8-17-2011

Development of novel bio/nano interfaces for materials science and biomedical applications

Carlee Ashley

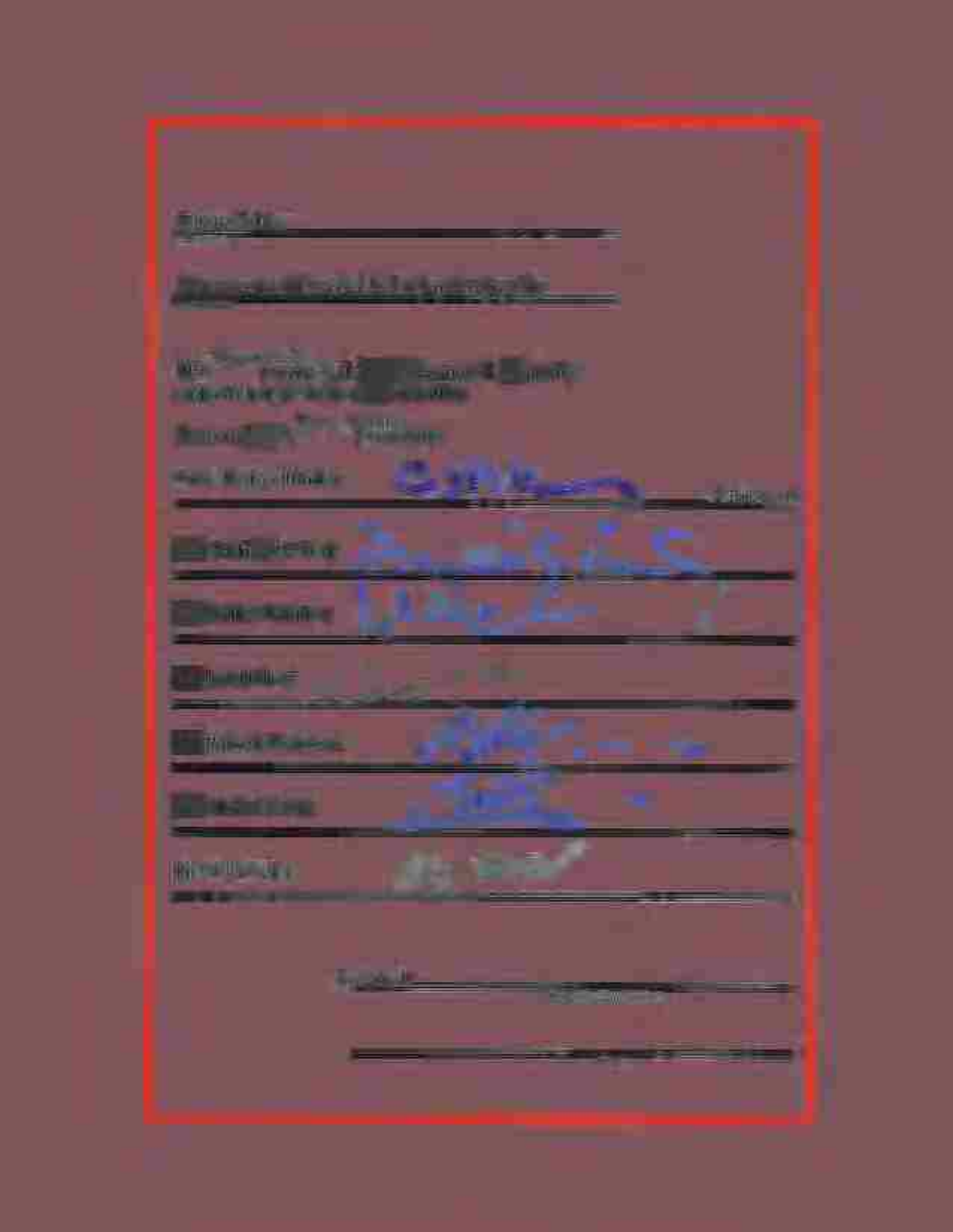

DEVELOPMENT OF NOVEL BIO/NANO INTERFACES FOR MATERIALS SCIENCE AND BIOMEDICAL APPLICATIONS

BY

CARLEE E. ASHLEY

B.S., Biochemistry, University of New Mexico, 2005

DISSERTATION

Submitted in Partial Fulfillment of the
Requirements for the Degree of

Doctor of Philosophy
Engineering

The University of New Mexico
Albuquerque, New Mexico

May, 2010

DEVELOPMENT OF NOVEL BIO/NANO INTERFACES FOR MATERIALS SCIENCE AND BIOMEDICAL APPLICATIONS

BY

CARLEE E. ASHLEY

ABSTRACT OF DISSERTATION

Submitted in Partial Fulfillment of the
Requirements for the Degree of

Doctor of Philosophy
Engineering

The University of New Mexico
Albuquerque, New Mexico

May, 2010

DEVELOPMENT OF NOVEL BIO/NANO INTERFACES FOR MATERIALS SCIENCE AND BIOMEDICAL APPLICATIONS

Carlee E. Ashley

B.S., Biochemistry, University of New Mexico, 2005
Ph.D., Engineering, University of New Mexico, 2010

ABSTRACT

Virus-like particles (VLPs) of MS2 bacteriophage possess a variety of characteristics that enable their use in biomedical and materials science applications. MS2 VLPs are perfectly monodisperse and possess a highly regular periodic structure. Their protein capsids can be modified in precise locations via chemical conjugation or genetic display of peptides, and their interior volumes can be readily loaded with a variety of non-genomic materials by taking advantage of their ability to self-assemble in the presence of RNA and RNA-modified cargos. Using peptides identified by filamentous phage display, I have demonstrated the utility of MS2 VLPs as targeted nanocarriers capable of highly specific delivery of various therapeutic and imaging agents to human cancer cells in vitro and as templates in the synthesis of novel types of nanomaterials, including self-assembled hexagonal close-packed arrays and nanoparticles

with greatly enhanced surface plasmonic properties. Multivalent peptide display on MS2 VLPs greatly enhances their affinity for target cells (e.g. hepatocellular carcinoma), providing the specificity necessary to deliver various therapeutic agents, including chemotherapeutic drugs, siRNA cocktails, and the A-chain of ricin toxin, to cancer cells without affecting the viability of normal cells (e.g. hepatocytes, endothelial cells, and immune cells). siRNA cocktails and ricin A-chain, when delivered to cancer cells via targeted VLPs, induce apoptosis within 48 hours at concentrations less than 10 pM and 100 fM, respectively. Multivalent peptide display on MS2 VLPs also promotes the deposition of remarkably thin, conformal coatings of gold. By encapsidating 16-nm quantum dots within VLPs prior to the metallization of their exterior surface, I hope to create a new class of core-shell nanoparticles with greatly enhanced fluorescence properties. Finally, evaporation-induced self-assembly of MS2 VLPs enables the formation of highly ordered hexagonal close-packed monolayers, the long-range periodicity of which can be measured using in situ GISAXS. Assembling the core-shell nanoparticles into a 2D array potentially enables construction of a hybrid plasmonic waveguide that allows optical energy to be transported from one location to another beyond the diffraction limit. For solar energy harvesting applications, the absorption coefficient of quantum dots is enhanced by the metal plasmonic shell, potentially enabling the development of an ultra-thin solar cell.

I have, additionally, developed a porous silica nanoparticle-supported lipid bilayer (‘protocell’) for targeted delivery applications. Protocells combine enhanced specificity, stability, and cargo capacity when compared to similarly-sized liposomes. They can, additionally encapsulate and deliver multicomponent cargos. Due to their unique

biophysical features, protocells loaded with drug cocktails (e.g. doxorubicin, 5-fluorouracil, and cisplatin) are able to kill drug resistant cancer cells 10^7-fold more effectively than FDA-approved liposomal doxorubicin (Doxil®).

Table of Contents

INTRODUCTION: **1**

CHAPTER 1: Protocells – A Universal Nanocarrier for Targeted Delivery of Multicomponent Cargos to Cancer **6**

CHAPTER 2: Multivalent Peptide Display on Virus-like Particles of MS2 Bacteriophage Facilitates Highly Specific Delivery of Cytotoxic Agents to Cancer **38**

CHAPTER 3: In-situ Grazing Incidence Small Angle X-ray Scattering of 2D Virus-Like Particle Lattice Formation via a Convective Assembly Process **82**

SUMMARY OF CONTRIBUTIONS: **97**

INTRODUCTION

Biological materials can direct the formation of complex inorganic materials (1, 2), while organic and inorganic materials can influence cellular behavior (e.g. sensing, dormancy, drug resistance, etc.) and induce cell death (3, 4). Although composite materials with biotic and abiotic elements have been developed for a wide variety of applications, I will focus on the use of bio-nano interfaces in two related research avenues: **(1)** the use of protein and inorganic nanoparticles for targeted delivery of multicomponent cargos to human cancer and **(2)** the self-assembly of protein nanoparticles into well-ordered structures that can be replicated in any arbitrary inorganic material via peptide-directed nucleation and growth.

A plethora of inorganic, organic, and biological materials have been developed for a vast number of medical applications, including biosensing (2), tissue regeneration (5), directed stem cell differentiation (6), single cell isolation and probing(3), lab-on-a-chip analysis of complex biofluids (7), high throughput DNA sequencing (8), vaccine development and other types of immunomodulation (9, 10), targeted delivery of therapeutic and diagnostic agents to cancer, virally-infected cells, and pathogenic bacteria (4, 11, 12), and controlled release of protein drugs and opioids (13-15). Nanoparticles composed of lipids (e.g. liposomes), polymers (e.g. PEG nanoparticles, PAMAM dendrimers, etc.), proteins (e.g. viruses, bacteriophages, virus-like particles, etc.), or inorganic materials (e.g. mesoporous silica, gold, etc.) have been used for passive and active targeting of drugs to a variety of cells, including cancer and pathogenic bacteria, as well as controlled release of encapsulated cargo over several days or weeks (4, 16, 17).

Liposomes and polymeric nanoparticles constitute the majority of nanoparticle-based delivery systems currently in FDA trials and have been utilized to encapsulate a variety of cargos and target a variety of cancers (18). More recently, porous inorganic particles have been used to deliver higher concentrations of cargo in a controllable fashion (19), while gold nanoparticles and nanoshells have been utilized to induce localized hyperthermia upon infrared radiation (20). Most state-of-the-art nanocarriers suffer from limited specificity, stability, and/or cargo capacity, however. To this end, I developed the protocell (21-23), a porous silica nanoparticle-supported lipid bilayer, for use in targeted delivery applications. The protocell combines enhanced specificity and stability with the ability to simultaneously encapsulate and deliver high concentrations of chemically disparate therapeutic and diagnostic agents. Protocells are, furthermore, non-toxic, non-immunogenic, and cost-effective to manufacture in large quantities (~0.5¢ per dose). I have also adapted virus-like particles of MS2 bacteriophage for use in targeted delivery applications. MS2 VLPs naturally self-assemble in the presence of RNA and can, therefore, be rapidly loaded with therapeutic RNAs, as well as any cargo that can be surface-modified with nucleic acids. Furthermore, targeting peptides and scFvs can be chemically conjugated or genetically inserted into the protein capsid of MS2 VLPs to promote selective cargo delivery. Importantly, MS2 VLPs are the first example of a platform that integrates the random peptide display capabilities of filamentous phage with the cargo capacity of a hollow capsid. Protocells and virus-like particles individually address numerous challenges associated with targeted delivery and can potentially be used as universal nanocarriers capable of delivering multicomponent cargos to any arbitrary type of cancer.

Globular proteins, as well as viruses, bacteriophages, and virus-like particles are highly monodisperse and can be assembled into well-ordered two- and three-dimensional structures using a variety of evaporation-driven techniques (24, 25). I have employed a horizontal convective assembly technique to promote the formation of *hcp* monolayers from a colloidal suspension containing virus-like particles of MS2 or Qβ bacteriophage. I monitored the time-dependent structural evolution of these monolayers via *in situ* GISAXS and modulated their long-range order by varying the coating conditions that affect particle-particle interactions and particle-substrate interactions. These self-assembled structures can be replicated in any inorganic material of interest via modification of the protein surface with peptides that promote nucleation and growth of a specific material. Phage display has been utilized to identify peptides that bind to a wide variety of inorganic materials. These peptides are capable of selectively binding to the target material and can recognize different lattice types (1). Furthermore, peptides that exist in an unbound form can promote the formation of nanoparticles from an appropriate precursor solution (26). Peptides conjugated to a surface can direct the organization of pre-formed nanoparticles into hierarchical structures and can, additionally, promote deposition of various materials on bacteriophage and viral surfaces(27). I have modified the surfaces of MS2 VLPs with gold-binding peptides that, when displayed in high densities, promote the deposition of thin, conformal gold coatings on the VLP surface. By encapsulating different materials, such as quantum dots, within the interior volume of MS2 VLPs prior to their metallization, I hope to create ultra-bright plasmonic nanoparticles, as well as metamaterials with unique optical and electrical properties.

References

1. Sarikaya M, Tamerler C, Jen AKY, Schulten K, & Baneyx F (2003) Molecular biomimetics: nanotechnology through biology. *Nat Mater* 2(9):577-585.
2. Baca HK, *et al.* (2006) Cell-directed assembly of lipid-silica nanostructures providing extended cell viability. *Science* 313(5785):337-341.
3. Carnes EC, *et al.* (2010) Confinement-induced quorum sensing of individual Staphylococcus aureus bacteria. *Nat Chem Biol* 6(1):41-45.
4. Peer D, *et al.* (2007) Nanocarriers as an emerging platform for cancer therapy. (Translated from English) *Nature Nanotechnology* 2(12):751-760 (in English).
5. Wong Po Foo CTS, Lee JS, Mulyasasmita W, Parisi-Amon A, & Heilshorn SC (2009) Two-component protein-engineered physical hydrogels for cell encapsulation. *Proceedings of the National Academy of Sciences* 106(52):22067-22072.
6. Levenberg S, *et al.* (2003) Differentiation of human embryonic stem cells on three-dimensional polymer scaffolds. *Proceedings of the National Academy of Sciences of the United States of America* 100(22):12741-12746.
7. Herr AE, *et al.* (2007) Microfluidic immunoassays as rapid saliva-based clinical diagnostics. *Proceedings of the National Academy of Sciences* 104(13):5268-5273.
8. Wendell D, *et al.* (2009) Translocation of double-stranded DNA through membrane-adapted phi29 motor protein nanopores. *Nat Nano* 4(11):765-772.
9. Hubbell JA, Thomas SN, & Swartz MA (2009) Materials engineering for immunomodulation. *Nature* 462(7272):449-460.
10. Peabody DS, *et al.* (2008) Immunogenic display of diverse peptides on virus-like particles of RNA phage MS2. *Journal of Molecular Biology* 380(1):252-263.
11. Kumar P, *et al.* (2008) T Cell-Specific siRNA Delivery Suppresses HIV-1 Infection in Humanized Mice. *Cell* 134(4):577-586.
12. Norman RS, Stone JW, Gole A, Murphy CJ, & Sabo-Attwood TL (2007) Targeted Photothermal Lysis of the Pathogenic Bacteria, Pseudomonas aeruginosa, with Gold Nanorods. *Nano Letters* 8(1):302-306.
13. Arias JL, Gómez-Gallo A, Delgado ÁV, & Ruiz MA (2009) Kollidon® SR colloidal particles as vehicles for oral morphine delivery in pain treatment. *Colloids and Surfaces B: Biointerfaces* 70(2):207-212.
14. Dasgupta S, Banerjee SS, Bandyopadhyay A, & Bose S (April 6, 2010) Zn- and Mg-Doped Hydroxyapatite Nanoparticles for Controlled Release of Protein. *Langmuir* 26(7):4958-4964.
15. Kakizawa Y, *et al.* (2009) Controlled release of protein drugs from newly developed amphiphilic polymer-based microparticles composed of nanoparticles. *Journal of Controlled Release* 142(1):8-13.
16. Ferrari M (2008) Nanogeometry: Beyond drug delivery. *Nat Nano* 3(3):131-132.
17. Rosi NL, *et al.* (2006) Oligonucleotide-Modified Gold Nanoparticles for Intracellular Gene Regulation. *Science* 312(5776):1027-1030.
18. Davis ME, *et al.* (March 21, 2010) Evidence of RNAi in humans from systemically administered siRNA via targeted nanoparticles. *Nature* advance online publication.
19. Xia T, *et al.* (2009) Polyethyleneimine Coating Enhances the Cellular Uptake of Mesoporous Silica Nanoparticles and Allows Safe Delivery of siRNA and DNA Constructs. *ACS Nano* 3(10):3273-3286.
20. Hirsch LR, *et al.* (2003) Nanoshell-mediated near-infrared thermal therapy of tumors under magnetic resonance guidance. *Proceedings of the National Academy of Sciences of the United States of America* 100(23):13549-13554.

21. Liu JW, Jiang XM, Ashley C, & Brinker CJ (2009) Electrostatically Mediated Liposome Fusion and Lipid Exchange with a Nanoparticle-Supported Bilayer for Control of Surface Charge, Drug Containment, and Delivery. *Journal of the American Chemical Society* 131(22):7567-+.
22. Liu JW, Stace-Naughton A, & Brinker CJ (2009) Silica nanoparticle supported lipid bilayers for gene delivery. *Chemical Communications* (34):5100-5102.
23. Liu JW, Stace-Naughton A, Jiang XM, & Brinker CJ (2009) Porous Nanoparticle Supported Lipid Bilayers (Protocells) as Delivery Vehicles. *Journal of the American Chemical Society* 131(4):1354-+.
24. Kuncicky Daniel M, Naik Rajesh R, & Velev Orlin D (2006) Rapid Deposition and Long-Range Alignment of Nanocoatings and Arrays of Electrically Conductive Wires from Tobacco Mosaic Virus13. *Small* 2(12):1462-1466.
25. Yuan Z, Petsev DN, Prevo BG, Velev OD, & Atanassov P (2007) Two-Dimensional Nanoparticle Arrays Derived from Ferritin Monolayers. *Langmuir* 23(10):5498-5504.
26. Slocik Joseph M, Stone Morley O, & Naik Rajesh R (2005) Synthesis of Gold Nanoparticles Using Multifunctional Peptides13. *Small* 1(11):1048-1052.
27. Nam KT*, et al.* (2006) Virus-Enabled Synthesis and Assembly of Nanowires for Lithium Ion Battery Electrodes. *Science*:1122716.

CHAPTER 1

Protocells – A Universal Nanocarrier for Targeted Delivery of Multicomponent Cargos to Cancer

It has been long recognized that the pharmacological properties of 'free' drugs can be improved through their targeted delivery using nanocarriers[1]. Although numerous types of cancer therapeutics that employ passively-targeted liposomes, polymers, or proteins for drug encapsulation or complexation are commercially-available[2], few clinically-approved drugs that selectively target diseased cells via specific biomolecular interactions yet exist[1]. Here we report the development of porous nanoparticle-supported lipid bilayers (protocells)[3-5], a new class of targeted nannocarriers which, due to a unique set of biophysical properties, simultaneously addresses multiple challenges associated with targeted delivery, including specificity, a high capacity for disparate types of cargo, controllable cargo release, stability, solubility, biocompatibility, and lack of immunogenicity[1]. Protocells, when modified with a targeting peptide (SP94[6]) that binds to human liver cancer (hepatocellular carcinoma, or HCC), exhibit a 10,000-fold greater affinity for HCC than for normal human hepatocytes, endothelial cells, and immune cells. We have loaded protocells with multicomponent cargos including therapeutics (e.g. drugs, siRNA, and protein toxins) and diagnostic agents (e.g. quantum dots). Significantly, due to the enormous cargo capacity of the high-surface-area nanoporous core combined with the enhanced targeting efficacy enabled by the supported lipid bilayer's remarkable fluidity, as few as *one* protocell loaded with a chemotherapeutic drug cocktail can kill an HCC cell with induced multiple drug resistance, representing a

10^6-fold improvement over liposomal doxorubicin[7]. Due to their combination of specificity, stability, and enhanced cargo capacity, we propose that protocells can serve as universal nanocarriers capable of delivering a high payload of therapeutic and diagnostic agents directly to human cancer cells with minimal systemic toxicity.

Targeted delivery of drugs encapsulated within nanocarriers can potentially ameliorate a number of problems exhibited by conventional 'free' drugs, including poor solubility, limited stability, rapid clearing, and lack of selectivity, which can result in non-specific toxicity to healthy cells and prevent the dose escalation necessary to eradicate diseased cells[8]. *Passive* targeting schemes, which rely on the enhanced permeability of the tumor vasculature to promote accumulation of nanocarriers (the so-called enhanced permeability and retention, or EPR, effect) overcome many of these problems, but the lack of cell-specific interactions needed to induce nanocarrier internalization can result in drug expulsion and induction of multiple drug resistance (MDR)[9]. Additionally, not all tumors exhibit the EPR effect,[10] and passively-targeted nanocarriers are no more effective at treating blood cancers then free drugs[11]. *Selective* targeting strategies employ ligands (e.g. peptides, monoclonal antibodies, aptamers, vitamins, etc.) conjugated to the nanocarrier surface that specifically interact with receptors expressed on the cell surface of interest[12]. This strategy requires that receptors are highly over-expressed by the target cell (10^4-10^5 copies/cell) relative to normal cells[1]. Displaying multiple copies of the targeting ligand on the nanocarrier surface promotes collective, multivalent binding effects that result in enhanced affinity[13] and more efficient drug delivery through receptor-mediated internalization pathways, which help circumvent the efflux mechanisms that contribute to MDR[14]. However, it has been observed that targeting ligands can also increase non-specific interactions, resulting in rapid entrapment of nanocarriers by such barriers as the walls of blood vessels and phagocytic

cells that reside in the liver and spleen [15]. Modifying the nanocarrier surface with hydrophilic, shielding polymers (e.g. polyethylene glycol, or PEG) reduces non-specific interactions with serum proteins and macrophages of the reticuloendothelial system but also invariably diminishes targeting specificity[15].

Liposomes are the most extensively studied class of nanocarriers due to their low inherent toxicity and immunogenicity, as well as the relative ease with which their surfaces can be modified with PEG to improve circulation times[12]. However, nearly ten years after FDA-approval of liposomal doxorubicin, there remain significant challenges to the successful implementation of liposomes as targeted nanocarriers. Liposomes and other targeted nanocarriers must be able to simultaneously achieve high targeting specificity and delivery efficiency, while avoiding entrapment by the body's defences. Other desirable characteristics include a high capacity for disparate types of therapeutic and diagnostic agents, the ability to controllably release encapsulated cargo upon internalization within the target cell, stability, solubility, and lack of immunogenicity[1]. In some cases, it is also desirable to direct the intracellular targeting of delivered cargo in order to maximize therapeutic efficacy [16].

Here we report the development of a novel targeted nanocarrier: the 'protocell,' a porous nanoparticle-supported lipid bilayer[3-5] (see Figure 1) that addresses many limitations associated with state-of-the-art nanocarriers. Fusion of liposomes to a spherical, high-surface-area nanoporous silica core followed by modification of the resulting supported lipid bilayer (SLB) with PEG and multiple copies of targeting and fusogenic peptides creates a unique construct that, in comparison to liposomes, maintains enhanced selectivity and stability while enabling the targeted delivery and controlled release of high concentrations of multicomponent cargos (see Figure 2b). Importantly, the nanoporous silica core suppresses the large-scale bilayer fluctuations that limit liposome

stability while also enhancing bilayer fluidity compared to that of either unsupported bilayers (i.e. 'empty' liposomes) or bilayers supported on solid silica particles. This synergistic combination of properties enables high targeting specificity with a minimal number of targeting ligands, which is crucial to reduce non-specific binding and minimize immunogenicity.

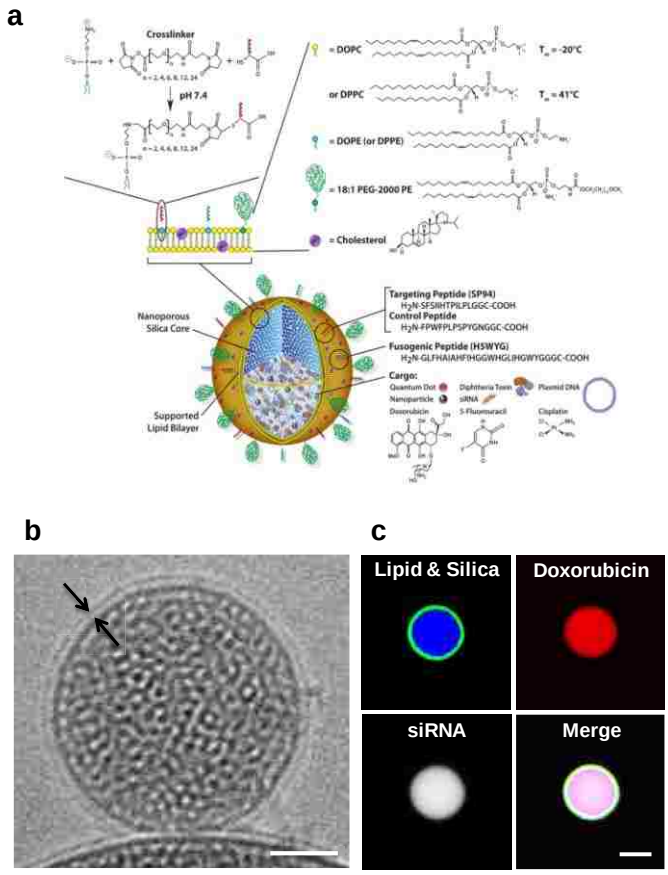

Figure 1. Features of the porous nanoparticle-supported lipid bilayer. (a) A schematic of the protocell, depicting the disparate types of therapeutic and diagnostic agents that can be loaded within the nanoporous silica core. Targeting and fusogenic peptides can be conjugated to phosphatidylethanolamine (DOPE or DPPE), present in the SLB at 1-10 wt%, via a heterobifunctional crosslinker with a PEG spacer arm. The SLB is composed of either fluid (DOPC) or non-fluid (DPPC) zwitterionic lipids with 30 wt% cholesterol and 5 wt% PEG-2000 PE to enhance colloidal stability and decrease non-specific interactions. (b) Cryogenic TEM image of the protocell, showing the nanoporous core and the 5-nm SLB (bracketed by arrows). Scale bar = 25 nm. (c) Fluorescence microscopy image of protocells formed on large porous cores to enable imaging, showing NBD-labeled lipid (green) fully encapsulating the Alexa Fluor 405®-labeled silica core (blue), which is loaded with doxorubicin (red) and Alexa Fluor 647®-labeled siRNA (white). Scale bar = 5 μm.

To demonstrate the unique biophysical properties of protocells, Figure 2a shows temperature-dependent fluorescence recovery after photobleaching (FRAP) results for a DPPC (transition temperature, T_m = 41˚C) bilayer supported on a nanoporous or solid silica particle. We observe that the photobleached region begins to recover at 35°C (± 1°C) for the nanoporous SLB compared to 41°C (± 1°C) for both the solid SLB and unilamellar liposomes[17]: in effect the nanoporous support suppresses the transition temperature of DPPC by 6°C. We propose that the underlying 3D porosity of the support (composed of nanoscopic patches of silica and water) modulates the local packing density of lipid head groups, thereby increasing fluidity without appreciably changing the average packing density (determined by us previously using neutron reflectivity[18]). This effect is not observed for bilayers supported on either solid surfaces or silica thin films with 2D nanopores oriented parallel to the substrate surface (where T_m = 41˚C as commonly reported). As illustrated in Figure 2b, increased SLB fluidity enables a targeting peptide, when displayed in low densities on the SLB, to bind multivalently to surface receptor(s) expressed by the cancer cell of interest (HCC in this case); cooperative, multivalent interactions are crucial to achieve high specific affinity and to direct receptor-mediated endocytosis of protocells. The ability of targeting peptides to be recruited to a cancer cell surface when displayed on a nanoporous SLB is vividly demonstrated in Figure 2c. NBD-labeled DOPC (T_m = -20˚C) or DPPC liposomes were fused to a planar nanoporous substrate (with a 3D pore structure identical to that of the protocell core) and modified with a low density (~0.015 wt%) of Alexa Fluor 647®-labeled SP94 peptides (H_2N-SFSIILTPILPL-COOH, identified via filamentous phage display to have an affinity for unknown receptor(s) expressed by human HCC[6]). Upon addition of an HCC cell line (Hep3B) to the supported planar bilayers at 25°C, we

observed rapid (1-2 minutes) recruitment of SP94 peptides to the cancer cell surface for the fluid DOPC bilayer with no measurable recruitment for the solid DPPC bilayer. As shown in Figure 2d, SP94-targeted DOPC protocells are efficiently endocytosed by Hep3B but not by normal (i.e. untransformed) hepatocytes.

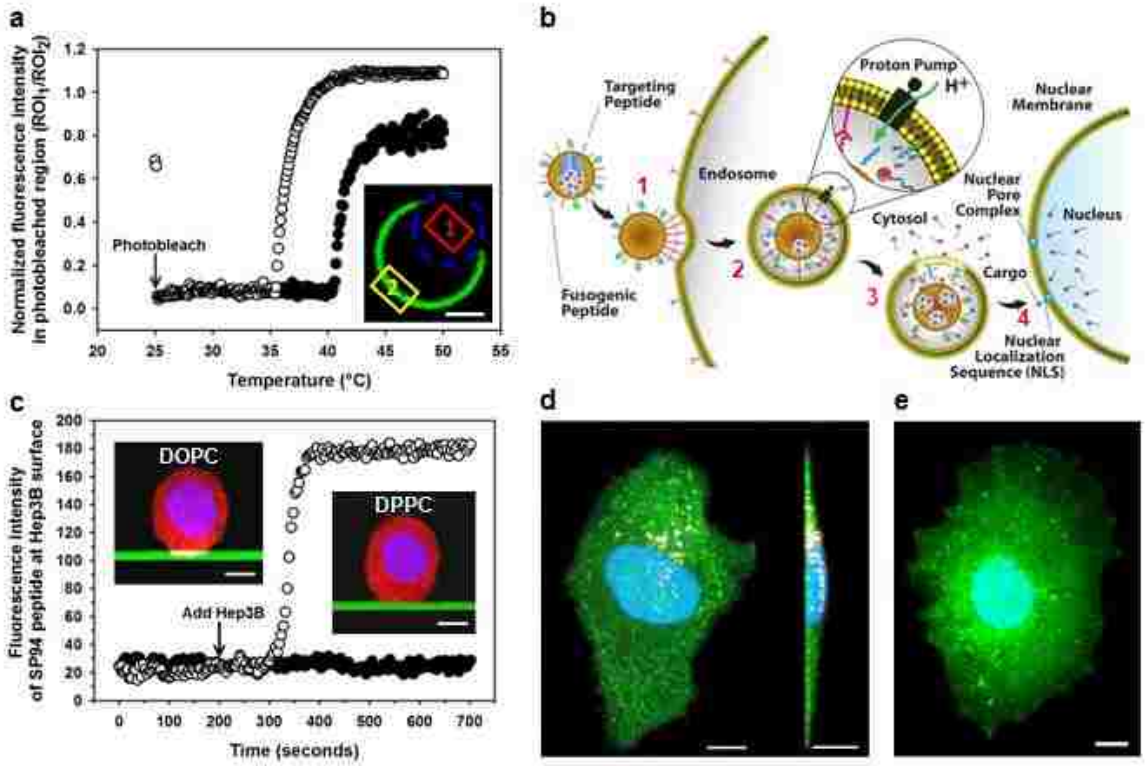

Figure 2. Biophysical characteristics of protocells that promote high affinity surface binding and internalization by HCC. (a) Temperature-dependent FRAP of NBD-labeled DPPC bilayers (green) supported on nanoporous (○) or solid (●) spherical silica particles. Inset: normalized fluorescence recovery in the photobleached region (blue circle) was determined by dividing the fluorescence intensity (FI) in region of interest 1 (ROI_1) by the FI in ROI_2. Scale bar = 5 μm. (b) DOPC protocells bind to HCC with high affinity due to recruitment of SP94 targeting peptides to the cell surface (step 1), become internalized via receptor-mediated endocytosis (step 2), and release their cargo into the cytosol upon endosome acidification and protonation of the H5WYG fusogenic peptide (step 3). Cargos modified with a NLS are transported through the nuclear pore complex and become concentrated in the nucleus (step 4). (c) SP94 peptides (white) can be recruited to the surface of a Hep3B cell (cytosol = red, nucleus = blue) at 25°C when displayed on a planar nanoporous SLB (green) composed of DOPC (○) but not DPPC (●). Inset scale bars = 5 μm. (d) and (e) DOPC protocells (lipid = red, silica = white) that display a low density of SP94 are endocytosed by Hep3B (d; cytosol = green, nucleus = blue) but not by hepatocytes (e). Scale bars = 10 μm.

To demonstrate that specific affinity for HCC is dramatically influenced by multivalent binding effects and that these effects can be enhanced when peptides are displayed on a fluid SLB, we conjugated various densities of SP94 (1 to 2048 peptides per particle, on average) to DOPC or DPPC protocells and liposomes and determined the resulting dissociation constants (K_d) using flow cytometry (low K_d values correspond to high specific affinities; see Supplementary Figure 1 for details). Figure 3a demonstrates that SP94-targeted DOPC protocells have a high specific affinity (K_d < 1 nM) for Hep3B and that, over the range of 6 to 2048 peptides per particle, their K_d values are consistently low (0.94 – 0.08 nM) and relatively independent of peptide density. DOPC protocells modified with ~240 copies of the SP94 peptide have a K_d (~0.1 nM) that is 10^4-fold lower than the K_d values of SP94-targeted protocells for various control cells, including human hepatocytes (see Figure 3b), endothelial cells (HUVECs), and immune cells (PBMCs and B- and T-lymphocytes), 2000-fold lower than the K_d of free SP94 for Hep3B, and nearly 50,000-fold lower than the K_d of unmodified protocells for Hep3B (see Supplementary Figure 2). The influence of SLB fluidity on multivalent binding and specific affinity is clearly illustrated by a comparison of DOPC and DPPC protocells modified with various concentrations of SP94 (see Figure 3a). At high SP94 densities (≥ 240 peptides/particle), multivalent effects can be realized even when peptides are displayed on solid DPPC SLBs. At lower SP94 densities, however, the K_d values of DPPC protocells increase dramatically with decreasing peptide density and approach the K_d of the monovalent peptide. This result is due to the kinetic hindrance experienced by peptides conjugated to solid SLBs, which limits peptide recruitment to the cancer cell surface and decreases the specific affinity of DPPC protocells in a peptide density-dependent fashion. The K_d values of protocells are consistently lower than those of similarly-sized liposomes (~120-nm in diameter) at all SP94 densities (see Figure 3a), a result we attribute to the enhanced fluidity of the protocell SLB combined with the ability

of the nanoporous core to suppress the large-scale bilayer fluctuations that likely act as a steric barrier to multivalent binding of peptides displayed on liposomes to the Hep3B surface. At a density of ~6 peptides per particle, DOPC protocells have a 200-fold lower K_d than DOPC liposomes, the significance of which is demonstrated by our observation that reducing peptide density greatly decreases non-specific binding of DOPC and DPPC protocells and liposomes to normal hepatocytes (see Figure 3b). Therefore, protocells that possess a fluid SLB are uniquely able to selectively target HCC at low SP94 densities, as evidenced by the 10^4-fold difference between their specific affinity for Hep3B and their non-specific interaction with hepatocytes. If sub-nanomolar affinity is undesirable (e.g. results in reduced tumor penetration), the K_d values of SP94-targeted protocells can be precisely modulated by incorporating various amounts of fluid and non-fluid lipids into the SLB (see Supplementary Figure 3).

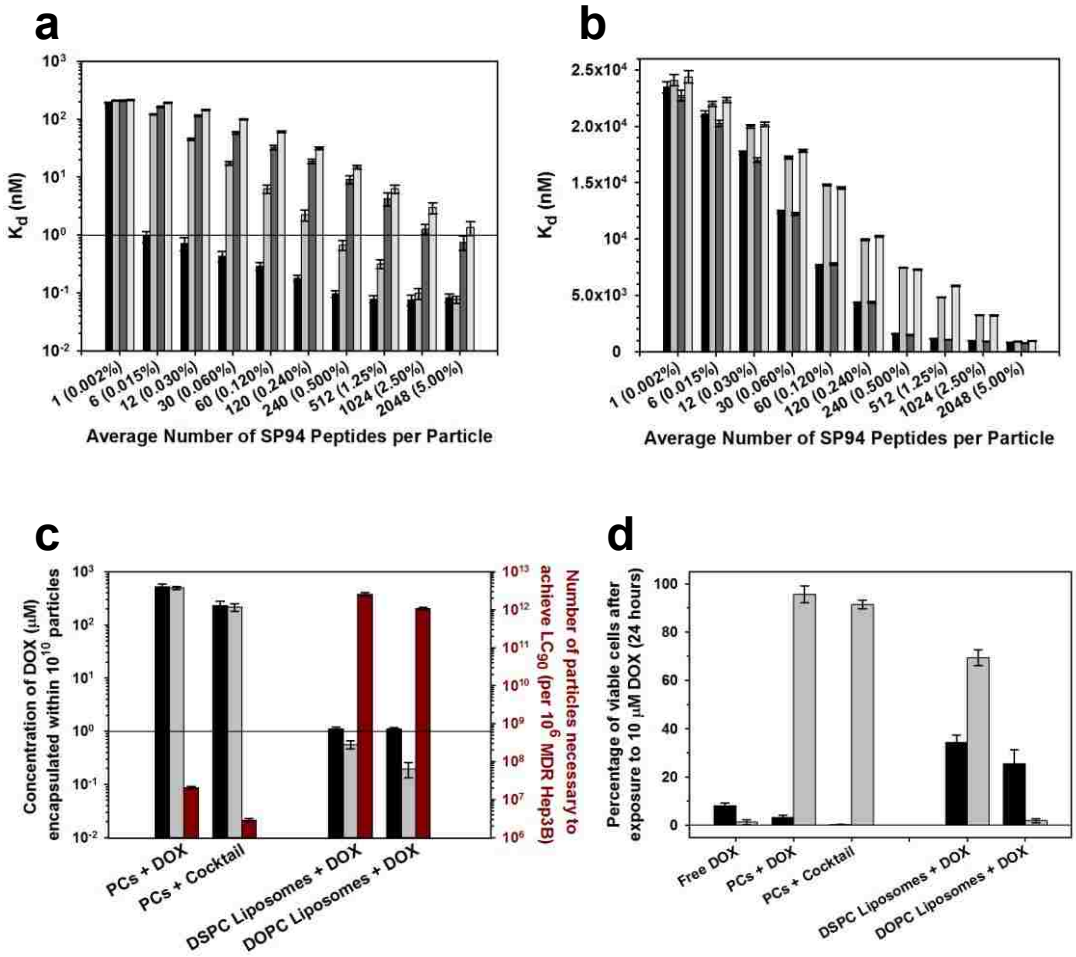

Figure 3. The specific affinity and cytotoxicity of protocells, as compared to liposomes. (a) and (b) Dissociation constants (K_d) of SP94-targeted protocells and liposomes for Hep3B (a) and hepatocytes (b) as a function of the average number of SP94 peptides per particle (average SP94 wt% is in parentheses). K_d values are shown for DOPC protocells (■), DPPC protocells (■), DOPC liposomes (■), and DPPC liposomes (■). DOPC protocells modified with a low density of SP94 have a maximal affinity for Hep3B and a minimal affinity for hepatocytes. All surface binding experiments were conducted at 4°C to prevent endocytosis of protocells and liposomes. (c) Capacity and cytotoxicity of DOX-loaded protocells and liposomes. Left axis: the absolute (■) and effective capacities (■) of DOPC protocells, DSPC liposomes, and DOPC liposomes for DOX. Absolute capacity is defined as the concentration of DOX that can be physically encapsulated within 10^{10} particles, while effective capacity is the concentration of DOX that is released upon endocytosis by HCC in a form capable of intercalating nuclear DNA. Right axis: the number of DOX-loaded protocells or liposomes (■) that must be added to 10^6 MDR Hep3B to kill 90% of the cells in the population (LC_{90}) within 24 hours. See Supplementary Figure 9 for the LC_{90} values of free DOX and DOX-loaded protocells. (d) The number of MDR Hep3B (■) and hepatocytes (■) that remain viable after exposure to 10 μM of free DOX, protocell-encapsulated DOX, or liposomal DOX for 24 hours. Due to their enhanced specificity, stability, and capacity, protocells are cytotoxic to MDR Hep3B but not hepatocytes. Sytox® Green nucleic acid stain and Alexa Fluor 647®-labeled annexin V were used to distinguish viable (double-negative) from non-viable (single- or double-positive) cells. All error bars represent 95% confidence intervals (1.96 σ) for n = 5 (a and b) or n = 3 (c and d).

As illustrated schematically in Figure 2b, multivalent binding of SP94 to HCC surface receptor(s) initiates receptor-mediated endocytosis, an internalization pathway that helps to circumvent MDR[19]. The confocal microscopy images in Figures 2d and 2e demonstrate that SP94-targeted DOPC protocells are internalized by Hep3B but not by hepatocytes. To demonstrate that high affinity surface binding followed by receptor-mediated endocytosis enables targeted delivery of multicomponent cargos, we encapsulated various therapeutic and diagnostic agents (see Figure 1a) within the protocell core by simply soaking the nanoporous particles in a solution of the desired cargo prior to fusion of DOPC liposomes and conjugation of SP94 peptides to the SLB. We determined that the SP94 peptide directs protocells to lysosomes upon endocytosis by HCC (see Supplementary Figure 4); in order to prevent degradation of sensitive cargo, we further modified the SLB with a histidine-rich fusogenic peptide (H5WYG, H_2N-GLFHAIAHFIHGGWHGLIHGWYG-COOH[20]) that promotes endosomal escape without affecting the integrity of the plasma membrane. As illustrated in Figure 2b, delivery of encapsulated cargo to HCC is achieved via the following successive steps: (1) DOPC protocells bind to the surface of HCC cells via the interaction between SP94 (magenta) and unknown receptor(s) overexpressed by HCC. Peptide recruitment to the cell surface promotes the multivalent effects that increase specificity. (2) Protocells are endocytosed by HCC cells, and endosome acidification destabilizes the SLB (see Supplementary Figure 5), thereby enabling encapsulated cargo to diffuse out of the nanoporous core. Protonation of imidazole moieties (pK_a = 6.0) in the fusogenic peptide (blue) initiates osmotic swelling and membrane destabilization of endosomes via the 'proton sponge' mechanism. (3) Endosome disruption enables protocell components and cargo to become distributed in the cytosol of the HCC cell. (4) Finally, cargo modified with a nuclear localization sequence (M9 domain of heterogeneous nuclear ribonucleoprotein A1, H_2N-

NQSSNFGPMKGGNFGGRSSGPYGGGGQYFAKPRNQGGY-COOH[21]) become concentrated in the nucleus. By encapsulating fluorescent surrogates (similar in size and charge to therapeutic or diagnostic agents of interest) within protocells prepared with fluorescently-labelled SLBs and nanoporous cores, the various stages involved in cargo delivery can be visualized by hyperspectral confocal fluorescence microscopy (Figure 4). As evidenced by the appearance of punctuate regions containing co-localized lipid, silica, and cargo, protocells are rapidly endocytosed ($t_{½}$ = 15 minutes) by Hep3B cells (see Figure 4a) and reach a saturating intracellular concentration (~500 protocells per Hep3B cell) within 2 hours. Approximately 4 hours after endocytosis, the lipid and silica moieties of the protocell, as well as the four model cargos become distributed throughout the cytosol of Hep3B cells (see Figure 4b), and, within 24 hours, cargos modified with the NLS are targeted to the nuclei (see Figure 4c).

We have utilized the above sequence of events to deliver high payloads of various cytotoxic agents, including drugs and drug cocktails, siRNA cocktails (see Supplementary Figure 6), and protein toxins (see Supplementary Figure 7) to Hep3B without affecting the viability of control cells. Due to the large pore volume (~50%) and high surface area (>1000 m^2/g) of their nanoporous cores, protocells have a 1000-fold higher capacity for the chemotherapeutic drug, doxorubicin (DOX) than similarly-sized liposomes loaded via an ammonium phosphate gradient-based approach (see Figure 3c, left axis). Additionally, protocells exhibit long-term stability that is independent of the SLB composition: given that their SLBs remain fully intact, DOPC protocells release a negligible amount of DOX when maintained in neutral pH buffer or complete growth medium at 4°C for > 3 weeks (see Supplementary Figure 8). Conversely, DOPC liposomes release nearly all of their encapsulated DOX within 72 hours. Therefore, the fluid lipids that enable selective targeting at low peptide densities (necessary to minimize

non-specific binding and uptake by the body's defences) cannot be used in liposomal drug formulations, since pre-mature release of encapsulated cargo results in non-specific toxicity to healthy cells (see discussion of Figure 3d).

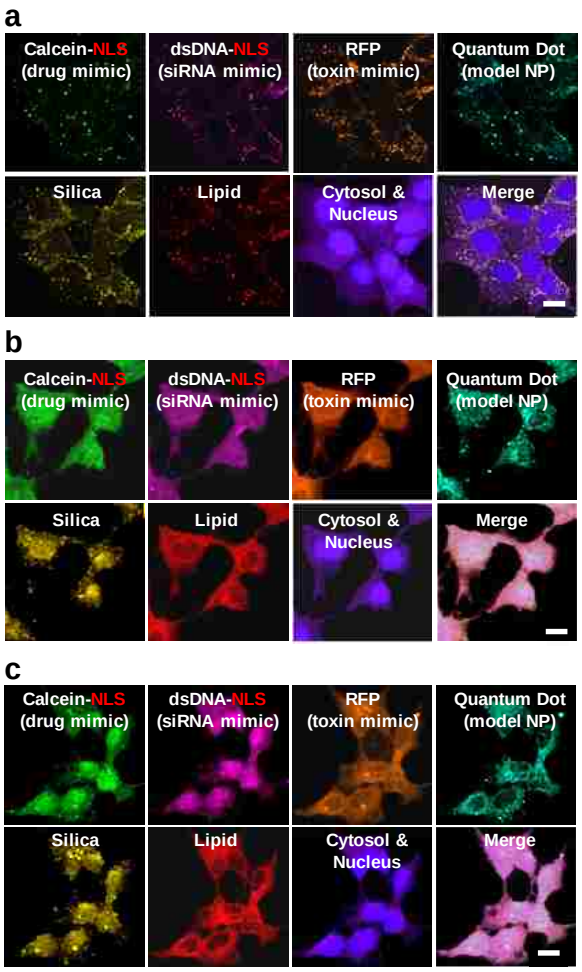

Figure 4. Delivery of multicomponent cargos to the cytosol and nuclei of HCC cells. Hyperspectral confocal fluorescence microscopy was employed to individually track the lipid (red) and silica (yellow) of the protocell, as well as four model types of cargo (green = calcein, a low molecular weight drug mimic; magenta = a double-stranded DNA oligonucleotide, which acts as a siRNA mimic; orange = red fluorescent protein, a protein toxin mimic; teal = far red-fluorescent quantum dots, a model nanoparticle) within the cytosol (purple) and nuclei (blue) of Hep3B cells as a function of time. (a) Within 15 minutes of exposing Hep3B to protocells loaded with the multicomponent mixture, the lipid, silica, and cargos have a punctate appearance, indicating that protocells are localized within endosomes. (b) Within 4 hours, the H5WYG peptide promotes endosomal escape, thereby releasing the lipid, silica, and cargos into the cytosol of the Hep3B cells. (c) Within 24 hours, calcein and the dsDNA oligonucleotide, both of which are modified with a NLS, become concentrated in the nucleus, while the RFP and quantum dots remain largely localized in the cytosol. Scale bars = 20 μm.

The combination of properties unique to targeted protocells solve the challenge of maintaining high targeting specificity and inducing rapid cytotoxicity of target cells, while avoiding collateral damage to normal cells. Figure 3c (right axis) plots the number DOPC protocells and liposomes, loaded with DOX, modified with a low peptide density (0.015%), and stabilized with PEG, needed to kill 90% of Hep3B with induced MDR (LC_{90}). We observe that 10^5 fewer protocells are necessary to achieve the LC_{90} value than for corresponding liposomes. Figure 3d shows the percentage of Hep3B and hepatocytes that remain viable after exposure to 10 μM of DOX (in a 'free' form or encapsulated within protocells or liposomes) for 24 hours. Here we observe that DOX-loaded protocells maintain greater than 90% hepatocyte viability, while killing over 95% of MDR Hep3B. By comparison, liposomes are less efficient at killing Hep3B and induce significant cytotoxicity of normal cells. We attribute these striking differences to the several orders of magnitude higher capacity (Figure 3c) and binding affinity (Figure 3a) of DOPC protocells, which combine synergistically to provide dramatic improvements in selective cytotoxicity, as well as the low density of targeting peptides and long-term SLB stability, which reduce non-specific binding and toxicity to normal cells. Importantly, protocells can also be loaded with multicomponent cargos. Figures 3c and 3d show that, when loaded with a cocktail of DOX, 5-fluorouracil, and cisplatin (a chemotherapeutic drug cocktail known to be particularly effective against HCC[22]), as few as ***one*** SP94-modified protocell is sufficient to kill a Hep3B cell with induced MDR while maintaining > 90% hepatocyte viability.

In summary, we have demonstrated that protocells bearing the SP94 targeting peptide combine the high specificity, enhanced cargo capacity, and long-term stability necessary to deliver a variety of therapeutic and diagnostic agents to cancer cells with minimal side effects. The combined attributes of protocells enable their use as a universal

nanocarrier that simultaneously addresses the complex requirements of multicomponent targeted delivery, the successful implementation of which is critical to effectively combat cancer.

Methods Summary

Nanoporous silica particles were synthesized and characterized as described previously by us (see Supplementary Figure 10)[23], and particles larger than 200-nm in diameter were removed via differential centrifugation or size-exclusion chromatography (see Supplementary Figure 10b and 10f). Protocells were formed by fusing 120-nm liposomes to the nanoporous core as reported previously[3-5], and the composition of the SLB was optimized to reduce non-specific binding and to mitigate the cytotoxicity associated with cationic and, to a lesser extent, anionic lipids (see Supplementary Figures 11 and 12)[24]. Zwitterionic lipids, such as DOPC or DPPC, with 5 wt% phosphatidylethanolamine (PE), 5 wt% PEG-2000 PE, and 30 wt% cholesterol were used in all further studies. The size of the nanoporous core was also optimized to attain a balance between achievable cargo capacity and the rate of protocell internalization (see Supplementary Figure 13); nanoparticles 100- to 150-nm in diameter were employed in the delivery of drugs, drug cocktails, siRNA cocktails, protein toxins, and plasmid DNA. In order to maximize targeting efficacy, the SLB was modified with various types of targeting ligands known to have an affinity for HCC (see Supplementary Figure 14), and SP94 was selected for use in delivery experiments. The nanoporous cores were soaked in a 10 mM solution of cargo(s) for 1-12 hours prior to liposome fusion. The rate of intracellular cargo release

was optimized by incorporating various percentages of AEPTMS, an amine-containing silane, into the sol used to form the nanoporous cores. Particles containing 30wt% AEPTMS were used to deliver drugs and drug cocktails.

References:

1 Peer, D. *et al.* Nanocarriers as an emerging platform for cancer therapy. *Nature Nanotechnology* **2**, 751-760, (2007).

2 Wagner, V., Dullaart, A., Bock, A.-K. & Zweck, A. The emerging nanomedicine landscape. *Nat Biotech* **24**, 1211-1217 (2006).

3 Liu, J. W., Jiang, X. M., Ashley, C. & Brinker, C. J. Electrostatically Mediated Liposome Fusion and Lipid Exchange with a Nanoparticle-Supported Bilayer for Control of Surface Charge, Drug Containment, and Delivery. *Journal of the American Chemical Society* **131**, 7567-+, (2009).

4 Liu, J. W., Stace-Naughton, A. & Brinker, C. J. Silica nanoparticle supported lipid bilayers for gene delivery. *Chemical Communications*, 5100-5102, (2009).

5 Liu, J. W., Stace-Naughton, A., Jiang, X. M. & Brinker, C. J. Porous Nanoparticle Supported Lipid Bilayers (Protocells) as Delivery Vehicles. *Journal of the American Chemical Society* **131**, 1354-+, (2009).

6 Lo, A., Lin, C. T. & Wu, H. C. Hepatocellular carcinoma cell-specific peptide ligand for targeted drug delivery. *Molecular Cancer Therapeutics* **7**, 579-589, (2008).

7 Gordon, A. N. *et al.* Recurrent Epithelial Ovarian Carcinoma: A Randomized Phase III Study of Pegylated Liposomal Doxorubicin Versus Topotecan. *J Clin Oncol* **19**, 3312-3322 (2001).

8 Ferrari, M. Cancer nanotechnology: Opportunities and challenges. *Nat. Rev. Cancer* **5**, 161-171, (2005).

9 Gottesman, M. M., Fojo, T. & Bates, S. E. Multidrug resistance in cancer: Role of ATP-dependent transporters. *Nat. Rev. Cancer* **2**, 48-58, (2002).

10 Jain, R. K. Barriers to drug-delivery in solid tumors. *Scientific American* **271**, 58-65 (1994).

11 Sapra, P. & Allen, T. M. Internalizing Antibodies Are Necessary for Improved Therapeutic Efficacy of Antibody-targeted Liposomal Drugs. *Cancer Res* **62**, 7190-7194 (2002).

12 Torchilin, V. P. Recent advances with liposomes as pharmaceutical carriers. *Nat Rev Drug Discov* **4**, 145-160 (2005).

13 Jiang, W., KimBetty, Y. S., Rutka, J. T. & ChanWarren, C. W. Nanoparticle-mediated cellular response is size-dependent. *Nat Nano* **3**, 145-150, doi:http://www.nature.com/nnano/journal/v3/n3/suppinfo/nnano.2008.30_S1.html (2008).

14 Pastan, I., Hassan, R., FitzGerald, D. J. & Kreitman, R. J. Immunotoxin therapy of cancer. *Nat Rev Cancer* **6**, 559-565 (2006).

15 Ferrari, M. Nanogeometry: Beyond drug delivery. *Nat Nano* **3**, 131-132 (2008).
16 Peer, D., Zhu, P., Carman, C. V., Lieberman, J. & Shimaoka, M. Selective gene silencing in activated leukocytes by targeting siRNAs to the integrin lymphocyte function-associated antigen-1. *Proc. Natl. Acad. Sci. U. S. A.* **104**, 4095-4100 (2007).
17 Bothun, G. D., Knutson, B. L., Strobel, H. J. & Nokes, S. E. Liposome Fluidization and Melting Point Depression by Pressurized CO2 Determined by Fluorescence Anisotropy. *Langmuir* **21**, 530-536, (2004).
18 Doshi, D. A. *et al.* Neutron Reflectivity Study of Lipid Membranes Assembled on Ordered Nanocomposite and Nanoporous Silica Thin Films. *Langmuir* **21**, 2865-2870, (2005).
19 Goren, D. *et al.* Nuclear delivery of doxorubicin via folate-targeted liposomes with bypass of multidrug-resistance efflux pump. *Clin. Cancer Res.* **6**, 1949-1957 (2000).
20 Midoux, P., Kichler, A., Boutin, V., Maurizot, J.-C. & Monsigny, M. Membrane Permeabilization and Efficient Gene Transfer by a Peptide Containing Several Histidines. *Bioconjugate Chemistry* **9**, 260-267, (1998).
21 Subramanian, A., Ranganathan, P. & Diamond, S. L. Nuclear targeting peptide scaffolds for lipofection of nondividing mammalian cells. *Nat Biotech* **17**, 873-877 (1999).
22 Lee, J. O. *et al.* Combination chemotherapy with capecitabine and cisplatin for patients with metastatic hepatocellular carcinoma. *Annals of Oncology* **20**, 1402-1407, (2009).
23 Carroll, N. J., Pylypenko, S., Atanassov, P. B. & Petsev, D. N. Microparticles with Bimodal Nanoporosity Derived by Microemulsion Templating. *Langmuir*, (2009).
24 Xia, T. *et al.* Comparison of the Mechanism of Toxicity of Zinc Oxide and Cerium Oxide Nanoparticles Based on Dissolution and Oxidative Stress Properties. *ACS Nano* **2**, 2121-2134, (2008).

Supplementary Figures and Legends:

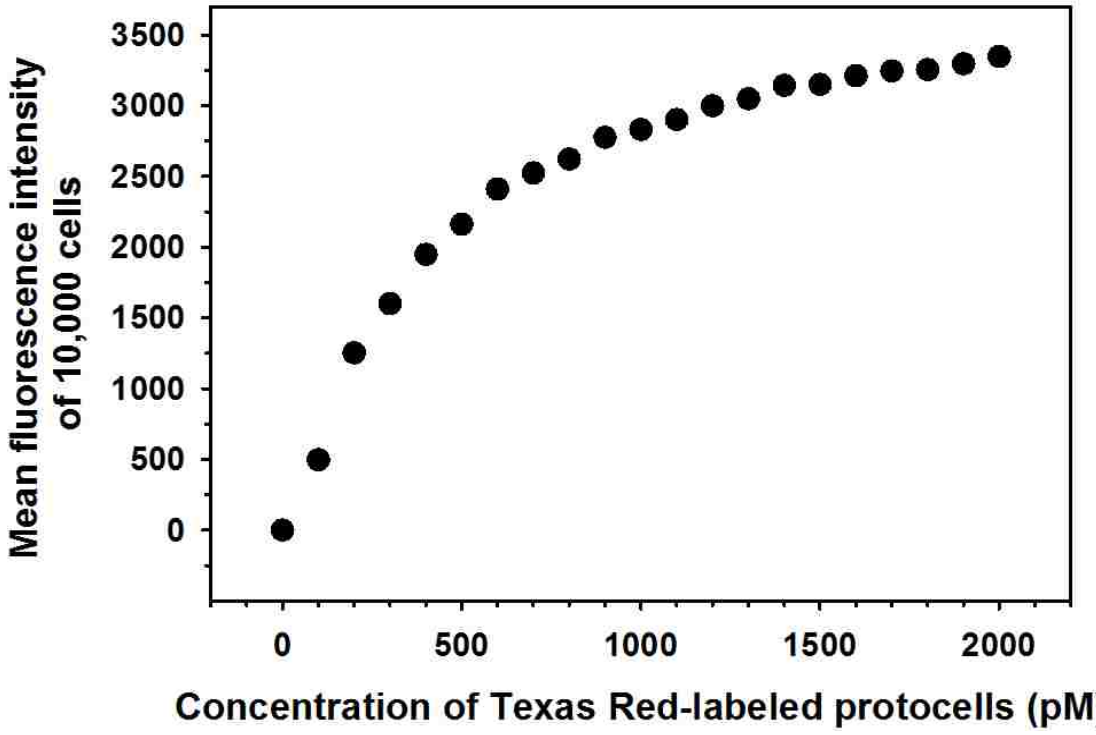

Supplementary Figure 1. Saturation binding curves were constructed by exposing various concentrations of fluorescently-labeled particles (unmodified and SP94-targeted protocells and liposomes) to a fixed number of cells (HCC and control cells) and measuring the mean fluorescence intensity of each cell population via flow cytometry. GraphPad Prism (GraphPad Software, Inc.; La Jolla, CA) was employed to calculate dissociation constants (K_d) from binding curves. The above curve represents the K_d (~0.40 nM) of DOPC protocells modified with 0.060 wt% SP94 (~30 peptides/particle) when exposed to Hep3B.

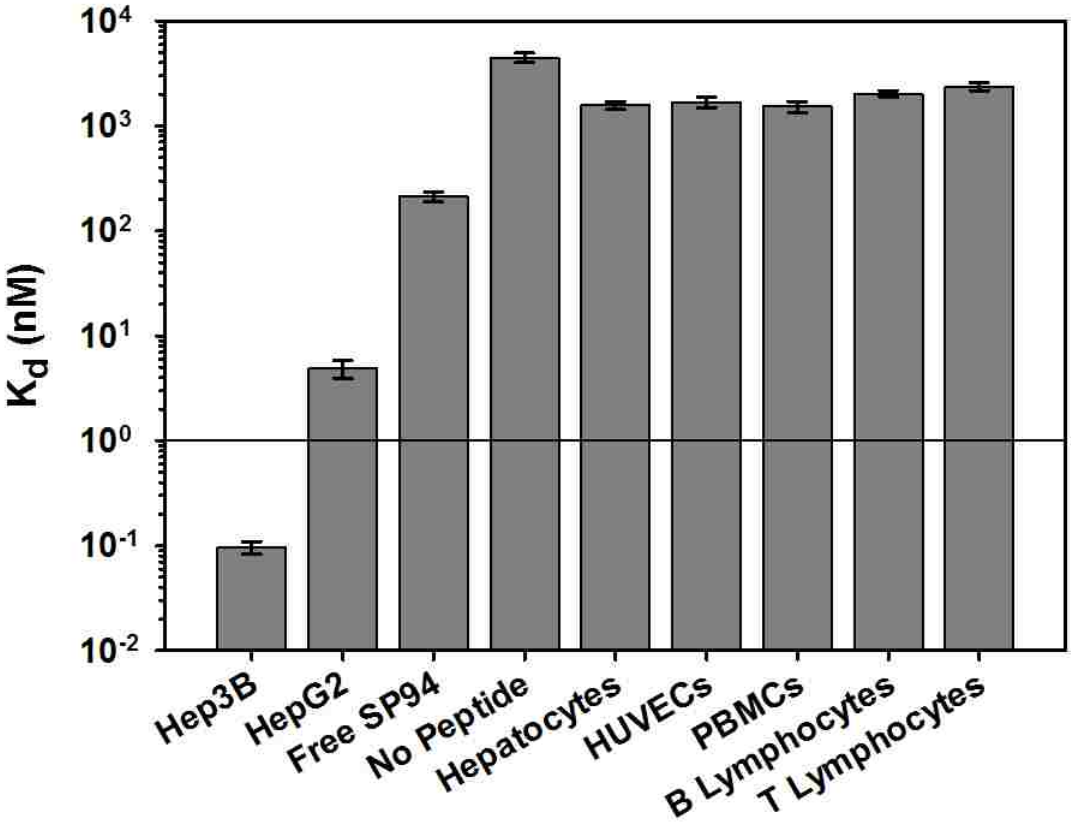

Supplementary Figure 2. The K_d values of DOPC protocells modified with 0.500 wt% SP94 (~240 peptides/particle) for Hep3B and HepG2, the K_d of free SP94 for Hep3B, the K_d of unmodified DOPC protocells (no peptide) for Hep3B, and the K_d values of SP94-targeted DOPC protocells (~240 peptides/particle) for human hepatocytes, endothelial cells (human umbilical vein endothelial cells, or HUVECs), peripheral blood mononuclear cells (PBMCs), B-lymphocytes, and T-lymphocytes. SP94-targeted DOPC protocells have a 10^4-fold higher affinity for HCC than for control cells, providing the specificity necessary for efficacious delivery. All error bars represent 95% confidence intervals (1.96 σ) for n = 5.

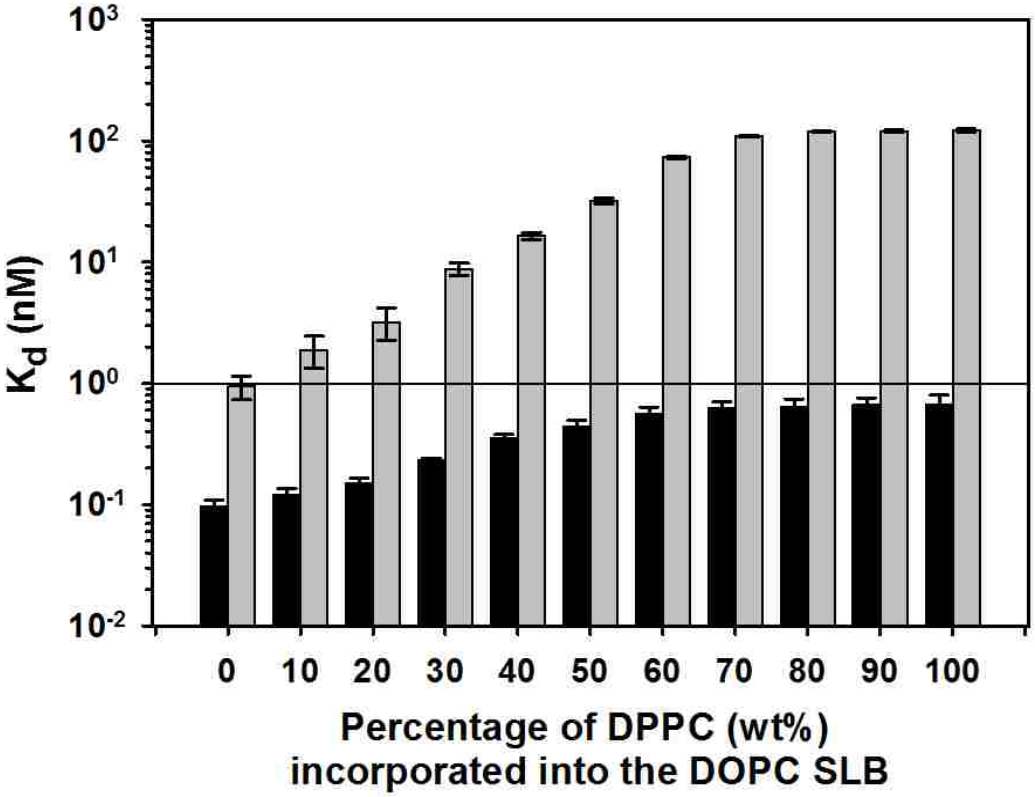

Supplementary Figure 3. The K_d values of protocells can be precisely modulated from 0.10 nM to 100 nM by simply incorporating various amounts of fluid (DOPC) and non-fluid (DPPC) lipids into the SLB. K_d values of DOPC protocells modified with 0.500 wt% SP94 (■) remain fairly constant as increasing amounts of DPPC are incorporated into the SLB. Conversely, the K_d values of DOPC protocells modified with 0.015 wt% SP94 (■) increase with increasing DPPC concentration. All error bars represent 95% confidence intervals (1.96 σ) for n = 5.

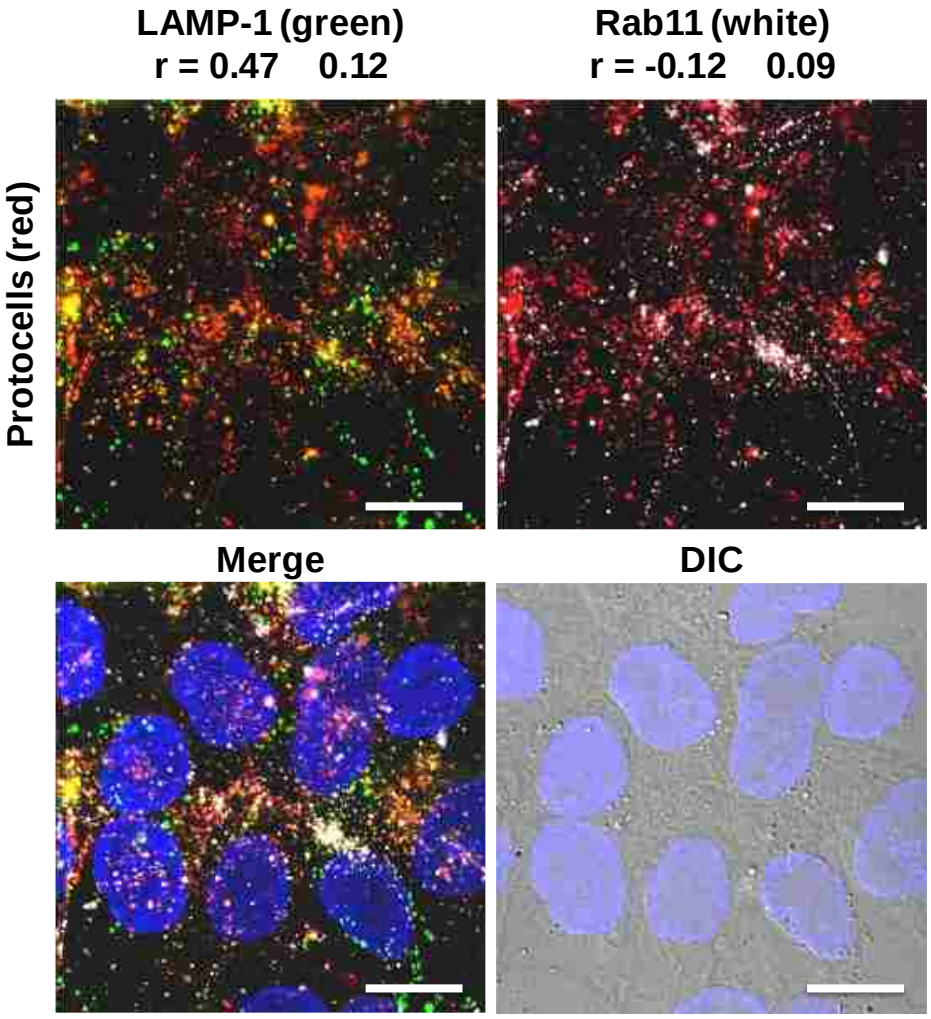

Supplementary Figure 4. The SP94 peptide directs protocells to lysosomes upon endocytosis by HCC, as evidenced by the positive Pearson's correlation (r) between SP94-targeted DOPC protocells (labeled with 5 wt% Texas Red DHPE) and lysosome-associated membrane protein-1 (labeled with Alexa Fluor 488). Conversely, the Pearson's correlation between protocells and Rab11 (labeled with Alexa Fluor 647) is ≈ 0, which indicates that protocells are not localized within $Rab11^+$ recycling endosomes. Differential Interference Contrast (DIC) images were employed to define the boundaries of Hep3B cells, the nuclei of which are labeled with DAPI, such that pixels outside of the cell boundaries could be disregarded when calculating Pearson's correlation coefficients (expressed as the mean value ± the standard deviation for n = 3 x 50 cells). Scale bars = 10 μm.

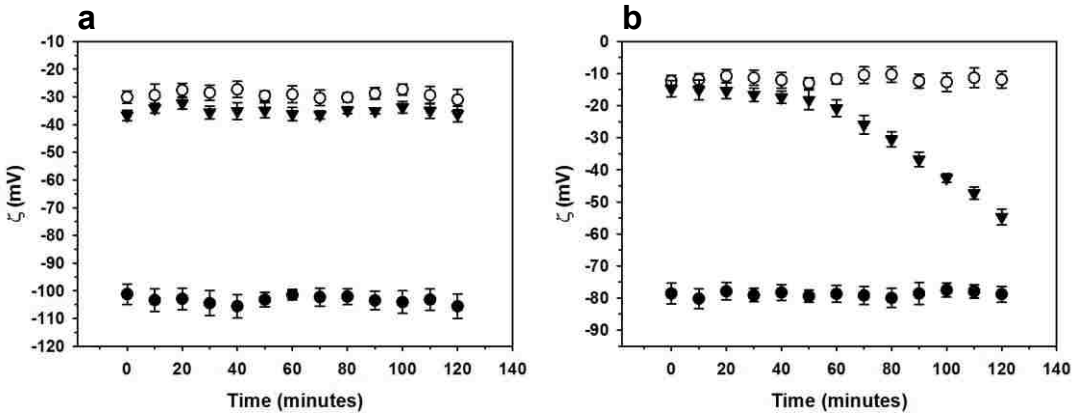

Supplementary Figure 5. Zeta potential (ζ) values of DOPC liposomes (○), DOPC protocells (▼), and nanoporous silica cores (●) when exposed to 1 mM KCl at pH 7 (a) or 1 mM KCl at pH 5 (b) for 2 hours. Acidic conditions destabilize the SLB, as evidenced by the time-dependent decrease in the zeta potential of DOPC protocells when exposed to the pH 5 buffer. Zeta potential values of DOPC liposomes and silica nanoparticles at pH 7 and pH 5 correlate well with those that have been reported previously[31]. All error bars represent 95% confidence intervals (1.96 σ) for n = 3.

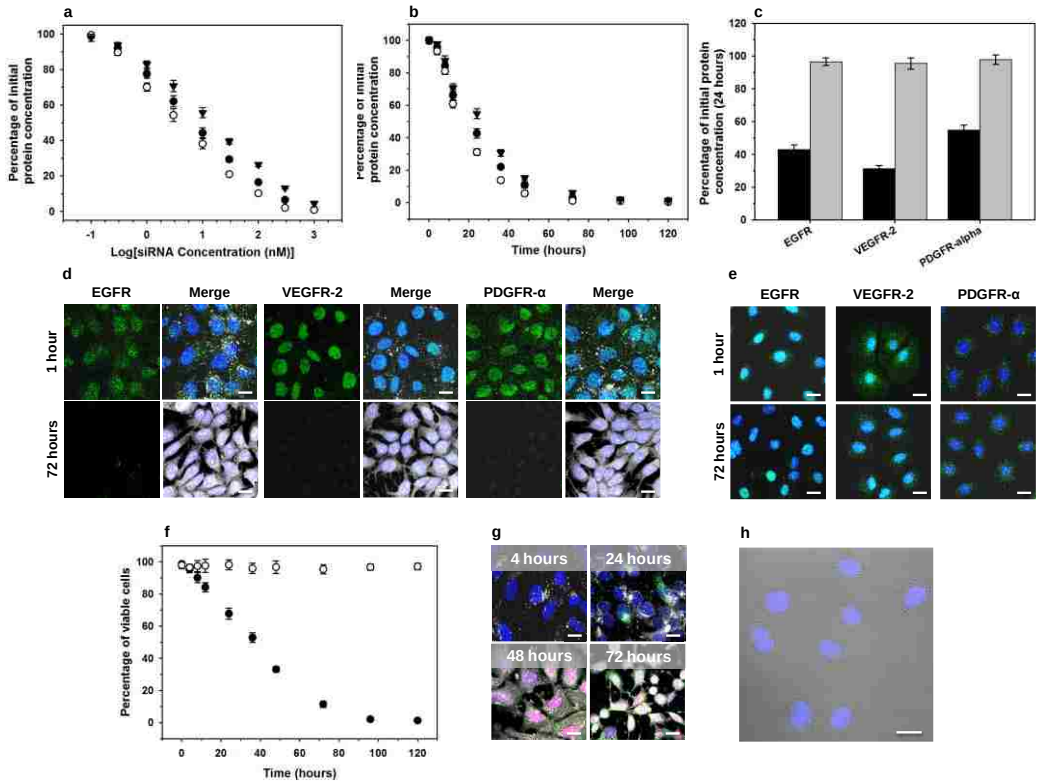

Supplementary Figure 6. Delivery of a siRNA cocktail to HCC via SP94-targeted protocells with 'bimodal' nanoporous cores. Bimodal silica nanoparticles (see Supplementary Methods) have large (10-30 nm), surface-accessible pores that can be rapidly loaded with siRNA, protein toxins, and other high molecular weight cargos. (a) and (b) SP94-targeted protocells loaded with a siRNA cocktail that silences expression of epidermal growth factor receptor (EGFR), vascular endothelial growth factor receptor-2 (VEGFR-2), and platelet-derived growth factor receptor-α (PDGFR-α) induce a dose- (a) and time-dependent (b) decrease in target protein concentrations (determined via immunofluorescence) when exposed to Hep3B. The concentrations of protocell-delivered siRNA necessary to silence 50% of EGFR (●), VEGFR-2 (○), and PDGFR-α (▼) expression (IC_{50}) within 24 hours are 6.68 nM, 4.18 nM, and 12.8 nM, respectively (a). Protocells loaded with the siRNA cocktail decrease EGFR (●), VEGFR-2 (○), and PDGFR-α (▼) concentrations by >90% within 72 hours at a total siRNA concentration of 10 nM (b). (c) SP94-targeted protocells loaded with 10 nM of the siRNA cocktail reduce EGFR, VEGFR-2, and PDGFR-α expression in Hep3B (■) but not hepatocytes (■). (d) and (e) Confocal fluorescence microscopy was utilized to confirm that SP94-targeted protocells are exclusively endocytosed by Hep3B (d) and, therefore, do not induce a decrease in EGFR, VEGFR-2, or PDGFR-α concentrations when exposed to hepatocytes (e). Upon endocytosis by Hep3B, SP94-targeted protocells with Alexa Fluor 647-labeled nanoporous cores (white) are initially (1 hour) localized within endosomes but become dispersed in the cytosol within 4 hours; over the course of 72 hours, siRNA molecules are released from the nanoporous core and silence nearly all EGFR, VEGFR-2, and PDGFR-α (green) expression. (f) – (h) SP94-targeted protocells loaded with 10 nM of the siRNA cocktail kill 50% of Hep3B (●) within 36 hours without affecting the viability of hepatocytes (○). Upon exposure to siRNA-loaded protocells, Hep3B cells become positive for Alexa Fluor 488-labeled annexin V (green) within 24 hours and double-positive for annexin V and propidium iodide (red) within 48 hours (g). Hepatocytes remain double-negative for annexin V and propidium iodide when exposed to SP94-targeted protocells loaded with siRNA for > 1 week (h). All error bars represent 95% confidence intervals (1.96 σ) for n = 3. Nuclei are stained with DAPI in all fluorescence images. Scale bars = 20 μm.

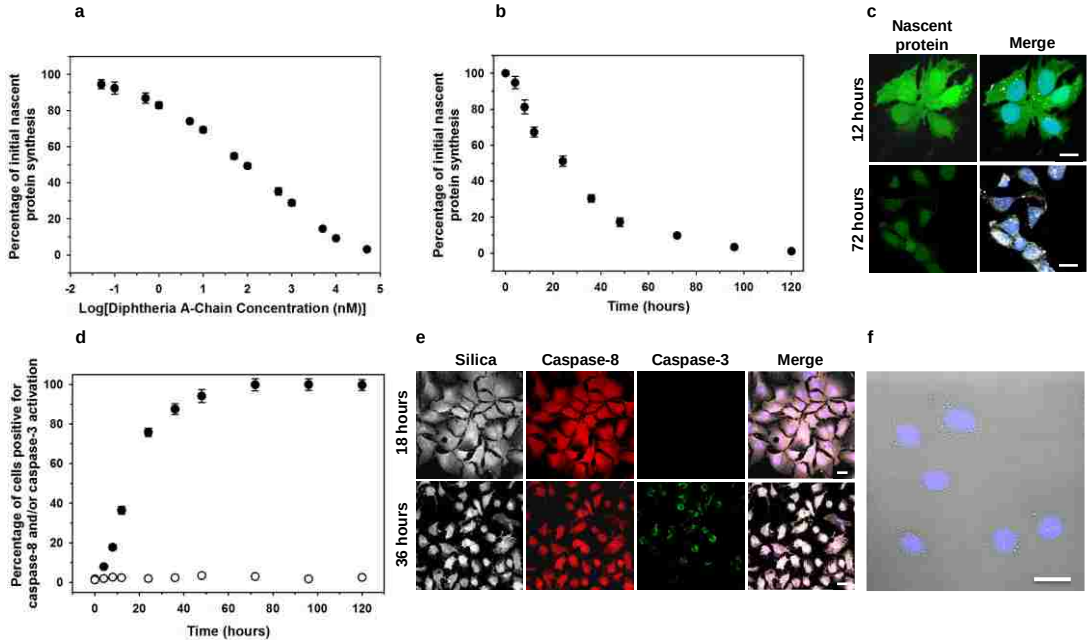

Supplementary Figure 7. Delivery of diphtheria toxin A-chain to HCC using SP94-targeted protocells with bimodal nanoporous cores. Diphtheria toxin is an exotoxin secreted by *Corynebacterium diphtheriae* that is composed of two subunits (A and B) held together by a disulfide bond. The B-chain (39 kDa) facilitates receptor-mediated endocytosis of the toxin, while the A-chain (24 kDa) inhibits protein synthesis in eukaryotic host cells by using NAD as a substrate to catalyze the ADP-ribosylation of aminoacyl-transferase II (EF-2)[32]. Active A-chain can be generated by exposing the native toxin to trypsin and a reducing agent (e.g. dithiothreitol). (a) SP94-targeted protocells loaded with diphtheria toxin A-chain cause a dose-dependent decrease in nascent protein synthesis when exposed to Hep3B for 24 hours. The IC_{50} value of toxin-loaded protocells is 92.0 nM. (b) and (c) Protocells that encapsulate 100 nM of diphtheria toxin A-chain cause a 50% reduction in nascent protein synthesis within 24 hours and a 90% reduction within 72 hours. Nascent protein synthesis was quantified using an Alexa Fluor 488-labeled derivative of methionine (green), and protocell endocytosis by Hep3B was tracked using Alexa Fluor 647-labeled nanoporous cores (white). (d) Diphtheria toxin A-chain delivered via SP94-targeted protocells induces apoptosis in 50% of Hep3B cells (●) within ~18 hours at concentrations < 100 nM but has no cytotoxic effect on hepatocytes (○). (e) Toxin-loaded protocells with Alexa Fluor 647-labeled cores (white) induce caspase-8 activation (red) within 18 hours and capase-3 activation (green) within 36 hours when exposed to Hep3B. (f) SP94-targeted protocells loaded with diphtheria toxin A-chain induce neither caspase-8 nor caspase-3 activation when exposed to hepatocytes for > 1 week. All error bars represent 95% confidence intervals (1.96 σ) for n = 3. Nuclei are stained with DAPI in all fluorescence images. Scale bars = 20 μm.

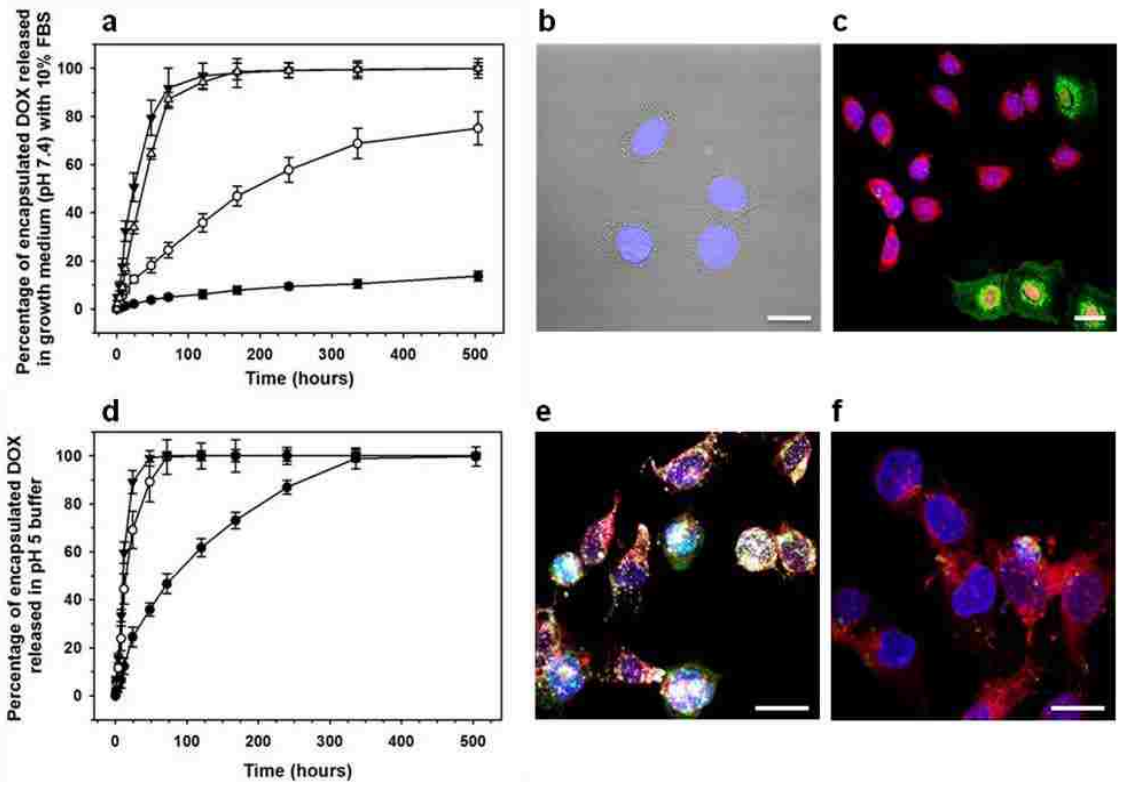

Supplementary Figure 8. Release of doxorubicin (DOX) from protocells and liposomes under neutral and acidic pH conditions. (a) The time-dependent release of DOX from DOPC protocells (●), DSPC liposomes (○), DOPC liposomes (▼), and nanoporous cores (Δ) when exposed to growth medium (EMEM) with 10% fetal bovine serum (FBS) at pH 7.4. Protocells exhibit long-term stability that is independent of the SLB composition: given that their SLBs remain fully intact, DOPC-coated protocells release a negligible amount of DOX when maintained in complete growth medium at 4°C for > 3 weeks. Conversely, DOPC liposomes release nearly all of their encapsulated DOX within 72 hours. Thus, the fluid lipids that enable selective targeting at low peptide densities cannot be used in liposomal drug formulations since pre-mature release of encapsulated cargo results in non-specific toxicity to healthy cells; stable formulations of liposomal drugs require the use of fully saturated, high T_m lipids and high concentrations of cholesterol, which act cooperatively to increase the lipid packing density and limit diffusion of the drug across the bilayer[33]. The stability of 'gold standard' liposomal doxorubicin (e.g. DSPC with 30 mol% cholesterol, loaded using an ammonium sulfate gradient approach) remains limited, however, as up to 30% of the drug is released within 72 hours when stored in complete growth medium. (b) and (c) DOX-loaded protocells are stable under neutral pH conditions and in the presence of serum proteins; they are, therefore, non-toxic to hepatocytes (b). Pre-mature release of DOX from DSPC and DOPC liposomes results in intracellular accumulation of DOX (red) within hepatocytes, as well as non-specific cytotoxicity (c). Non-viable cells are labeled with a green fluorophore that can permeate the compromised membranes of apoptotic and necrotic cells. (d) The time-dependent release of DOX from DOPC protocells (●), DSPC liposomes (○), and DOPC liposomes (▼) when exposed to a pH 5 citric acid buffer. Acidic conditions destabilize the SLB and promote release of DOX from the nanoporous core. (e) and (f) SP94-targeted protocells, the cores of which are labeled with Alexa Fluor 647 (white), can deliver high enough concentrations of DOX to MDR Hep3B to induce rapid cell death (e). SP94-targeted DSPC and DOPC liposomes deliver DOX to the cytosol of MDR Hep3B but in insufficient concentrations to induce cytotoxicity (f). All error bars represent 95% confidence intervals (1.96 σ) for n = 3. Nuclei are stained with DAPI in all fluorescence images. Scale bars = 20 μm.

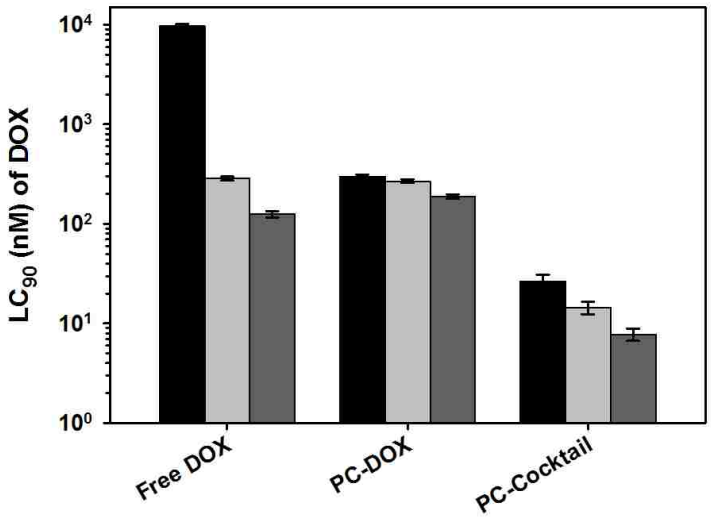

Supplementary Figure 9. The concentrations of free DOX, DOX-loaded protocells (PC-DOX), and protocells that encapsulate a cocktail of DOX, 5-fluorouracil (5-FU), and cisplatin (PC-Cocktail) that are necessary to kill 90% of Hep3B with induced MDR (■), parental Hep3B (■), or MDR Hep3B exposed to cyclosporin A (CsA), which inhibits the Pgp efflux mechanism (■). Hep3B and HepG2 naturally express low-to-moderate levels of P-glycoprotein (Pgp)[34], the over-expression of which is a common cause of MDR in various types of cancer cells. However, as Pgp expression is highly heterogeneous in HCC[34], we have induced MDR in parental Hep3B via chronic exposure to DOX. Nanocarriers that are internalized via receptor-mediated endocytosis processes are typically able to circumvent the Pgp efflux mechanism and can, therefore, induce cytotoxicity in MDR cells at lower drug concentrations. DOX delivered via SP94-targeted protocells is capable of killing 90% of Hep3B with induced MDR (LC_{90}) at a concentration that is nearly 100-fold less than the LC_{90} value of free DOX (9.7 μM); protocells can decrease this value by another order of magnitude due to their ability to simultaneously deliver DOX, as well as 5-FU and cisplatin, neither of which are substrates for Pgp[34,35]. All error bars represent 95% confidence intervals (1.96 σ) for n = 3.

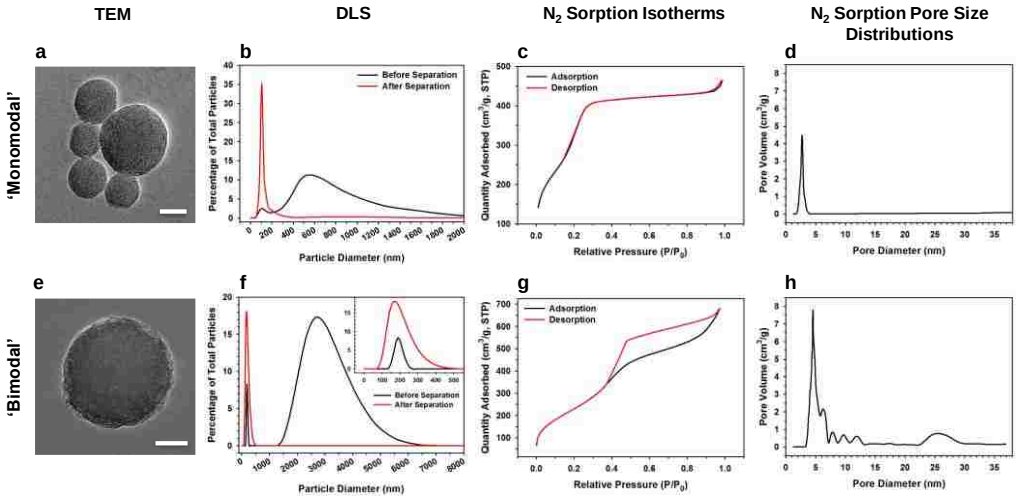

Supplementary Figure 10. Characterization of the two types of nanoporous silica particles employed as protocell cores. The nanoporous silica particles that form the core of the protocell are prepared, as previously described by us[36,37], from a homogenous mixture of water-soluble silica precursor(s) and amphipathic surfactant(s) using either aerosol-assisted evaporation-induced self-assembly (EISA) or by solvent extraction-driven self-assembly within water-in-oil emulsion droplets (see Supplementary Methods for more details). Solvent evaporation or extraction concentrates the aerosol or emulsion droplets in surfactant(s), which directs the formation of periodic, ordered structures, around which silica assembles and condenses. Surfactants are removed via thermal calcination, which results in porous nanoparticles with well-defined, uniform pore sizes and topologies. Transmission electron microscopy (TEM, scale bars = 50 nm), dynamic light scattering (DLS), and nitrogen sorption indicate that particles formed via aerosol-assisted EISA ('monomodal' particles) possess an average diameter of approximately 100-nm (after size exclusion-based separation), a Brunauer−Emmer−Teller (BET) surface area in excess of 1200 m^2/g, a pore volume fraction of about 50%, and a unimodal pore diameter of 2.5-nm. Particles formed within emulsion droplets ('bimodal' particles) have an average diameter of ~150-nm, a BET surface area of >600 m^2/g, a pore volume fraction of ~65%, and a bimodal pore morphology composed of large (10-30 nm), surface-accessible pores interconnected by 6-nm pores. Importantly, the liquid-vapor or liquid-liquid interfacial tensions associated with aerosol or emulsion processing (respectively) enforce a spherical shape with minimal surface roughness. Both types of particles have fully accessible three-dimensional pore networks, as evidenced by TEM imaging and analysis of nitrogen sorption isotherms. The high pore volume, surface area, and accessibility of the nanoporous silica cores imparts a high cargo capacity and enables rapid loading of multiple types of therapeutic and diagnostic agents. Monomodal nanoporous cores have a high capacity for low molecular weight chemotherapeutic agents, while bimodal cores possess the large, surface-accessible pores necessary for encapsulation of siRNA, protein toxins, and other high molecular weight cargos. The rate of cargo release can be precisely controlled by the degree to which the silica core is condensed. Incorporating various amounts of AEPTMS, an amine-containing silane, into the sol used to form the nanoporous silica cores reduces the level of achievable condensation and promotes more rapid dissolution of the cores under neutral pH, high ionic strength (i.e. cytosolic) conditions. Particles that contain no AEPTMS dissolve over the course of 2 weeks, while particles that contain 30 mol% AEPTMS dissolve within 24 hours (data not shown). Protocells can, therefore, be adapted for applications requiring continuous or burst release profiles.

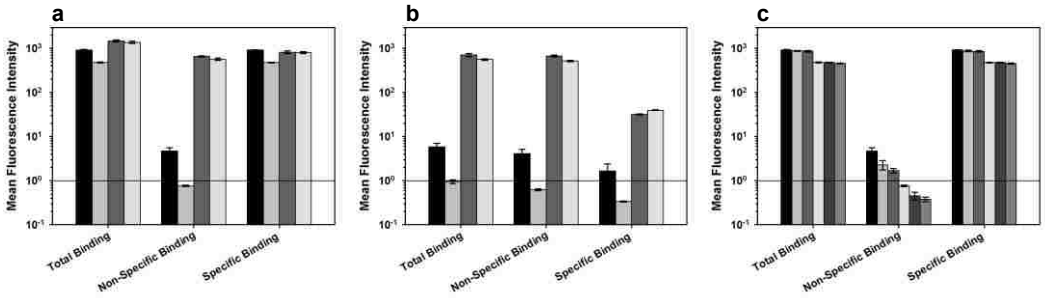

Supplementary Figure 11. The non-specific affinity of protocells modified with 0.500 wt% of the SP94 peptide (~240 peptides/particle) for Hep3B and hepatocytes is a function of the charge and fluidity of lipids employed in the SLB and the degree to which the SLB is modified with cholesterol or PEG. (a) and (b) The affinity of SP94-targeted DOPC (■), DPPC (■), DOTAP (■), and DOPG (■) protocells for Hep3B (a) and hepatocytes (b). Total binding is defined as the mean fluorescent intensity (MFI) of cells exposed to a saturating concentration of SP94-targeted protocells (labeled with 1 wt% Texas Red DHPE), while non-specific binding is defined as the MFI of cells exposed to a saturating concentration of unmodified protocells (labeled with 1 wt% Texas Red DHPE). Specific binding is the difference between total binding and non-specific binding. Lipids with a net positive (DOTAP) or negative charge (DOPG) increase the non-specific binding of protocells to both HCC and hepatocytes. Employing zwitterionic lipids in the SLB minimizes non-specific binding and maximizes specific binding; DPPC protocells have a slightly lower non-specific affinity for Hep3B and hepatocytes than DOPC protocells. (c) The affinity of DOPC (■), DOPC with 30 wt% cholesterol (■), DOPC with 5 wt% PEG-2000 (■), DPPC (■), DPPC with 30 wt% cholesterol (■), and DPPC with 5 wt% PEG-2000 (■) protocells for Hep3B. Incorporating cholesterol or PEG-2000 PE into the SLB further reduces the non-specific binding of DOPC and DPPC protocells to HCC. All error bars represent 95% confidence intervals (1.96 σ) for n = 3.

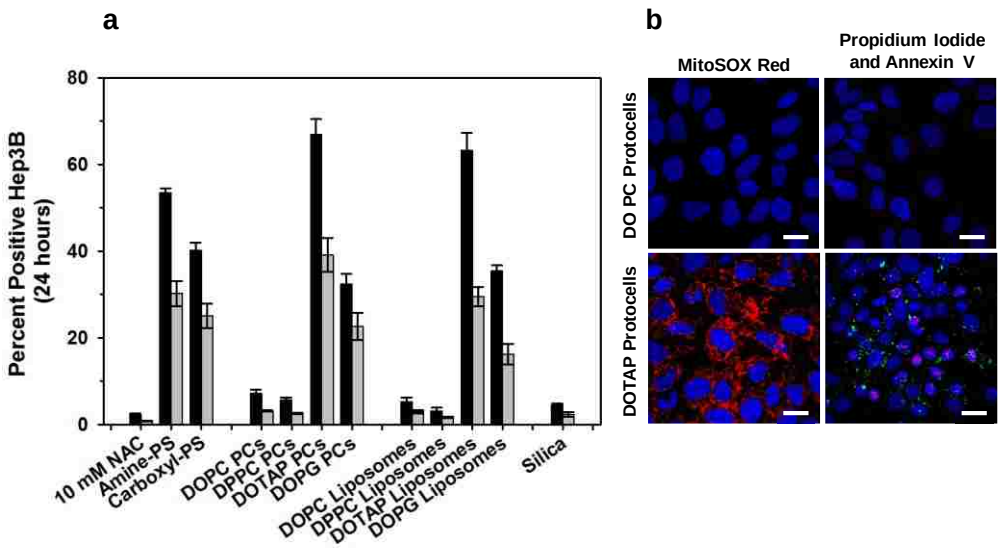

Supplementary Figure 12. The non-specific toxicity of protocells is a function of the charge of lipids employed in the SLB. (a) The degree to which 'empty' SP94-targeted protocells and liposomes induce oxidative stress and subsequent cell death in Hep3B was determined using MitoSOX Red (■), a mitochondrial superoxide indicator that fluoresces in the presence of superoxide anions, and propidium iodide (■), respectively. Protocells and liposomes with bilayers composed of cationic (DOTAP) or anionic (DOPG) lipids induce oxidative stress in up to 60% of Hep3B within 24 hours, while fewer than 10% of Hep3B cells were positive for MitoSOX Red fluorescence upon exposure to protocells and liposomes with bilayers composed of zwitterionic lipids (DOPC or DPPC). Silica nanoparticles alone had little effect on Hep3B viability. Positively- and negatively-charged polystyrene nanoparticles (amine-PS and carboxyl-PS, respectively) were employed as positive controls[38], while Hep3B exposed to 10 mM of the antioxidant, N-acetylcysteine (NAC), was used as a negative control. All error bars represent 95% confidence intervals (1.96 σ) for n = 3. (b) Confocal fluorescence microscopy was used to confirm that Hep3B cells become positive for MitoSOX Red, as well as Alexa Fluor 488-labeled annexin V (green) and propidium iodide (red) upon exposure to DOTAP protocells for 24 hours. Nuclei are stained with DAPI. Scale bars = 20 μm.

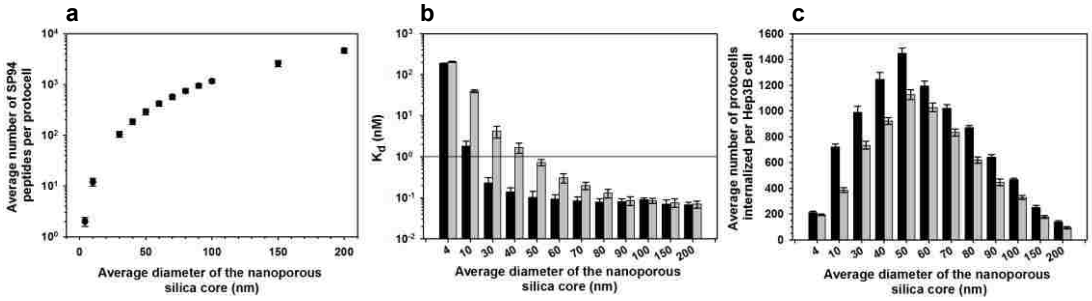

Supplementary Figure 13. The overall diameter of the nanoporous core affects the achievable ligand density, the specific affinity, and the average number of protocells endocytosed by a single HCC cell. (a) As the diameter of the nanoporous core is increased from 4-nm to 200-nm, the SP94 density that is achievable under saturating conditions (when 10 wt% DOPE is incorporated into the SLB) increases from 2 to >4000 peptides per protocell. (b) Since protocells with larger cores can display higher densities of the SP94 peptide, they have a higher affinity (i.e. lower K_d values) for Hep3B. The dependence of K_d on the diameter of the nanoporous core is less pronounced for DOPC (■) protocells than for DPPC (■) protocells; since peptides can be recruited to the Hep3B surface when displayed on a fluid SLB, DOPC protocells can retain high specific affinity at low peptide densities. (c) As the diameter of the nanoporous core increases, fewer SP94-targeted DOPC (■) and DPPC (■) protocells are endocytosed by each Hep3B cell, which is, presumably, due to the observation that membrane wrapping occurs most effectively for 30- to 60-nm particles[39]. All error bars represent 95% confidence intervals (1.96 σ) for n = 3.

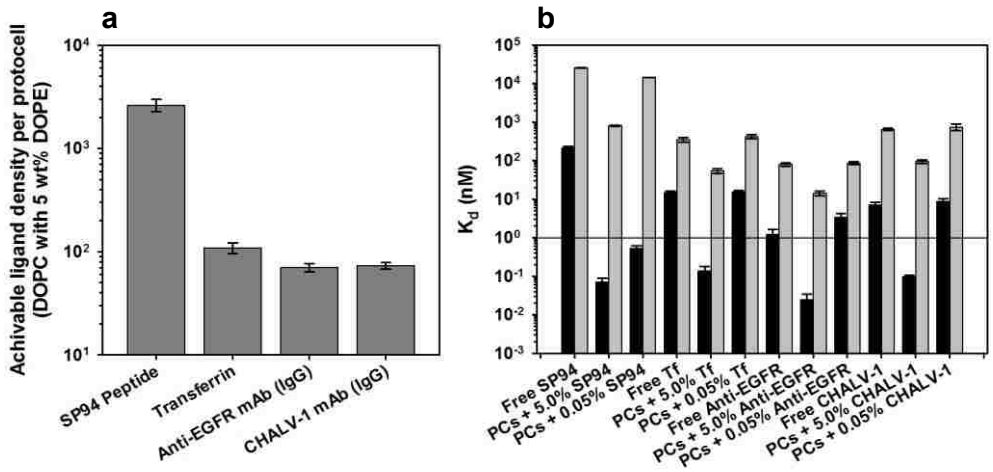

Supplementary Figure 14. We modified the SLBs of protocells with various types of targeting ligands that have an affinity for human hepatocellular carcinoma (HCC) in order to promote selective uptake and multicomponent cargo delivery: the SP94 peptide, which was identified by Lo *et al.* to bind to HCC; diferric transferrin (Tf), a glycoprotein involved in iron transport that binds to a receptor (transferrin receptor, or TfR) upregulated by certain HCC cell lines[40]; a monoclonal antibody against epidermal growth factor receptor (EGFR), which is overexpressed by many types of HCC[41]; and a monoclonal antibody against an unknown HCC surface antigen (CHALV-1; Abcam; Cambridge, MA). (a) The maximum number of ligands that can be conjugated to each protocell when DOPE is incorporated into the SLB at 5 wt% and when protocells are incubated with a saturating ligand concentration. Transferrin (~80 kDa, 8 x 10 nm[42]) and IgG (~150 kDa, 14.2 x 8.5 x 3.8 nm[43] are 1000X larger than the SP94 peptide (~1500 Da); their achievable densities are, therefore, 25- and 40-fold less (respectively) than that of SP94. (b) K_d values for the free ligands, as well as for DOPC protocells modified with a high (5.0 wt%) or low (0.05 wt%) density of each ligand when exposed to Hep3B (■) and hepatocytes (■). Only protocells modified with SP94 retain their affinity for Hep3B at low ligand densities; protocells modified with a low density of Tf, anti-EGFR, or CHALV-1 have K_d values similar to that of the monovalent ligand. Furthermore, SP94 has the lowest inherent affinity for hepatocytes, which is likely due to the fact that TfR, EGFR, and the HCC surface antigen targeted by CHALV-1 are not only expressed by HCC but by hepatocytes as well. Given that DOPC protocells modified with a low density of SP94 (0.05 wt%) possess the highest achievable ligand density, the highest affinity for HCC, and the lowest affinity for human hepatocytes, we chose to employ SP94 as the targeting ligand in the majority of our studies. All error bars represent 95% confidence intervals (1.96 σ) for n = 3.

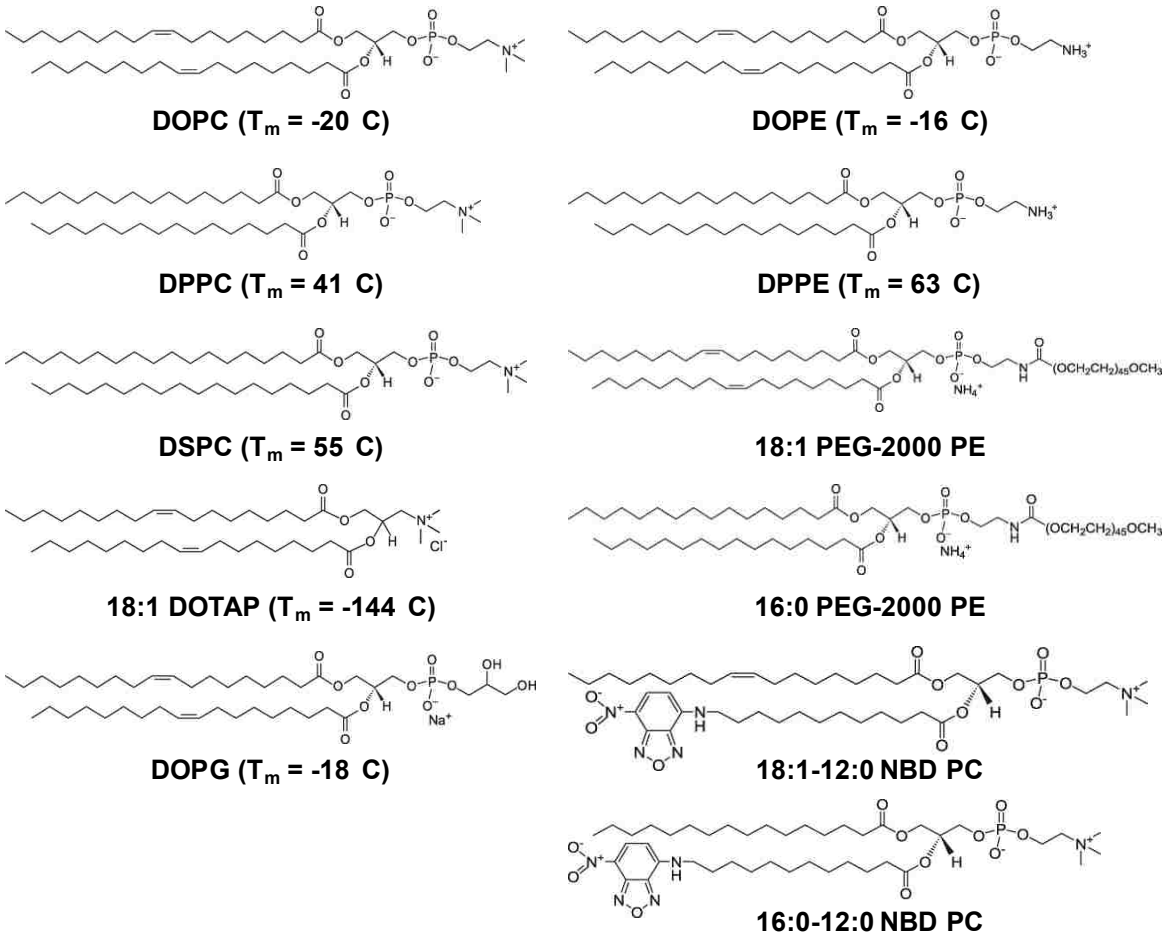

Supplementary Figure 15. Structures of lipids employed in the SLB of protocells.

Supplementary References:

31 Zimmermann, R. *et al.* Charging and structure of zwitterionic supported bilayer lipid membranes studied by streaming current measurements, fluorescence microscopy, and attenuated total reflection Fourier transform infrared spectroscopy. *Biointerphases* **4**, 1-6 (2009).

32 Honjo, T., Nishizuka, Y., Hayaishi, O. & Kato, I. Diphtheria Toxin-dependent Adenosine Diphosphate Ribosylation of Aminoacyl Transferase II and Inhibition of Protein Synthesis. *Journal of Biological Chemistry* **243**, 3553-3555 (1968).

33 Drummond, D. C., Meyer, O., Hong, K., Kirpotin, D. B. & Papahadjopoulos, D. Optimizing Liposomes for Delivery of Chemotherapeutic Agents to Solid Tumors. *Pharmacol Rev* **51**, 691-744 (1999).

34 Tong, A. W. *et al.* Chemosensitization of human hepatocellular carcinoma cells with cyclosporin A in post-liver transplant patient plasma. *Clin. Cancer Res.* **2**, 531-539 (1996).

35 Shen, X., Chen, G., Zhu, G. & Fong, W.-F. (±)-3'-O, 4'-O-dicynnamoyl-cis-khellactone, a derivative of (±)-praeruptorin A, reverses P-glycoprotein mediated multidrug resistance in cancer cells. *Bioorganic & Medicinal Chemistry* **14**, 7138-7145 (2006).

36 Carroll, N. J., Pylypenko, S., Atanassov, P. B. & Petsev, D. N. Microparticles with Bimodal Nanoporosity Derived by Microemulsion Templating. *Langmuir*, doi:10.1021/la900988j (2009).

37 Lu, Y. F. *et al.* Aerosol-assisted self-assembly of mesostructured spherical nanoparticles. *Nature* **398**, 223-226 (1999).

38 Xia, T. *et al.* Comparison of the Mechanism of Toxicity of Zinc Oxide and Cerium Oxide Nanoparticles Based on Dissolution and Oxidative Stress Properties. *ACS Nano* **2**, 2121-2134, doi:10.1021/nn800511k (2008).

39 Jiang, W., KimBetty, Y. S., Rutka, J. T. & ChanWarren, C. W. Nanoparticle-mediated cellular response is size-dependent. *Nat Nano* **3**, 145-150, doi:http://www.nature.com/nnano/journal/v3/n3/suppinfo/nnano.2008.30_S1.html (2008).

40 SCIOT, R. *et al.* Transferrin receptor expression in human hepatocellular carcinoma: an immunohistochemical study of 34 cases. *Histopathology* **12**, 53-63 (1988).

41 Kannangai, R., Sahin, F. & Torbenson, M. S. EGFR is phosphorylated at Ty845 in hepatocellular carcinoma. *Mod Pathol* **19**, 1456-1461 (2006).

42 Ghosh, S., Mukherjee, A., Sadler, Peter J. & Verma, S. Periodic Iron Nanomineralization in Human Serum Transferrin Fibrils13. *Angewandte Chemie International Edition* **47**, 2217-2221 (2008).

43 Sarma, V. R., Silverton, E. W., Davies, D. R. & Terry, W. D. The Three-Dimensional Structure at 6 a Resolution of a Human {gamma}G1 Immunoglobulin Molecule. *J Immunol* **107**, 929-a- (1971).

CHAPTER 2

Multivalent Peptide Display on Virus-like Particles of MS2 Bacteriophage Facilitates Highly Specific Delivery of Cytotoxic Agents to Cancer

It is widely accepted that the pharmacokinetic properties and therapeutic efficacy of many monomeric anti-cancer drugs, as well as drug and gene delivery systems, can be improved through their coupling to ligands that selectively target accessible cellular receptors differentially or over-expressed by diseased cells or tissues, a concept that has been clinically proven to enable dose optimization while mitigating undesirable side effects (1). A plethora of ligands (antibodies and their fragments, peptides, growth factors, glycoproteins, carbohydrates, vitamins, aptamers, etc.) have been utilized to promote specific delivery of therapeutic and diagnostic agents (low molecular weight drugs (2), therapeutic oligonucleotides (3), toxins (4), cytotoxic peptides (5), radionuclides (4), cytokines (6), gold nanoparticles and nanoshells (7), quantum dots (8), iron oxide and other superparamagnetic nanoparticles(9), gadolinium-based contrast agents (10), etc.) to a wide variety of human cancers *in vitro* and *in vivo*. Therapeutic and diagnostic agents can be directly conjugated to the targeting ligand (e.g. immunotoxins) or loaded, via complexation or encapsulation, into a protein, polymer, or inorganic particle that is modified with the targeting ligand. An astonishing number of targeted

delivery systems have been developed since Moolten and Cooperband reported the first tumor-specific immunotoxin in 1970 (11), including a multitude of nanoparticles (liposomes, dendrimers, polymeric nanoparticles and micelles, carbon nanotubes, inorganic nanoparticles, plant and animal viruses, bacteriophages, virus-like particles, etc.) that rely on passive and active targeting mechanisms to direct their accumulation at the tumor site and to promote their selective internalization by tumor cells (12).

Nanoparticles ≤ 150-200 nm in diameter are capable of escaping capture by the reticuloendothelial system (RES) and become concentrated in the tumor interstitium due to the enhanced permeability of disorganized tumor vasculature, as well as the decreased draining efficacy of tumor lymphatics (i.e. the so-called enhanced permeability and retention, or EPR, effect) (13). Nanoparticles can, furthermore, be surface-modified with hydrophilic polymers, such as poly(ethylene glycol) (PEG), to reduce non-specific interactions with serum proteins and endothelial cells, mitigate uptake by RES macrophages, and decrease the magnitude of the humoral immune response (14). Nanoparticles modified with tumor-specific ligands can home to tumor sites and, via receptor-mediated endocytosis, deliver cytotoxic agents directly to the cytosol of tumor cells, which increases the therapeutic index of many drugs and can circumvent or overwhelm the P-glycoprotein (Pgp) efflux mechanism that contributes to multiple drug resistance (MDR), a phenotype exhibited by numerous types of cancers (15). The targeting efficacy of nanoparticle-based delivery systems depends on the inherent affinity of the ligand for its cognate receptor, as well as the density of ligands displayed on the nanoparticle surface. Monoclonal antibodies have been widely used to home nanoparticles to various cell types due to their characteristically high specific affinity (K_d

≤ 1 nM, typically) for the target receptor; their clinical utility can, however, be limited by their size (~160 kDa), which precludes efficient tumor penetration, as well as their immunogenicity and non-specific uptake by the RES, which can cause dose-limiting toxicity (16). Combinatorial-based techniques, including phage display and SELEX (systematic evolution of ligands by exponential enrichment), have been utilized to evolve high affinity peptides, antibody fragments (e.g. Fab and scFv fragments, single VH domains, etc. (17)), and aptamers, which, due to their reduced size (0.50 – 25 kDa), can more effectively penetrate tumors, are typically not recognized by the mononuclear phagocytic system, are less likely to initiate immune responses, and can be displayed in high densities on the surfaces of nanoparticles (16). Multivalent display of targeting ligands dramatically increases the binding avidity of nanoparticles, often by three to five orders of magnitude with respect to the monovalent ligand, which decreases the rate of nanoparticle dissociation and can lead to more efficient internalization (18).

Targeted nanoparticles can be rapidly loaded with high concentrations of therapeutic and diagnostic agents (relative to the drug concentrations that are achievable via simple conjugation to targeting ligands), mitigate premature degradation of cargo, and increase drug bioavailability. Many nanoparticles have, additionally, been engineered to controllably release encapsulated cargo in the tumor microenvironment or upon endocytosis (19, 20). PEGylated liposomes and dendrimers are extensively studied and form the basis of several FDA-approved nanoparticle-based cancer therapeutics due to their low inherent immunogenicity, as well as their biocompatibility, biodegradability, and high degree of solubility in aqueous solvents (21, 22). Liposomes, dendrimers, and polymeric nanoparticles have a cargo capacity that is limited by their interior volume,

however, and cannot typically be adapted for use in applications requiring multicomponent delivery. Conversely, a number of porous inorganic nanoparticles have been developed that have a high capacity for disparate therapeutic and diagnostic agents and can simultaneously deliver drugs, as well as molecules that increase the sensitivity of fluorescence- and/or magnetic resonance-based imaging (23-27). The biodistribution and non-specific toxicity of these multifunctional nanoparticles must be more thoroughly characterized, however, before their *in vivo* utility is conclusively demonstrated.

Plant and animal viruses, bacteriophages, and virus-like particles have received considerable attention in the past decade for their utility in a wide variety of applications that span multiple scientific disciplines, including peptide-directed formation of inorganic nanomaterials and nanoparticles (28-30), vaccine development (31-33), and targeted delivery of drugs and genes to a wide variety of cell types (34, 35). Viruses and bacteriophages possess numerous characteristics that make them of interest as targeted nanocarriers, including their inherent ability to encapsulate DNA and RNA, as well as their high degree of monodispersity and their ability to be modified with high densities of diverse targeting ligands. Furthermore, filamentous (M13, fd, and f1) and lytic (T7, T4, and λ) bacteriophages have been used as display platforms for complex libraries of randomized peptide or scFv sequences. Phage display is a remarkably powerful, combinatorial-based technique that enables evolution of ligands with a high specific affinity for target cells or cellular receptors without *a priori* knowledge of the amino acid sequence (16, 17, 36, 37). Filamentous phage M13, the basis of most commercially-available display systems, has been extensively utilized to identify targeting ligands that bind to recombinant proteins differentially or over-expressed by cancer cells, as well as

entire cancer cell lines or freshly-excised tumor cells (36, 38). Phage display has, additionally, been used to recover ligands with an affinity for tumor vasculature, extracellular matrix components, and necrotic areas using *in vivo* and *ex vivo* techniques (39, 40). Peptides and antibody fragments identified by phage display are typically conjugated to liposomes or polymeric nanocarriers, which can reduce the affinity of the ligand for its target receptor. Attempts have, therefore, been made to utilize recombinant M13 particles for targeted delivery (34, 41, 42). Filamentous phages, however, selectively package their genome via complex, cooperative interactions between DNA and coat proteins, making it difficult to encapsidate non-genomic materials (43); drugs and other cargo must, therefore, be conjugated to the external surface of their capsids. To circumvent this limitation, researchers have reconstituted coat protein-random peptide fusions in the bilayers of drug-loaded liposomes (44), fused drug-loaded liposomes to M13 bearing tumor-specific peptides (45), and utilized other types of viruses, bacteriophages, and virus-like particles with a cargo capacity.

Adenovirus has been extensively adapted for use in targeted gene therapy due to its natural ability to transfect host cells with double-stranded DNA, including plasmids that encode reporter proteins. Adenoviral vectors are typically PEGylated to suppress the innate immune response and mitigate coxsackievirus-adenovirus receptor (CAR)-mediated endocytosis and modified with tumor-specific ligands to promote selective transfection of cancer cells with the gene of interest (46, 47). Polyomavirus (48, 49), lambda phage (50), and bacteriophage phi-29 (51) have been engineered in a similar manner to deliver reporter genes and siRNA, while the natural affinity of canine parvovirus for transferrin receptor (TfR) has been utilized to promote cell-specific uptake

of parvovirus-like particles (52). Icosahedral plant viruses, including Cowpea chlorotic mottle virus (CCMV) (53), Cowpea mosaic virus (CPMV) (54, 55), and Hibiscus chlorotic ringspot virus (HCRSV) (56), have been emptied of their genomic RNA, loaded with various types of exogenous materials, including gold nanoparticles and chemotherapeutic drugs, and targeted to cancer cells via modification with folic acid or peptides that bind to receptors typically over-expressed by cancer (e.g. vascular endothelial growth factor receptor, or VEGFR).

More recently, virus-like particles (VLPs) of MS2 bacteriophage have been engineered for use in targeted delivery and address several limitations associated with nanocarriers derived from filamentous phages and plant viruses. MS2 VLPs self-assemble from 180 copies of a single coat protein (13.7 kDa) into a perfectly monodisperse, 27.5-nm capsid with icosahedral symmetry (T = 3). The periodicity of the capsid, the presence of surface-accessible amino acid residues with reactive moieties (e.g. lysine and glutamic acid), and the tolerance of a genetically-fused coat protein dimer (the so-called single-chain dimer (33)) for ≥ 90% of peptide insertions enables dense, repetitive display of peptides and antibody fragments via chemical conjugation or genetic insertion and aptamers, vitamins, glycoproteins, etc. via chemical conjugation. Stockley, *et al.* used heterobifunctional crosslinkers to modify MS2 VLPs with transferrin for targeted delivery of ricin A-chain or antisense oligonucleotides to TfR^+ cells (57, 58), while Francis, *et al*. employed lysine residues, as well as an unnatural amino acid (*p*-aminophenylalanine, inserted at position 19 of MS2 coat protein) to link peptides, aptamers, and PEG to the exterior surface of MS2 VLPs and promoted stable encapsulation of chemotherapeutic drugs, Gd-based contrast agents, and fluorescent

molecules via conjugation of cargo to functionalized amino acids present on the interior capsid surface (59-63). Another attractive feature of MS2 VLPs is that their interior volume can be rapidly loaded with a variety of non-genomic materials using several approaches. Hollow capsids can be produced from native bacteriophages via hydrolysis of the genome (64) or by expression of coat protein from a plasmid in transformed *Escherichia coli* (63, 65, 66). The presence of 32 pores, each of which is ~1.8-nm in diameter, in the MS2 capsid enables diffusion of small molecules into the interior volume, a technique that Stockley and Francis have employed to encapsidate antisense oligonucleotides, fluorescent molecules, chemotherapeutic drugs, and Gd-based contrast agents (58, 60, 61, 63). Furthermore, MS2 coat protein naturally self-assembles in the presence of RNA (see below for more details), enabling cargos modified with RNA to be selectively encapsidated within the interior volume, a technique Stockley has employed to load MS2 VLPs with ricin A-chain. Additionally, the abundance of lysine residues on the interior capsid surface suggests that negatively-charged cargos of the appropriate size can be encapsidated within MS2 VLPs via non-specific electrostatic interactions (43). MS2 VLPs are biocompatible, biodegradable, stable under a variety of temperature, pH, and solvent conditions, and are easily synthesized and purified in large quantities using safe, cost-effective procedures. Their structural simplicity enables their synthesis *in vivo* using saturated bacterial cultures, as well as entirely *in vitro* using cell-free protein synthesis systems (67). Finally, Peabody *et al.* are developing MS2 VLPs as a platform for random peptide (33) and scFv (unpublished results) display. MS2 VLPs are the only particles, to date, that possess both the random peptide display capabilities of filamentous phage and the cargo capacity of the hollow capsid.

Here we report the simultaneous delivery of multiple types of chemically disparate therapeutic and diagnostic agents to human hepatocellular carcinoma (HCC) using MS2 VLPs modified with high densities of targeting peptides that have an affinity for HCC (Fig. 1*A*). Peptides conjugated to surface lysine residues present in the VLP capsid or genetically inserted in a surface loop of coat protein are displayed on the VLP surface in dense, repetitive arrays (90-240 copies per VLP) (33). Multivalent display of peptides with an affinity for HCC promotes highly specific surface binding and internalization of MS2 VLPs by HCC (Fig. 1*B*) but not by normal hepatocytes (Fig. 1*C*). MS2 VLPs, furthermore, naturally self-assemble in the presence of RNA, enabling specific encapsidation of therapeutic RNAs, as well as any molecule or nanoparticle (≤ 16-nm in diameter) that can be surface-modified with RNA (Fig. 1*D*). Specific internalization of targeted VLPs combined with the cargo capacity of the hollow capsid enable selective delivery of a variety of cytotoxic and imaging agents to HCC (Fig. 1*E*) without affecting the viability of hepatocytes and other control cells *in vitro*.

Results and Discussion

Modification of Cargo with RNA Promotes Specific Encapsidation of Disparate Therapeutic and Diagnostic Agents within MS2 VLPs. MS2 VLPs can be rapidly loaded with a variety of therapeutic and diagnostic agents and surface modified with ligands, including peptides, aptamers, and transferrin, that promote specific uptake by cancer cells. Several approaches for loading MS2 VLPs with various types of cargos have been reported that either utilize the 1.8-nm pores present in the MS2 capsid to passively diffuse small molecules into the interior volume or employ nucleic acids to drive capsid

assembly (58, 60, 61, 63). MS2 coat protein, when expressed from a plasmid in transformed *E. coli*, can spontaneously form hollow capsids in the absence of RNA (65, 66); hollow capsids can also be formed by exposing MS2 bacteriophage to basic conditions to promote hydrolysis of the genome (64). Soaking hollow capsids in a solution containing the cargo of interest promotes diffusion of the cargo into the interior volume of the capsid; negatively-charged cargos (e.g. RNA and antisense oligonucleotides) are retained via electrostatic interactions with coat protein, while small molecule drugs or fluorophores pre-modified with reactive moieties can form covalent bonds with functionalized amino acids present on the interior capsid surface (59). MS2 coat protein, typically harvested via acetic acid or urea-driven disassembly of native MS2 bacteriophage (57), can also spontaneously assemble into complete capsids upon addition of nucleic acids. The efficacy and rate of capsid assembly are maximized in the presence of the MS2 translational operator, a 19-nucleotide RNA stem-loop that, via its interaction with coat protein, mediates exclusive encapsidation of the MS2 genome during bacteriophage replication (57, 65, 68). The MS2 operator, or *pac* site, can promote efficient encapsidation of non-genomic materials within the interior volume of MS2 VLPs upon conjugation of the *pac* site to the cargo of interest (57, 58). MS2 VLPs will also, however, encapsidate RNA hairpins with sequences that differ from that of the native operator (68), as well as heterologous nucleic acids, including single- and double-stranded RNA and DNA ≤ 3 kbp in length.

We have encapsidated various types of therapeutic (drugs, siRNA, and protein toxins) and imaging (quantum dots) agents within the interior volume of MS2 VLPs (Fig. 1*A*) by exploiting their natural ability to assemble in the presence of both heterologous

nucleic acids and cargos modified with the *pac* site. We used thiol-cleavable, heterobifunctional crosslinkers (e.g. succinimidyl 6-(3-[2-pyridyldithio]-propionamido)hexanoate, or LC-SPDP, which is reactive toward sulfhydryls and primary amines) to conjugate the *pac* site, modified with a 3' sulfhydryl moiety and $(U)_{3\text{-}9}$ spacer, to a CdSe/ZnS core-shell quantum dot, passivated with amine-terminated PEG (Fig. 1*D*), as well as the chemotherapeutic drugs, doxorubicin and cisplatin, both of which contain primary amine groups; the use of crosslinkers that are cleavable via reduction is critical to liberate cytotoxic agents in the cytosol of target cancer cells. We employed a similar strategy to conjugate the *pac* site, modified with a 3' amine moiety, to the A-chain of ricin toxin, which contains a free cysteine residue. To encapsidate a cocktail of doxorubicin, cisplatin, and 5-fluorouracil, we incorporated three internal 5-fluorouridine moieties into the *pac* site sequence, which was further modified with a 5' thiol group to enable conjugation to doxorubicin and cisplatin. To harvest coat protein for the reassembly reaction, we exposed native MS2 bacteriophage to glacial acetic acid, which promotes precipitation of the RNA genome and maturase, as well as disassembly of the capsid into coat protein monomers, and dialyzed resulting monomers against 20 mM acetic acid, which favors the formation of coat protein dimers. Upon addition of buffered siRNA or *pac* site-modified cargo, ninety dimers spontaneously reassemble around the cargo to form a complete, 27.5-nm capsid (Fig. 1*D*). Using this technique, the reassembly reaction yield varied from ~40% to ~90%, depending on the type of cargo; nearly 100% of fully-assembled VLPs contained encapsidated cargo (results not shown). Loading efficiencies for each type of cargo are described below.

To demonstrate that MS2 VLPs are capable of simultaneously encapsidating and delivering a variety of therapeutic and diagnostic agents to HCC, we first incubated an excess of coat protein dimers with a mixture of *pac* site-modified quantum dots and doxorubicin, as well as fluorescently-labeled siRNA and ricin A-chain modified with a fluorescently-labeled derivative of the *pac* site. We then purified fully assembled capsids via size-exclusion chromatography, chemically conjugated a targeting peptide that promotes selective uptake of VLPs by HCC to the capsid surface, and fluorescently-labeled the capsid using Alexa Fluor® 555 hydrazide and 1-ethyl-3-[3-dimethylaminopropyl]carbodiimide hydrochloride (EDC). Upon exposing the HCC cell line, Hep3B, to targeted VLPs loaded with the multicomponent cargo mixture, we employed hyperspectral confocal fluorescence microscopy to individually track the four types of cargo, as well as the capsid, within the cytosol of a Hep3B cell. As is clearly demonstrated in Fig. 1*E*, targeted VLPs can deliver a high payload of chemically disparate therapeutic and imaging agents to cancer cells *in vitro*.

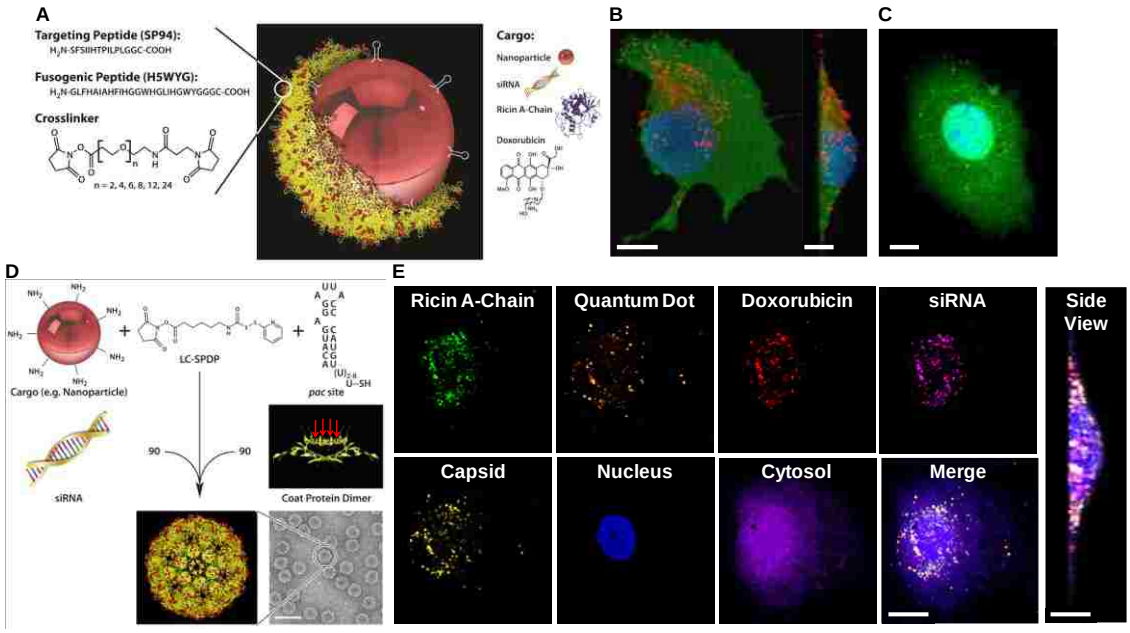

Figure 1. Targeted delivery of disparate therapeutic and diagnostic agents to human hepatocellular carcinoma (HCC) via multivalent display of the SP94 targeting peptide on virus-like particles (VLPs) of MS2 bacteriophage. (A) Various types of cargo can be specifically encapsidated within the interior volume of MS2 VLPs (via the scheme depicted in part D), including nanoparticles, siRNA, protein toxins (e.g. ricin A-chain), and chemotherapeutic agents (e.g. doxorubicin). The surface of the protein capsid (yellow) can, furthermore, be modified in precise locations with functional peptides (red) via chemical conjugation (using a heterobifunctional crosslinker with a PEG spacer arm) in order to target VLPs to a diseased cell or tissue or to promote endosomal escape once VLPs are internalized within the target cell. (B)-(C) VLPs (red) modified with the SP94 targeting peptide are internalized within HCC (B) but not hepatocytes (C), demonstrating that SP94 confers the specificity necessary for efficacious targeted delivery. VLPs are labeled with Alexa Fluor® 555 and cells are labeled with a blue fluorescent nuclear stain (Hoechst 33342) and CellTracker™ Green CMDFA. Scale bars = 10 µm. (D) Various types of cargo can be encapsidated within MS2 VLPs via modification with the *pac* site, a 19-nucleotide RNA hairpin loop present in the bacteriophage genome that is thought to initiate capsid assembly. Primary amine-functionalized cargos are conjugated to the *pac* site, modified with a 3' sulfhydryl moiety, via a heterobifunctional crosslinker (LC-SPDP). Ninety coat protein dimers then self-assemble around siRNA or RNA-modified cargo to form the 27.5-nm capsid. The yield of fully-assembled capsids is depicted in the TEM image of VLPs, each of which encapsidates ~90 siRNAs (scale bar = 50 nm). Arrows point to the locations of surface-accessible lysine residues, which are utilized to conjugate targeting and fusogenic peptides to the capsid surface. (E) Hyperspectral confocal fluorescence imaging can be employed to demonstrate that targeted VLPs are capable of simultaneously delivering a cocktail of ricin A-chain (modified with an Alexa Fluor® 488-labeled derivative of the *pac* site), *pac* site-modified Qdot® 585 ITK™ amino(PEG) quantum dots, *pac* site-modified doxorubicin (naturally emits at 560 nm and 592 nm when dissolved in water [1], and Alexa Fluor® 647-labeled siRNA specifically to HCC Hep3B (labeled with Hoechst 33342 and CellTracker™ Violet BMQC). Scale bars = 20 µm.

Multivalent Display of Targeting Peptides Enhances the Specific Affinity of MS2 VLPs for HCC. MS2 VLPs can be modified with high densities (≥ 30 ligands per VLP) of peptides, aptamers, and other low molecular weight (≤ 25 kDa) targeting ligands through chemical conjugation to surface-accessible amino acids with reactive moieties (e.g. lysine, glutamic acid, etc.) (59, 62, 63). Multivalent display of targeting ligands on a nanoparticle surface enhances the affinity of the monovalent ligand for the target cell or cellular receptor through collective binding effects that promote high avidity interactions between nanoparticles and the target cell surface (18, 63, 69, 70). We have employed peptide, glycoprotein, and antibody-based ligands that are known to bind to HCC to determine how ligand size, inherent affinity, and density influence specific surface binding of MS2 VLPs. The SP94 (H_2N-SFSIIHTPILPL-COOH) peptide, which has an affinity for unknown HCC surface antigen(s), was isolated from a filamentous phage-displayed dodecapeptide library via affinity selection against the HCC cell line, Mahlavu (71). Similarly, the GE11 peptide, which has an affinity for human epidermal growth factor receptor (hEGFR), and the HBsAgP peptide, which has an affinity for Hepatitis B surface antigen (HBsAg), were isolated from dodecapeptide and octapeptide libraries, respectively, by biopanning immobilized hEGFR (recombinant) or HBsAg (purified from the serum of HBV-infected patients) (72, 73). EGFR is over-expressed by many types of cancer, including HCC (74), while HBsAg can be expressed and secreted by HCC derived from hepatocytes chronically infected with HBV (75). In addition to peptide ligands, we employed diferric transferrin (Tf), a glycoprotein involved in iron transport that binds to a receptor (TfR) upregulated by several HCC cell lines (76) and a monoclonal antibody (CHALV-1) against an unknown HCC surface antigen. All peptides

were synthesized with C-terminal cysteine residues (separated from the affinity selected sequence via a $(Gly)_2$ spacer) and conjugated to surface lysine residues present in the MS2 capsid using the heterobifunctional crosslinker, succinimidyl-[(*N*-maleimidopropionamido)-tetracosaethyleneglycol] ester ($SM(PEG)_{24}$, which is reactive toward amine and sulfhydryl groups and contains a PEG spacer arm 9.5-nm in length. Tf and CHALV-1 were first activated with *N*-succinimidyl-S-acetylthioacetate (SATA), which adds protected sulfhydryls to primary amines, and then conjugated to MS2 VLPs using $SM(PEG)_{24}$. Crosslinkers with PEG spacers were used to reduce any steric hindrance that might interfere with ligand binding and to enable PEGylation of the MS2 surface, which reduces non-specific interactions and prevents recognition of MS2 VLPs by anti-MS2 antibodies (see below for more details).

We found that, under saturating conditions, each MS2 VLP can be modified with an average of 246 (± 9) peptides and that the peptide density can be reduced via reaction stoichiometry, as well as reaction time and temperature. Since glycoproteins and antibodies are substantially larger than peptide ligands (~40X and 80X, respectively), the density of Tf and CHALV-1 that is achievable under saturating conditions is more than an order of magnitude lower (Fig. S1*A*) than that of SP94, EC11, and HBsAgP, which limits the avidity of Tf- and CHALV-1-modified VLPs. We quantified the avidity of targeted MS2 VLPs for various HCC cell lines, as well as non-transformed hepatocytes, by measuring dissociation constants (K_d), which are a measure of specific surface binding and inversely proportional to avidity (i.e. low dissociation constants are indicative of high affinity or avidity). Although SP94, EC11, and HBsAgP have a lower inherent affinity for Hep3B than Tf or CHALV-1, MS2 VLPs modified with a high density (~240 peptides

per VLP) of any one targeting peptide have K_d values that are more than an order of magnitude less than the K_d values of Tf- and CHALV-1-modified VLPs (Fig. S1*B*), which highlights the importance of multivalency in maximizing avidity. Although MS2 VLPs modified with SP94, EC11, HBsAgP, Tf, or CHALV-1 have a high avidity for Hep3B, the degree to which they bind to other HCC cell lines, including HepG2 and PLC/PRF/5, strongly depends on the surface density of target receptor(s). Ligands that bind to unknown HCC surface antigen(s), such as SP94 and CHALV-1, have a high specific affinity for HCC, as evidenced by the 10^3-fold difference between their K_d values for Hep3B, HepG2, or PLC/PRF/5 and their K_d values for hepatocytes (Fig. S1*C*). Conversely, VLPs that display the EC11 peptide or Tf bind to HCC only 100-fold more effectively than they bind to hepatocytes due to the varying degree of EGFR (77) and TfR (78) over-expression by HCC, while VLPs that display HBsAgP are highly specific for the HCC cell lines that are positive for HBsAg expression (Hep3B and PCL/PRF/5) but not for $HBsAg^-$ cells lines (HepG2). Given that SP94-targeted MS2 VLPs possess the highest specific affinity for HCC and exhibit the lowest degree of non-specific binding to hepatocytes, we chose to employ SP94 as the targeting ligand in all subsequent experiments.

MS2 VLPs bearing 240 copies of the SP94 peptide have sub-nanomolar avidity for Hep3B, HepG2, and PLC/PRF/5 (Fig. 2*A*), the magnitude of which is retained when HCC cells are co-cultured with hepatocytes (Fig. S2). SP94-modified VLPs, furthermore, have a 500-fold higher affinity for Hep3B than monovalent SP94, a 2000-fold higher affinity for Hep3B than VLPs bearing 240 copies of an irrelevant peptide (H_2N-FPWFPLPSPYGNGGC-COOH (71)), and an 85,000-fold higher affinity for Hep3B than

unmodified VLPs. Importantly, VLPs displaying the SP94 peptide have between a 10,000 and 20,000-fold higher affinity for Hep3B than for human hepatocytes, endothelial cells (HUVECs), and immune cells (peripheral blood mononuclear cells (PBMCs), B-lymphocytes, and T-lymphocytes), providing the specificity necessary for efficacious targeted delivery (Fig. 2*A*). We have utilized atomic force microscopy (AFM) to confirm that SP94-targeted VLPs specifically bind to HCC by employing MS2 VLPs, covalently coupled to a gold-coated AFM tip and modified with high SP94 densities, to probe the surfaces of Hep3B cells before and after addition of exogenous SP94. Fig. 2*D* shows a contour map, superimposed on a fluorescence image of a Hep3B cell, that diagrams adhesion events that occurred between SP94-modified VLPs and unknown antigen(s) on the Hep3B surface. The pattern of adhesion events suggests that target receptor(s) are pre-clustered on the Hep3B surface prior to binding of SP94-targeted VLPs. The histogram in Fig. 2*E* plots observed rupture events, the magnitude of which was largely between 20 and 70 pN. Upon addition of exogenous SP94, the incidence of $\geq$ 40 pN adhesions decreases dramatically, which indicates that the rupture force for specific surface binding of SP94 to HCC is in the range of 40-70 pN (comparable to other biological interactions (79-81)).

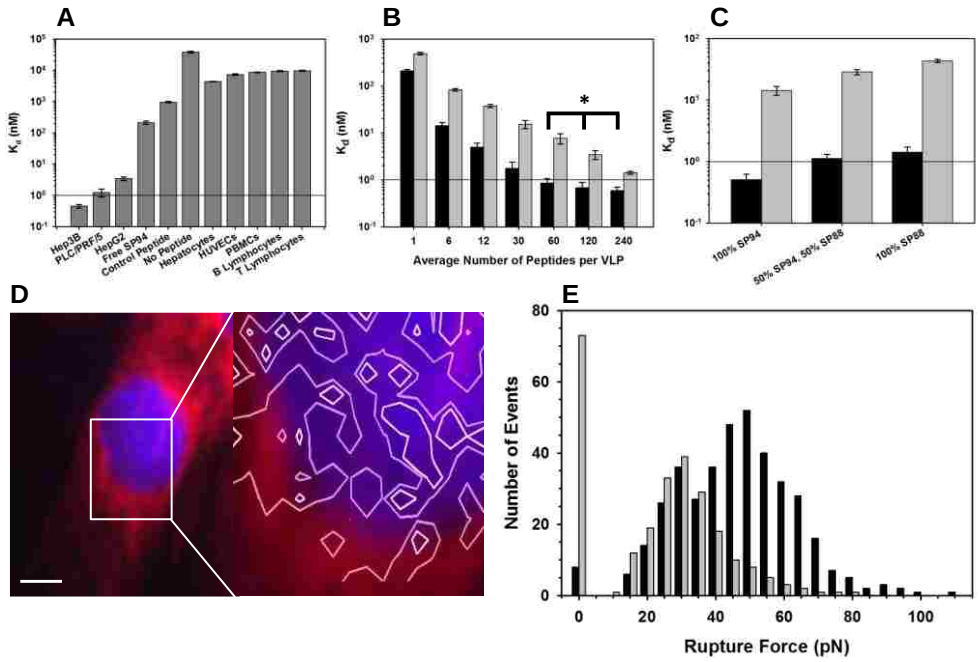

Figure 2. MS2 VLPs modified with the SP94 peptide have a high specific affinity for human HCC, the magnitude of which is dependent on the type(s) and density of targeting peptides. (A) MS2 VLPs modified with 240 copies of the SP94 peptide have a high specific affinity for the HCC lines, Hep3B, PLC/PRF/5, and HepG2, as evidenced by their low K_d values ($\leq$ 1 nM), which are 10^4-fold lower than the K_d of targeted VLPs for hepatocytes, endothelial cells (HUVECs), and immune cells (PBMCs and B- and T-lymphocytes), 500-fold lower than the K_d of free SP94 for Hep3B, 2000-fold lower than the K_d of MS2 VLPs modified with a control peptide (with no known affinity for HCC) for Hep3B, and > 10^4-fold lower than the K_d of unmodified VLPs (no peptide) for Hep3B. The dissociation constant (K_d) is a measure of specific surface binding and is inversely related to affinity (i.e. VLPs with a low K_d value have a high specific affinity for the target cell). (B) The affinity of targeted VLPs for Hep3B is a function of the peptide density and type. SP94 (■) and SP88 (■) targeting peptides are displayed in precise, yet fixed locations on the VLP surface; therefore, the affinity of targeted VLPs for Hep3B decreases (i.e. K_d increases) with decreasing peptide density since multivalent effects are less pronounced at lower peptide densities. SP88 has a lower inherent affinity for Hep3B than SP94; therefore, VLPs modified with SP88 have a lower affinity for Hep3B than VLPs modified with SP94 at all peptide densities. * indicates that the indicated values are NOT significantly different (using ANOVA, $p \sim 0.47$ for $n = 5$). (C) VLPs modified with a combination of SP94 and SP88 retain their overall affinity for Hep3B (K_d ~1 nM) when both peptides are present in an average density of 60 peptides per VLP (■). VLPs modified with ~3 copies each of the SP94 and SP88 peptides have a slightly lower specific affinity for Hep3B (■); reducing the peptide density might reduce the immunogenicity of targeted VLPs, however. (D, left) A fluorescence image of a Hep3B cell, the cytosol of which is stained with CellTracker™ Red CMTPX and the nucleus of which is stained with Hoechst 33342 (blue). Scale bar = 20 µm. (D, right) A contour map demonstrating the pattern and strength of adhesion events between the indicated region of the Hep3B surface and an Atomic Force Microscope (AFM) tip modified with VLPs to which the SP94 peptide is conjugated in high density (~240 peptides per VLP). The pattern of adhesion events with a magnitude in the 40-70 pN range tend to be clustered on the Hep3B surface when the experiment is performed at room temperature. Contours represent 60 pN and 120 pN total rupture force. (E) A histogram plotting the number of adhesion events at various rupture forces demonstrates that an AFM tip modified with VLPs that display the SP94 peptide in high density binds to the surface of a Hep3B cell with high affinity (■), which can be competitively inhibited via the addition of exogenous SP94 (■); the resulting histogram has minimal adhesion events $\geq$ 40 pN, indicating that specific rupture forces are in the 40-70 pN range. All error bars represent 95% confidence intervals (1.96 σ) for $n = 5$.

The avidity of MS2 for HCC is strongly dependent on the density of targeting peptides displayed on the VLP surface, as well as (to a lesser extent) the inherent affinity of the targeting peptide for HCC. As demonstrated in Fig. 2*B*, the affinity of MS2 VLPs for Hep3B remains essentially constant when at least one-third of coat protein monomers are modified with the SP94 peptide (~60 peptides per VLP). As SP94 density decreases, however, the affinity of MS2 VLPs for Hep3B decreases (i.e. K_d values increase), since the multivalent interactions that promote high avidity binding are less pronounced at low ligand densities. Furthermore, the K_d values of MS2 VLPs modified with the SP88 peptide (H_2N-ELMNPLLPFIQP-COOH; identified to have an affinity for HCC in the same manner as SP94 (71)) are higher at all peptide densities than the K_d values of SP94-targeted VLPs since SP88 has a lower inherent affinity for Hep3B (489.2 ± 31.4 nM for SP88 versus 211.1 ± 12.2 nM for SP94).

Multivalent display of targeting peptides on the surfaces of MS2 VLPs promotes a high specific affinity for the cancer cell of interest but will likely initiate an antibody response against the peptide as well. Possible strategies for suppressing the humoral immune response against targeted VLPs include reducing the density of surface-displayed ligands or masking the capsid with PEG. Phage display enables identification of numerous different peptide sequences, all of which have a high affinity for the target cell. Multiple targeting peptides can, therefore, be conjugated to MS2 VLPs in order to decrease the valency of each peptide, which should mitigate the immunogenicity of the targeted VLP without reducing its overall avidity for the target cell. Fig. 2*C* demonstrates that MS2 VLPs modified with 30 copies each of SP94 and SP88 retain their sub-nanomolar affinity for Hep3B. Even when VLPs are modified with only three copies of

each peptide, their K_d for Hep3B remains sufficiently low (~ 20 nM) to enable selective targeting of HCC. PEGylation of MS2 VLPs should minimize proteolytic degradation of the capsid, reduce the humoral immune response against coat protein, and mitigate non-specific interactions with non-target cells, all of which will increase the circulation half-life and enhance bioavailability of encapsidated cargo (59). We have demonstrated that coupling methyl-$(PEG)_{24}$-amine (~1000 Da with a spacer arm 8.6-nm in length) to the MS2 capsid using EDC results in > 80% modification and reduces recognition of MS2 VLPs by anti-MS2 monoclonal antibodies (results not shown). Masking a nanoparticle's surface with PEG, however, typically reduces its specific affinity for the target cancer cell by interfering with ligand binding (82). We have tested the degree to which PEGylated MS2 VLPs, surface-modified with SP94 using an extended-length crosslinker ($SM(PEG)_{24}$), bind to Hep3B and hepatocytes and have found that PEG-1000 does not substantially affect ($p \sim 0.055$ for $n = 5$ using the unpaired t test) the specific affinity of targeted VLPs for HCC (Fig. S1*D*).

Upon binding, SP94-targeted VLPs are rapidly endocytosed ($t_{½}$ = 6 minutes) by HCC (Fig. 1*B*) but show minimal surface binding and absolutely no internalization by hepatocytes (Fig. 1*C*). We have confirmed that the SP94 peptide directs VLPs to lysosomes upon endocytosis (Fig. S3) and have, therefore, further modified the capsid with a histidine-rich fusogenic peptide (Fig. 1*A*; H5WYG, H_2N-GLFHAIAHFIHGGWHGLIHGWYG-COOH (20)) that, upon protonation (pK_a = 6.0), induces osmotic swelling and membrane destabilization of endosomes without affecting the integrity of the plasma membrane. MS2 VLPs that co-display the SP94 and H5WYG peptides become dispersed in the cytosol of HCC cells within 1-4 hours of endocytosis

(Fig. S4), which indicates that degradation of sensitive or macromolecular cargo in the lytic lysosomal environment can be avoided.

Delivery of a Chemotherapeutic Cocktail to HCC via SP94-Targeted VLPs Induces Selective Cytotoxicity of HCC. To demonstrate the utility of MS2 VLPs in targeted delivery of cytotoxic agents to cancer, we encapsidated the chemotherapeutic drug, doxorubicin (trade name, Adriamycin®) by conjugating it to the 3' end of the *pac* site. Doxorubicin (DOX) is broad-spectrum anthracycline antibiotic that was isolated from *Streptomyces peucetius* in the early 1960's and approved by the FDA for treating human cancers in 1974. DOX inhibits DNA and RNA synthesis equally by intercalating double-stranded DNA and binding to topoisomerase II; DOX can, additionally, interact with anionic phospholipids present in cellular membranes to disrupt their macromolecular architectures (83). Enzymatic reduction of doxorubicin generates highly reactive free radicals, which are the leading cause of dose-limiting cardiotoxicity and painful palmar-plantar erythrodysesthesia (i.e. hand- foot syndrome). PEGylated liposomal doxorubicin (trade name, Doxil®), which received FDA approval in 2005, becomes concentrated in solid tumors via the EPR effect and, therefore, mitigates many adverse side effects associated with monomeric doxorubicin; active targeting of nanoparticle-encapsulated doxorubicin should further reduce non-specific toxicity and enable dose optimization.

MS2 VLPs each encapsidate 103 ± 9 molecules of doxorubicin, and, upon modification of the capsid with SP94, drug-loaded VLPs can induce selective apoptosis of Hep3B at nanomolar concentrations. Hep3B naturally expresses moderate levels of P-glycoprotein (Pgp), an efflux pump that is typically upregulated by cells during

acquisition of a MDR phenotype, which results in reduced intracellular accumulation of certain drugs, including anthracyclines (84). The concentration of doxorubicin necessary to kill 90% of MDR Hep3B (LC_{90}) in a population containing 1 x 10^6 cells/mL is 285.6 ± 8.2 nM, a value that can be reduced via inhibition of Pgp using cyclosporin A (CsA) (84) or addition of cisplatin and 5-fluorouracil (5-FU), neither of which are substrates for Pgp (85, 86) (Fig. 3*A*). Targeted nanocarriers that are internalized via receptor-mediated endocytosis are typically able to circumvent Pgp efflux mechanisms and can, therefore, kill MDR cancer cells at lower drug concentrations. DOX delivered via SP94-targeted MS2 VLPs is capable of killing 90% of MDR Hep3B at a concentration that is more than 10-fold less that LC_{90} value of free DOX. More impressively, MS2 VLPs loaded with DOX (45 ± 3 per VLP), cisplatin (49 ± 5 per VLP), and 5-FU (234 ± 16 per VLP), a chemotherapeutic drug cocktail known to be particularly effective against HCC (86) can kill 90% of MDR Hep3B at concentrations < 1 nM (Fig. 3*A*) without substantially affecting the viability of hepatocytes (Fig. 3*B*). VLPs of Qβ, a 28.5-nm icosahedral bacteriophage that is more stable than MS2 due to extensive disulfide crosslinking of its capsid, have a similar cytotoxic effect on MDR Hep3B but mitigate long-term hepatocyte toxicity (Fig. 3*B*)

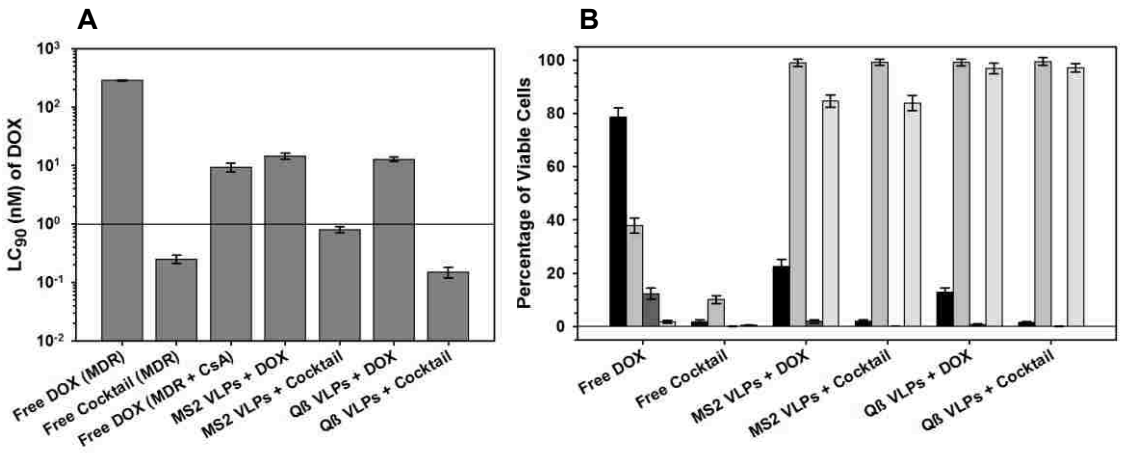

Figure 3. VLPs of MS2 and structurally related bacteriophages (e.g. Qβ) are capable of delivering a sufficient concentration of chemotherapeutic agents to induce cytotoxicity in Hep3B but not hepatocytes. (A) Doxorubicin (DOX) can be encapsulated within MS2 and Qβ VLPs via conjugation to the *pac* site, and a sufficiently high concentration can be delivered, via SP94-targeted VLPs, to DOX-resistant Hep3B to induce cytotoxicity at IC_{90} values of 10-15 nM, a 20-fold improvement in the cytotoxicity of free DOX. (B) The time-dependent viability of Hep3B (■ = 24 hours, ■ = 7 days) and hepatocytes (■ = 24 hours, ■ = 7 days) after exposure to free DOX, as well as DOX encapsulated in SP94-targeted VLPs. VLPs of Qβ bacteriophage are inherently more stable than MS2 VLPs due to the presence of disulfide bonds in their protein capsids; therefore DOX-loaded Qβ VLPs minimize the long-term loss of hepatocyte viability while effectively killing MDR Hep3B. All error bars represent 95% confidence intervals (1.96 σ) for n = 5.

SP94-Targeted MS2 VLPs that Encapsidate a Cocktail of siRNA Induce RNAi-Mediated Growth Arrest and Apoptosis of HCC. Due to their ability to spontaneously self-assemble in the presence of nucleic acids, MS2 VLPs are natural carriers of antisense oligonucleotides, small interfering RNA (siRNA), microRNA (miRNA), ribozymes, RNA decoys, aptamers, etc. and can potentially be adapted to encapsulate DNA vectors that encode therapeutic RNAs. RNA interference (RNAi) has been widely used to suppress expression of various proteins necessary for cancer cell proliferation and survivability via sequence-specific, post-transcriptional gene silencing that is typically mediated by siRNA or miRNA(87, 88). siRNAs (~21-base-pair segments of double-stranded RNA) are attractive as anti-cancer agents given their ability to promote RNAi in

mammalian cells without eliciting an interferon response (89). Furthermore, Davis, *et al.* recently demonstrated that siRNA, upon systemic administration via Tf-targeted polymeric nanoparticles can effectively inhibit specific genes in humans with solid tumors(3). Thus, targeted delivery of siRNA shows great promise in effectively treating a variety of cancers(90).

siRNA-driven formation of MS2 VLPs results in a > 90% yield of fully-assembled capsids, nearly 100% of which encapsidate 94 ± 6 siRNA molecules. siRNA-loaded MS2 VLPs are stable for > 3 months and effectively protect encapsidated siRNA from RNase-mediated degradation (data not shown). SP94-targeted MS2 VLPs that encapsidate a cocktail of siRNA that silences expression of cyclin A2, cyclin B1, cyclin D1, and cyclin E1 induce selective growth arrest and apoptosis of Hep3B at concentrations < 100 pM. The upregulation and activation of certain cyclins and cyclin-dependent kinases (Cdk), including cyclin A, cyclin D1, cyclin E, and Cdk4, have been implicated in hepatocarcinogenesis(91), and siRNA-mediated silencing of cyclin B1 and cyclin E has been demonstrated to enhance the susceptibility of various cancer types to chemotherapeutic drugs, as well as to induce selective growth arrest and apoptosis (92-94). SP94-targeted VLPs loaded with a siRNA that induces sequence-specific degradation of cyclin A2, cyclin B1, cyclin D1, or cyclin E1 mRNA cause a dose-dependent (Fig. 4*A*) and time-dependent (Fig. 4*B*) decrease in expression of the target protein upon exposure to Hep3B. The concentrations of siRNA necessary to silence 90% of cyclin A2, cyclin B1, cyclin D1, and cyclin E1 expression (IC_{90}) when delivered to Hep3B via SP94-targeted VLPs are 152 ± 4.3 pM, 164 ± 2.5 pM, 171 ± 3.9 pM, and 201 ± 7.8 pM, respectively (Fig. 4*A*), all of which correlate well to IC_{90} values obtained using

commercially-available transfection reagents (Fig. S5*A*). As compared to non-specific transfection reagents composed of cationic lipids (e.g. Lipofectamine^{TM} RNAiMAX), however, SP94-targeted VLPs are capable of selectively delivering siRNA cocktails to Hep3B without affection protein levels in hepatocytes (Fig. S5*B*). Exposure of Hep3B to the concentration of SP94-targeted VLPs necessary to reach the IC_{90} value for a particular target protein causes a 90% reduction in protein expression within 48 hours (Fig. 4*B*), an effect that persists for nearly a week and can be prolonged via modification of siRNA with a nuclear localization sequence (H_2N-NQSSNFGPMKGGNFGGRSSGPYGGGGQYFAKPRNQGGY-COOH, derived from the M9 domain of heterogeneous nuclear ribonucleoprotein A1(95)) (Fig. S5*C*). SP94-targeted MS2 VLPs that encapsidate the siRNA cocktail induce G_0/G_1 arrest (Fig. 4*C*) and apoptosis (Figs. 4*D* and S5*E*) in 90% of Hep3B within 72 hours at a total siRNA concentration of 100 pM without affecting the viability of hepatocytes (Figs. 4*D* and S5*F*).

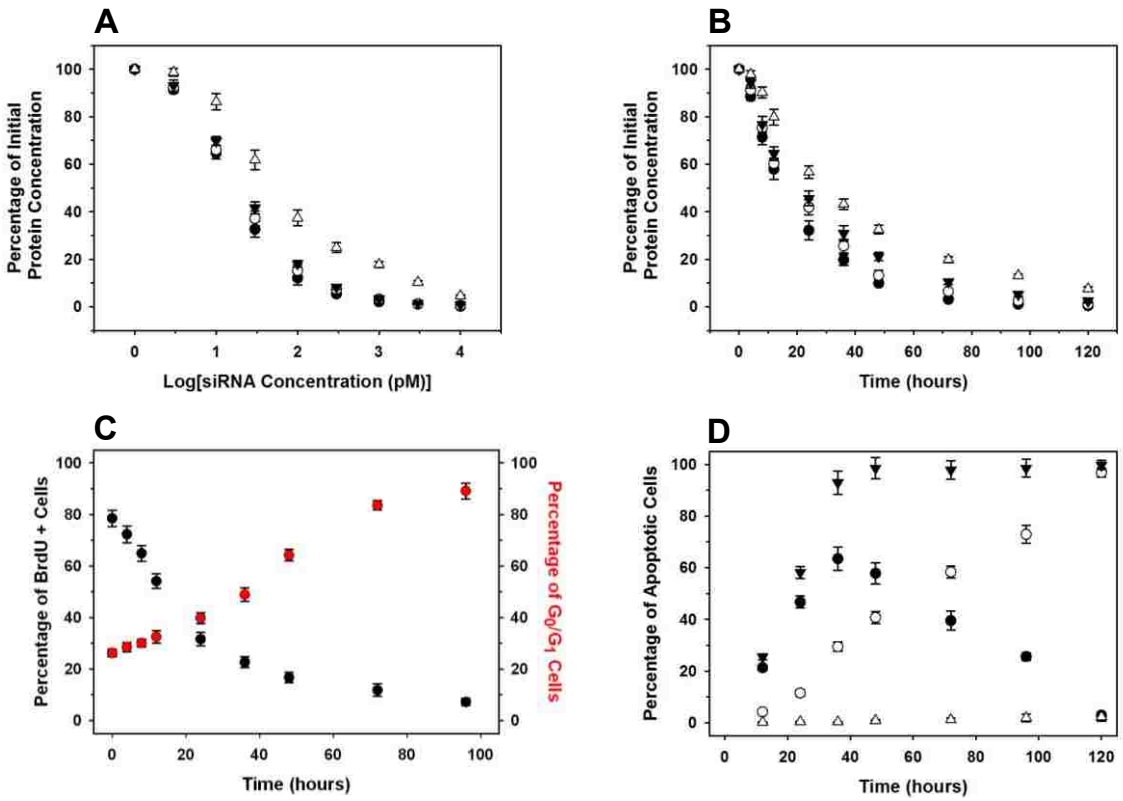

Figure 4. MS2 VLPs are natural carriers of small interfering RNA (siRNA) and modification of the capsid with the SP94 peptide enables specific delivery of siRNA cocktails that silence expression of various cyclins to Hep3B, causing rapid growth arrest and apoptosis at picomolar concentrations. (A) and (B) siRNAs that silence expression of cyclin A2 (●), cyclin B1 (○), cyclin D1 (▼), or cyclin E1 (Δ), when delivered to Hep3B via SP94-targeted VLPs, cause a dose- (A) and time-dependent (B) decrease in protein concentrations, as determined by immunofluorescence. (C) SP94-targeted VLPs that encapsidate a siRNA cocktail (silences expression of cyclin A2, cyclin D1, and cyclin E1; 100 pM total concentration) induce proliferation arrest, as determined by BrdU incorporation, and G_0/G_1 arrest, as determined by Hoechst 33342 staining, in Hep3B within 72 hours. (D) SP94-targeted VLPs that encapsidate a siRNA cocktail (silences expression of cyclin A2, cyclin B1, cyclin D1, and cyclin E1; 100 pM total concentration) induce apoptosis in Hep3B (▼ = total number of apoptotic cells) but not hepatocytes (Δ) within 48 hours. Early apoptosis (● = cells positive for Alexa Fluor® 488-labeled annexin V) is induced in Hep3B within 12 hours, and late apoptosis (○ = cells positive for annexin V and propidium iodide) is induced within 24-48 hours. All error bars represent 95% confidence intervals (1.96 σ) for n = 5.

Ricin A-Chain Can Induce Specific Intoxication of HCC at Femtomolar Concentrations when Delivered via SP94-Targeted VLPs. MS2 VLPs can stably encapsidate RNA-modified cargo within their interior volume, which protects cargo from

degradation and prevents toxicity to non-target cells and tissues. MS2 VLPs modified with high densities of targeting ligands can, furthermore, bind to and be internalized by cancer cells with high specificity. The combined stability and targeting efficacy of MS2 VLPs has enabled their development as a delivery vehicle for especially cytotoxic agents, such as the A-chain of ricin toxin (57). Ricin is a potent protein toxin derived from the seeds of *Ricinis communis* and exerts its cytotoxic effect via catalytic inhibition of protein synthesis. Native ricin is a heterodimer composed of the catalytically-active A-chain (32 kDa), which inhibits eukaryotic ribosomes via depurination of a single adenine residue (A^{4324}) in 28S RNA, and the galactose-binding B-chain (32 kDa), which utilizes its lectin activity to promote receptor-mediated endocytosis of the toxin (96, 97).

We have demonstrated that ricin A-chain, when encapsidated within SP94-targeted MS2 VLPs, induces caspase-3-dependent apoptosis of Hep3B at a concentration of 100 fM while maintaining nearly 100% hepatocyte viability. SP94-targeted VLPs loaded with ricin A-chain cause a dose-dependent (Fig. 5*A*) and time-dependent (Fig. 5*B*) decrease in nascent protein synthesis upon exposure to Hep3B. The concentration of ricin A-chain-loaded VLPs necessary to cause a 90% reduction in Hep3B protein biosynthesis within 48 hours is 98.9 ± 3.8 fM (Fig. 5*A*). The SP94 peptide, when displayed in high densities on MS2 VLPs, confers the specificity necessary to promote selective protein inhibition in HCC without affecting protein levels in hepatocytes (Fig. S6*A*). In comparison, monomeric ricin A-chain is unable to penetrate cells and, therefore, has no effect on Hep3B or hepatocyte protein synthesis, while ricin A-chain-loaded MS2 VLPs, when modified with a peptide (octaarginine, or R8 (98)) that promotes non-specific macropinocytosis, induce rapid protein inhibition when exposed to both Hep3B and

hepatocytes (Fig. S6*A*). In addition to inhibiting nascent protein synthesis, SP94-targeted MS2 VLPs that encapsidate ricin A-chain induce caspase-3-dependent apoptosis in Hep3B at exceedingly low concentrations (~100 fM) without affecting the viability of hepatocytes (Fig. 5*C*). Furthermore, apoptosis occurs rapidly; 90% of Hep3B cells are dead within 72 hours of being exposed to ricin A-chain-loaded VLPs (Fig. 5*D*). In order for SP94-targeted VLPs to effectively induce apoptosis in Hep3B, however, they must be co-modified with the H5WYG fusogenic peptide, which promotes endosomal escape of endocytosed VLPs and prevents lysosomal degradation of encapsidated ricin A-chain (Fig. S6*B*); agents that inhibit lysosome acidification, such as chloroquine, promote cytotoxicity of ricin A-chain-loaded VLPs in the absence of H5WYG. In conclusion, MS2 VLPs modified with a high density of the SP94 targeting peptide are able to selectively deliver a high payload of various therapeutic and diagnostic agents to HCC without affecting the viability of non-transformed cells. MS2 VLPs are ideally suited for targeted delivery of siRNA cocktails and possess the specificity and stability necessary to transport highly cytotoxic agents.

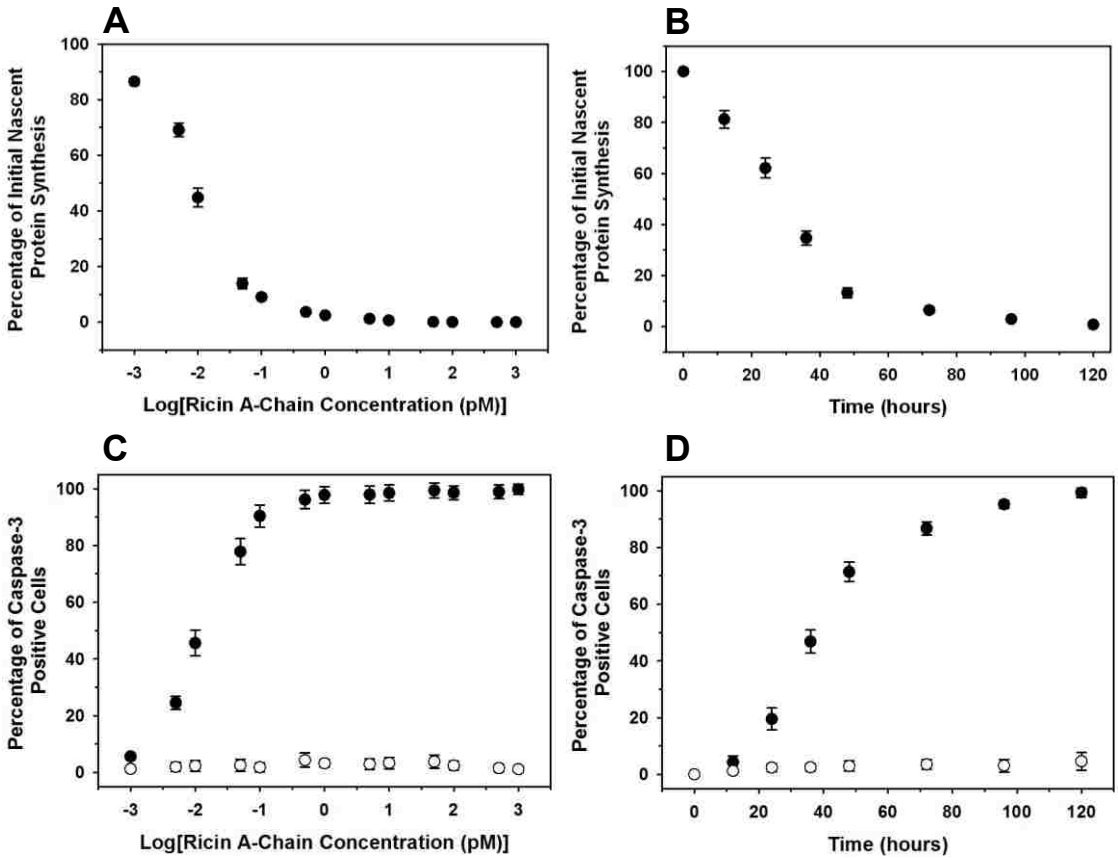

Figure 5. VLPs bearing the SP94 targeting peptide deliver ricin A-chain to HCC with high enough specificity to induce rapid apoptosis in Hep3B while leaving hepatocytes unharmed. (A) and (B) Ricin A-chain enzymatically inhibits 28S ribosomes and is, therefore, highly toxic to mammalian cells in minute quantities. Ricin A-chain cannot transverse the cell membrane unaided, however. SP94-modified VLPs encapsidate an average of 21 molecules of ricin A-chain per VLP and cause a 90% decrease in nascent protein synthesis (as measured by a decrease in the incorporation of a fluorescently-labeled derivative of methionine) at a concentration ~100 fM (A) within 48 hours (B). (C) Targeted VLPs that encapsidate ricin A-chain induce activation of caspase-3 in 90% of Hep3B cells at a concentration of 100 fM. (D) Ricin A-chain delivered to Hep3B via targeted VLPs induces activation of caspase-9 and caspase-3 within 12-24 hours. Hepatocytes remain unaffected, even after being exposed to ricin A-chain-loaded VLPs for >2 weeks. All error bars represent 95% confidence intervals (1.96 σ) for n = 5.

Materials and Methods

Synthesis of MS2 VLPs Loaded with Various Cargos

MS2 and Qβ bacteriophages were produced by infecting *E. coli* A/λ using well-established procedures(64) and purified by sedimentation to equilibrium in CsCl density gradients. To harvest coat protein for reassembly reactions, phages were diluted 1:3 in glacial acetic acid, incubated on ice for two hours, centrifuged briefly to pellet precipitated RNA and maturase, and dialyzed against 20 mM acetic acid for 20 hours. Modification of cargo with the *pac* site and/or fluorescent labels was performed as described in the Supplementary Materials and Methods section. Briefly, drug-*pac* site conjugates were made by adding an excess of doxorubicin and/or cisplatin to the *pac* site (containing either a 3' sulfhydryl moiety or modified with three internal 5-fluorouridines and a 5' thiol), pre-activated with LC-SPDP per manufacturer's instructions; unreacted drugs were removed via dialysis. To prepare quantum dot-*pac* site conjugates, amine-functionalized quantum dots were combined with an excess of LC-SPDP-activated *pac* site (modified with a 3' sulfhydryl moiety). Unreacted RNA was removed using a centrifugal filter device (50 kDa MWCO). Ricin A-chain-*pac* site conjugates were synthesized by activating reduced ricin A-chain with LC-SPDP, adding an excess of the *pac* site (containing a 3' amine moiety), incubating at 4°C for 24 hours, and removing unreacted RNA via centrifugal-driven filtration (10 kDa MWCO). A typical reassembly reaction consisted of 0.01 - 1 mM siRNA or *pac* site-modified cargo in 1X PBS, to which a 10-fold molar excess of dimerized coat protein was added. Reassembly was allowed to proceed for 4 hours at room temperature and 48 hours at 4°C prior to purification of excess coat protein and unencapsidated cargo via size-exclusion chromatography. VLPs

were modified with targeting ligands by incubating an excess of the ligand with $SM(PEG)_{24}$–activated capsids overnight at 4°C and removing unreacted ligand using a centrifugal filtration device (100 kDa MWCO). Average peptide density was determined using Tricine SDS-PAGE, while average Tf and CHALV-1 density was determined via Laemmli SDS-PAGE(99). ImageJ Image Processing and Analysis Software was utilized to compare band intensities relative to a standard concentration curve.

Determination of Dissociation Constants

Various concentrations of monovalent peptides (labeled with Alexa Fluor® 555 C_2 maleimide) or VLPs (labeled with Alexa Fluor® 555 carboxylic acid succinimidyl ester) were incubated with 1 x 10^6 cells/mL for 1 hour at 4°C. Unbound ligands and VLPs were removed via centrifugation, cells were resuspended in serum- and phenol red-free growth medium, and samples were analyzed with a FACSCalibur flow cytometer; fluorophores were excited with the 488-nm laser source, and emission was collected in the FL2 channel (585/42 filter/bandpass). Mean fluorescence intensity (MFI) was determined using FlowJo Software, and GraphPad Prism was employed to generate saturation binding curves (ligand or VLP concentration versus MFI), subtract the contribution of non-specific binding (i.e. binding of unmodified VLPs or VLPs modified with a control peptide) from total binding (i.e. binding of SP94-targeted VLPs), and calculate K_d values.

Preparation of Confocal Fluorescence Microscopy Samples

1 x 10^4 – 1 x 10^6 cells/mL were seeded on sterile coverslips (25-mm, No. 1.5) coated with 0.01% poly-L-lysine (150-300 kDa) and allowed to adhere for 4-24 hours at 37°C. Cells

were incubated with a 2000-fold excess of SP94-targeted VLPs for 1-4 hours at 37°C, washed with 1X PBS, stained according to manufacturer's instructions, fixed with 3.7% formaldehyde (10 minutes at room temperature), and mounted with an anti-fade reagent (SlowFade® Gold). Cells stained via immunofluorescence were, after fixation, permeabilized with 0.2% Triton X-100 (5 minutes at room temperature) and incubated with a blocking agent (Image-iT FX signal enhancer) for 30 minutes at room temperature; primary antibodies and secondary antibodies were diluted 1:500 in PBS with 1% BSA and incubated with cells for 1 hour at 37°C.

Viability and Apoptosis Assays

The viability of cells continually exposed for various time periods to various concentrations of chemotherapeutic drugs, drug cocktails, and siRNA cocktails was determined using either SYTOX® Green nucleic acid stain and Alexa Fluor® 647-labeled annexin V (drugs and drug cocktails) or Alexa Fluor® 488-labeled annexin V and propidium iodide (siRNA cocktails). Double-negative cells were considered to be viable; cells in early apoptosis were counted as those positive for annexin V, while cells in late apoptosis were counted as those double-positive for annexin V and either SYTOX ® Green or propidium iodide. Activation of caspase-3 and caspase-9 via SP94-targeted VLPs loaded with ricin A-chain was monitored using CaspGLOW™ staining kits per manufacturer's instructions.

References

1. Peer D*, et al.* (2007) Nanocarriers as an emerging platform for cancer therapy. (Translated from English) *Nature Nanotechnology* 2(12):751-760 (in English).
2. Park JH, Saravanakumar G, Kim K, & Kwon IC (Targeted delivery of low molecular drugs using chitosan and its derivatives. *Advanced Drug Delivery Reviews* 62(1):28-41.
3. Davis ME*, et al.* (Evidence of RNAi in humans from systemically administered siRNA via targeted nanoparticles. *Nature* advance online publication.
4. Sudimack J & Lee RJ (2000) Targeted drug delivery via the folate receptor. *Advanced Drug Delivery Reviews* 41(2):147-162.
5. Fawell S*, et al.* (1994) Tat-mediated delivery of heterologous proteins into cells. *Proceedings of the National Academy of Sciences of the United States of America* 91(2):664-668.
6. Halin C*, et al.* (2003) Synergistic Therapeutic Effects of a Tumor Targeting Antibody Fragment, Fused to Interleukin 12 and to Tumor Necrosis Factor {alpha}. *Cancer Res* 63(12):3202-3210.
7. Hirsch LR*, et al.* (2003) Nanoshell-mediated near-infrared thermal therapy of tumors under magnetic resonance guidance. *Proceedings of the National Academy of Sciences of the United States of America* 100(23):13549-13554.
8. Michalet X*, et al.* (2005) Quantum Dots for Live Cells, in Vivo Imaging, and Diagnostics. *Science* 307(5709):538-544.
9. Parkhurst QA, Connolly J, Jones SK, & Dobson J (2003) Applications of magnetic nanoparticles in biomedicine. *Journal of Physics D: Applied Physics* 36(13):R167-R181.
10. Oyewumi MO & Mumper RJ (2002) Engineering Tumor-Targeted Gadolinium Hexanedione Nanoparticles for Potential Application in Neutron Capture Therapy. *Bioconjugate Chemistry* 13(6):1328-1335.
11. Moolten FL & Cooperband SR (1970) Selective Destruction of Target Cells by Diphtheria Toxin Conjugated to Antibody Directed against Antigens on the Cells. *Science* 169(3940):68-70.
12. Cho K, Wang X, Nie S, Chen Z, & Shin DM (2008) Therapeutic Nanoparticles for Drug Delivery in Cancer. *Clinical Cancer Research* 14(5):1310-1316.
13. Jain RK (1994) Barriers to drug-delivery in solid tumors. *Scientific American* 271:58-65.
14. Xia T*, et al.* (2009) Polyethyleneimine Coating Enhances the Cellular Uptake of Mesoporous Silica Nanoparticles and Allows Safe Delivery of siRNA and DNA Constructs. *ACS Nano* 3(10):3273-3286.
15. Pastan I, Hassan R, FitzGerald DJ, & Kreitman RJ (2006) Immunotoxin therapy of cancer. *Nat Rev Cancer* 6(7):559-565.
16. Petrenko VA (2008) Evolution of phage display: from bioactive peptides to bioselective nanomaterials *Expert Opinion on Drug Delivery* 5(8):825-836.
17. Nilsson F, Tarli L, Viti F, & Neri D (2000) The use of phage display for the development of tumour targeting agents. *Advanced Drug Delivery Reviews* 43(2-3):165-196.

18. Jiang W, KimBetty YS, Rutka JT, & ChanWarren CW (2008) Nanoparticle-mediated cellular response is size-dependent. *Nat Nano* 3(3):145-150.
19. Ishida T, Kirchmeier MJ, Moase EH, Zalipsky S, & Allen TM (2001) Targeted delivery and triggered release of liposomal doxorubicin enhances cytotoxicity against human B lymphoma cells. *Biochimica et Biophysica Acta (BBA) - Biomembranes* 1515(2):144-158.
20. Midoux P, Kichler A, Boutin V, Maurizot J-C, & Monsigny M (1998) Membrane Permeabilization and Efficient Gene Transfer by a Peptide Containing Several Histidines. *Bioconjugate Chemistry* 9(2):260-267.
21. Kim Y, Klutz AM, & Jacobson KA (2008) Systematic Investigation of Polyamidoamine Dendrimers Surface-Modified with Poly(ethylene glycol) for Drug Delivery Applications: Synthesis, Characterization, and Evaluation of Cytotoxicity. *Bioconjugate Chemistry* 19(8):1660-1672.
22. Papahadjopoulos D*, et al.* (1991) STERICALLY STABILIZED LIPOSOMES - IMPROVEMENTS IN PHARMACOKINETICS AND ANTITUMOR THERAPEUTIC EFFICACY. (Translated from English) *Proceedings of the National Academy of Sciences of the United States of America* 88(24):11460-11464 (in English).
23. Lee JE*, et al.* (2009) Uniform Mesoporous Dye-Doped Silica Nanoparticles Decorated with Multiple Magnetite Nanocrystals for Simultaneous Enhanced Magnetic Resonance Imaging, Fluorescence Imaging, and Drug Delivery. *Journal of the American Chemical Society* 132(2):552-557.
24. Schneider GgF, Subr V, Ulbrich K, & Decher G (2009) Multifunctional Cytotoxic Stealth Nanoparticles. A Model Approach with Potential for Cancer Therapy. *Nano Letters* 9(2):636-642.
25. Liu JW, Jiang XM, Ashley C, & Brinker CJ (2009) Electrostatically Mediated Liposome Fusion and Lipid Exchange with a Nanoparticle-Supported Bilayer for Control of Surface Charge, Drug Containment, and Delivery. *Journal of the American Chemical Society* 131(22):7567-+.
26. Liu JW, Stace-Naughton A, & Brinker CJ (2009) Silica nanoparticle supported lipid bilayers for gene delivery. *Chemical Communications* (34):5100-5102.
27. Liu JW, Stace-Naughton A, Jiang XM, & Brinker CJ (2009) Porous Nanoparticle Supported Lipid Bilayers (Protocells) as Delivery Vehicles. *Journal of the American Chemical Society* 131(4):1354-+.
28. Douglas T*, et al.* (2002) Protein Engineering of a Viral Cage for Constrained Nanomaterials Synthesis. *Advanced Materials* 14(6):415-418.
29. Mao C*, et al.* (2003) Viral assembly of oriented quantum dot nanowires. *Proceedings of the National Academy of Sciences of the United States of America* 100(12):6946-6951.
30. Nam KT*, et al.* (2006) Virus-Enabled Synthesis and Assembly of Nanowires for Lithium Ion Battery Electrodes. *Science*:1122716.
31. Hunter Z, Smyth HD, Durfee P, & Chackerian B (2009) Induction of mucosal and systemic antibody responses against the HIV coreceptor CCR5 upon intramuscular immunization and aerosol delivery of a virus-like particle based vaccine. *Vaccine* 28(2):403-414.

32. Wheeler CM, *et al.* (2008) Safety and immunogenicity of co-administered quadrivalent human papillomavirus (HPV)-6/11/16/18 L1 virus-like particle (VLP) and hepatitis B (HBV) vaccines. *Vaccine* 26(5):686-696.
33. Peabody DS, *et al.* (2008) Immunogenic display of diverse peptides on virus-like particles of RNA phage MS2. *Journal of Molecular Biology* 380(1):252-263.
34. Bar H, Yacoby I, & Benhar I (2008) Killing cancer cells by targeted drug-carrying phage nanomedicines. *BMC Biotechnology* 8:37.
35. Yacoby I, Bar H, & Benhar I (2007) Targeted Drug-Carrying Bacteriophages as Antibacterial Nanomedicines. *Antimicrob. Agents Chemother.* 51(6):2156-2163.
36. Krumpe L & Mori T (2006) The Use of Phage-Displayed Peptide Libraries to Develop Tumor-Targeting Drugs. *International Journal of Peptide Research and Therapeutics* 12(1):79-91.
37. Sergeeva A, Kolonin MG, Molldrem JJ, Pasqualini R, & Arap W (2006) Display technologies: Application for the discovery of drug and gene delivery agents. *Advanced Drug Delivery Reviews* 58(15):1622-1654.
38. Aina OH, Sroka TC, Chen M-L, & Lam KS (2002) Therapeutic cancer targeting peptides. *Peptide Science* 66(3):184-199.
39. Chang D-K, *et al.* (2009) Antiangiogenic Targeting Liposomes Increase Therapeutic Efficacy for Solid Tumors. *Journal of Biological Chemistry* 284(19):12905-12916.
40. Arap W, Pasqualini R, & Ruoslahti E (1998) Cancer Treatment by Targeted Drug Delivery to Tumor Vasculature in a Mouse Model. *Science* 279(5349):377-380.
41. Chen L, *et al.* (2004) Design and Validation of a Bifunctional Ligand Display System for Receptor Targeting. *Chemistry & Biology* 11(8):1081-1091.
42. Hart SL, *et al.* (1994) Cell binding and internalization by filamentous phage displaying a cyclic Arg-Gly-Asp-containing peptide. *Journal of Biological Chemistry* 269(17):12468-12474.
43. Aniagyei SE, DuFort C, Kao CC, & Dragnea B (2008) Self-assembly approaches to nanomaterial encapsulation in viral protein cages. *Journal of Materials Chemistry* 18(32):3763-3774.
44. Jayanna P, Torchilin V, & Petrenko V (2009) Liposomes targeted by fusion phage proteins. *Nanomedicine: Nanotechnology, Biology and Medicine* 5(1):83-89.
45. Ngweniform P, Abbineni G, Cao B, & Mao C (2009) Self-Assembly of Drug-Loaded Liposomes on Genetically Engineered Target-Recognizing M13 Phage: A Novel Nanocarrier for Targeted Drug Delivery. *Small* 5(17):1963-1969.
46. Curiel DT (1999) Strategies to adapt adenoviral vectors for targeted delivery. *ANTICANCER MOLECULES: STRUCTURE, FUNCTION, AND DESIGN* (ANNALS OF THE NEW YORK ACADEMY OF SCIENCES), Vol 886, pp 158-171.
47. Bachtarzi H, Stevenson M, & Fisher K (2008) Cancer Gene Therapy with Targeted Adenoviruses. *Expert Opinion on Drug Delivery* 5(11):1231-1240.
48. Gleiter S & Lilie H (2003) Cell-type specific targeting and gene expression using a variant of polyoma VP1 virus-like particles <http://apps.isiknowledge.com.libproxy.unm.edu/full_record.do?product=WOS&search_mode=GeneralSearch&qid=26&SID=2AD3cClDglAeJEB6iIK&page=1&doc=1> *Biological Chemistry* 384(2):247-255.

49. May T, Gleiter S, & Lilie H (2002) Assessment of cell type specific gene transfer of polyoma virus like particles presenting a tumor specific antibody Fv fragment. *Journal of Virological Methods* 105(1):147-157.
50. Lankes HA*, et al.* (2007) In vivo gene delivery and expression by bacteriophage lambda vectors. *Journal of Applied Microbiology* 102(5):1337-1349.
51. Li L*, et al.* (2009) Evaluation of specific delivery of chimeric phi29 pRNA/siRNA nanoparticles to multiple tumor cells. *Molecular Biosystems* 5(11):1361-1368.
52. Singh P, Destito G, Schneemann A, & Manchester M (2006) Canine parvovirus-like particles, a novel nanomaterial for tumor targeting. *Journal of Nanobiotechnology* 4(1):2.
53. Douglas T & Young M (1998) Host-guest encapsulation of materials by assembled virus protein cages. *Nature* 393(6681):152-155.
54. Desito G, Yeh R, Rae CS, Finn MG, & Manchester M (2007) Folic Acid-Mediated Targeting of Cowpea Mosaic Virus Particles to Tumor Cells. *Chemistry & Biology* 14(10):1152-1162.
55. Brunel FM*, et al.* (Hydrazone Ligation Strategy to Assemble Multifunctional Viral Nanoparticles for Cell Imaging and Tumor Targeting. *Nano Letters* 10(3):1093-1097.
56. Ren Y, Wong SM, & Lim L-Y (2007) Folic Acid-Conjugated Protein Cages of a Plant Virus:â€‰ A Novel Delivery Platform for Doxorubicin. *Bioconjugate Chemistry* 18(3):836-843.
57. Wu M, Brown WL, & Stockley PG (1995) Cell-Specific Delivery of Bacteriophage-Encapsidated Ricin A Chain. *Bioconjugate Chemistry* 6(5):587-595.
58. Wu M, Sherwin T, Brown WL, & Stockley PG (2005) Delivery of antisense oligonucleotides to leukemia cells by RNA bacteriophage capsids. *Nanomedicine: Nanotechnology, Biology and Medicine* 1(1):67-76.
59. Kovacs EW*, et al.* (2007) Dual-Surface-Modified Bacteriophage MS2 as an Ideal Scaffold for a Viral Capsid-Based Drug Delivery System. *Bioconjugate Chemistry* 18(4):1140-1147.
60. Wu W, Hsiao Sonny C, Carrico Zachary M, & Francis Matthew B (2009) Genome-Free Viral Capsids as Multivalent Carriers for Taxol Delivery13. *Angewandte Chemie* 121(50):9657-9661.
61. Hooker JM, Datta A, Botta M, Raymond KN, & Francis MB (2007) Magnetic Resonance Contrast Agents from Viral Capsid Shells:â€‰ A Comparison of Exterior and Interior Cargo Strategies. *Nano Letters* 7(8):2207-2210.
62. Carrico ZM, Romanini DW, Mehl RA, & Francis MB (2008) **Oxidative coupling of peptides to a virus capsid containing unnatural amino acids**. *Chemical Communications*:1207-1207.
63. Tong GJ, Hsiao SC, Carrico ZM, & Francis MB (2009) Viral Capsid DNA Aptamer Conjugates as Multivalent Cell-Targeting Vehicles. *Journal of the American Chemical Society* 131(31):11174-11178.
64. Hooker JM, Kovacs EW, & Francis MB (2004) Interior Surface Modification of Bacteriophage MS2. *Journal of the American Chemical Society* 126(12):3718-3719.

65. Pickett GG & Peabody DS (1993) Encapsidation of heterologous RNAs by bacteriophage MS2 coat protein. *Nucl. Acids Res.* 21(19):4621-4626.
66. Rohrmann GF & Krueger RG (1970) The self-assembly of RNA free protein subunits from bacteriophage MS-2. *Biochemical and Biophysical Research Communications* 38(3):406-413.
67. Bundy B, Franciszkowicz M, & Swartz J (2007) **Escherichia coli-based Cell-free Synthesis of Virus-like Particles**. *Biotechnology and Bioengineering* 100:28-37.
68. Uhlenbeck O (1998) A coat for all sequences. *Nature Sturctural Biology* 5(3):174-176.
69. Weissleder R, Kelly K, Sun EY, Shtatland T, & Josephson L (2005) Cell-specific targeting of nanoparticles by multivalent attachment of small molecules. *Nat Biotech* 23(11):1418-1423.
70. Vance D, Martin J, Patke S, & Kane RS (2009) The design of polyvalent scaffolds for targeted delivery. *Advanced Drug Delivery Reviews* 61(11):931-939.
71. Lo A, Lin CT, & Wu HC (2008) Hepatocellular carcinoma cell-specific peptide ligand for targeted drug delivery. *Molecular Cancer Therapeutics* 7(3):579-589.
72. Li Z*, et al.* (2005) Identification and characterization of a novel peptide ligand of epidermal growth factor receptor for targeted delivery of therapeutics. *FASEB J.* 19(14):1978-1985.
73. Lu X, Weiss P, & Block T (2004) A phage with high affinity for hepatitis B surface antigen for the detection of HBsAg. *Journal of Virological Methods* 119(1):51-54.
74. Kannangai R, Sahin F, & Torbenson MS (2006) EGFR is phosphorylated at Ty845 in hepatocellular carcinoma. *Mod Pathol* 19(11):1456-1461.
75. Chemin I & Zoulim F (2009) Hepatitis B virus induced hepatocellular carcinoma. *Cancer Letters* 286(1):52-59.
76. SCIOT R*, et al.* (1988) Transferrin receptor expression in human hepatocellular carcinoma: an immunohistochemical study of 34 cases. *Histopathology* 12(1):53-63.
77. Gilligan A, Bushmeyer S, & Knowles BB (1992) Variation in EGF-induced EGF receptor downregulation in human hepatoma-derived cell lines expressing different amounts of EGF receptor. *Experimental Cell Research* 200(2):235-241.
78. Baynes R*, et al.* (1988) Transferrin iron interactions with cultured hepatocellular carcinoma cells (PLC/PRF/5). *European Journal of Cell Biology* 46(2):282-288.
79. Benoit M, Gabriel D, Gerisch G, & Gaub HE (2000) Discrete interactions in cell adhesion measured by single-molecule force spectroscopy. *Nat Cell Biol* 2(6):313-317.
80. Chu JJH, Lee JWM, & Ng ML (2005) Bio-Imaging the Entry Process of an Emerging Pathogenic Virus: The West Nile Virus. *Microscopy and Microanalysis* 11:958-959.
81. Gilbert Y*, et al.* (2007) Single-Molecule Force Spectroscopy and Imaging of the Vancomycin/d-Ala-d-Ala Interaction. *Nano Letters* 7(3):796-801.
82. Ferrari M (2008) Nanogeometry: Beyond drug delivery. *Nat Nano* 3(3):131-132.

83. Severs NJ, Twist VW, & Powell T (1991) Acute effects of adriamycin on the macromolecular organization of the cardiac-muscle cell plasma membrane. *Cardioscience* 2(1):35-45.
84. Tong AW*, et al.* (1996) Chemosensitization of human hepatocellular carcinoma cells with cyclosporin A in post-liver transplant patient plasma. *Clinical Cancer Research* 2(3):531-539.
85. Shen X, Chen G, Zhu G, & Fong W-F (2006) (±)-3'-O, 4'-O-dicynnamoyl-cis-khellactone, a derivative of (±)-praeruptorin A, reverses P-glycoprotein mediated multidrug resistance in cancer cells. *Bioorganic & Medicinal Chemistry* 14(21):7138-7145.
86. Lee JO*, et al.* (2009) Combination chemotherapy with capecitabine and cisplatin for patients with metastatic hepatocellular carcinoma. *Annals of Oncology* 20(8):1402-1407.
87. Ashihara E, Kawata E, & Maekawa T (2010) Future Prospect of RNA Interference for Cancer Therapies. *Current Drug Targets* 11(3):345-360.
88. Pawitan JA (2009) The possible use of RNA interference in diagnosis and treatment of various diseases. *International Journal of Clinical Practice* 63(9):1378-1385.
89. Elbashir SM*, et al.* (2001) Duplexes of 21-nucleotide RNAs mediate RNA interference in cultured mammalian cells. *Nature* 411(6836):494-498.
90. Oh Y-K & Park TG (2009) siRNA delivery systems for cancer treatment. *Advanced Drug Delivery Reviews* 61(10):850-862.
91. Masaki T*, et al.* (2003) Cyclins and cyclin-dependent kinases: Comparative study of hepatocellular carcinoma versus cirrhosis. *Hepatology* 37(3):534-543.
92. Gurzov EN & Izquierdo M (2006) Cyclin E1 knockdown induces apoptosis in cancer cells. *Neurological Research* 28:493-499.
93. Yuan J*, et al.* (2005) Stable gene silencing of cyclin B1 in tumor cells increases susceptibility to taxol and leads to growth arrest in vivo. *Oncogene* 25(12):1753-1762.
94. Li K, Lin S-Y, Brunicardi FC, & Seu P (2003) Use of RNA Interference to Target Cyclin E-overexpressing Hepatocellular Carcinoma. *Cancer Res* 63(13):3593-3597.
95. Subramanian A, Ranganathan P, & Diamond SL (1999) Nuclear targeting peptide scaffolds for lipofection of nondividing mammalian cells. *Nat Biotech* 17(9):873-877.
96. Franz D.V.M. MD, David R. & Jaax D.V.M. NK (1997) Ricin Toxin. *Medical Aspects of Chemical and Biological Warfare* eds Sidell F, R., Takafuji ET, & Franz DR (Borden Institute, Walter Reed Army Medical Center, Washington, D.C.), pp 631-642.
97. Wu Y-H, Shih S-F, & Lin J-Y (2004) Ricin Triggers Apoptotic Morphological Changes through Caspase-3 Cleavage of BAT3. *Journal of Biological Chemistry* 279(18):19264-19275.
98. Khalil IA, Kogure K, Futaki S, & Harashima H (2006) High Density of Octaarginine Stimulates Macropinocytosis Leading to Efficient Intracellular Trafficking for Gene Expression. *Journal of Biological Chemistry* 281(6):3544-3551.

99. Schagger H (2006) Tricine-SDS-PAGE. *Nat. Protocols* 1(1):16-22.

Supplementary Figures and Legends:

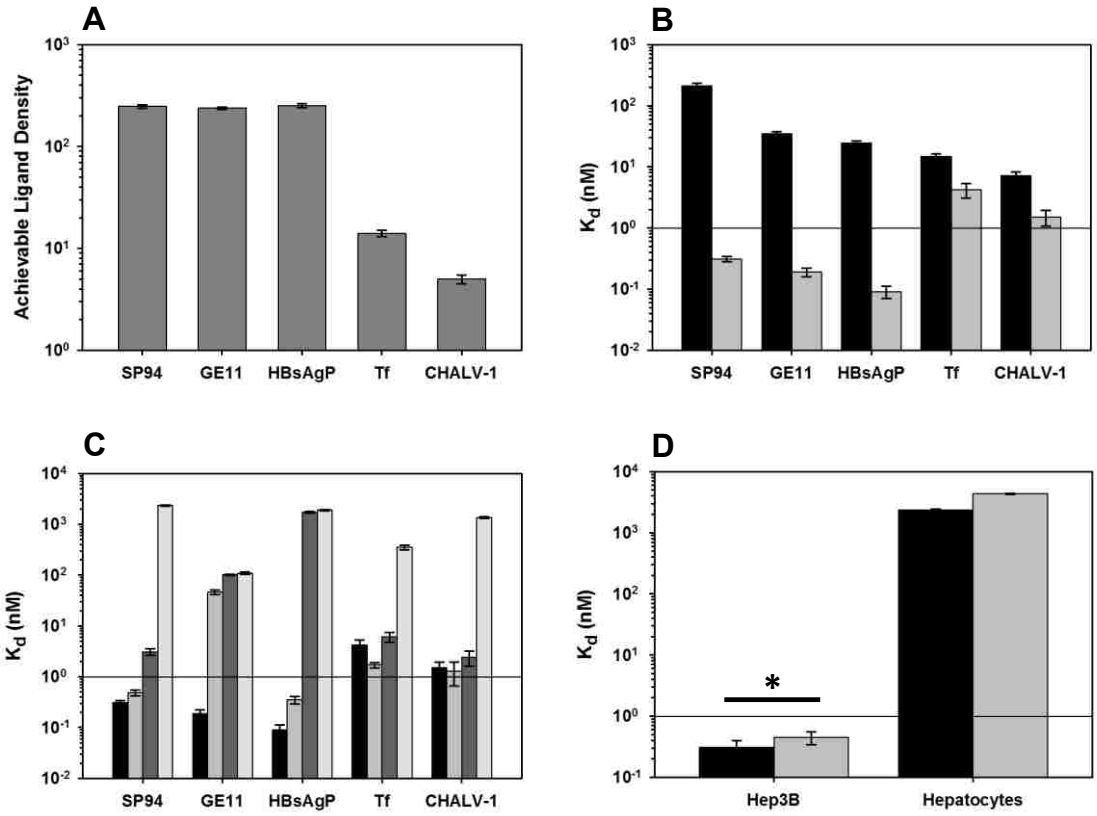

Figure S1. The avidity of MS2 VLPs for HCC is dependent on the inherent affinity of the monovalent ligand, as well as on the density of ligands displayed on the VLP surface. (A) The average number of ligands that can be conjugated to a single MS2 VLP under saturating conditions. (B) The dissociation constants (K_d) of monovalent ligands (■) and MS2 VLPs modified with the maximum ligand density (■) when exposed to Hep3B. (C) K_d values of MS2 VLPs, when modified with the maximum ligand density, for Hep3B (■), PLC/PRF/5 (■), HepG2 (■), and hepatocytes (■). (D) The K_d values of SP94-targeted MS2 VLPs (modified with an average of 240 peptides per VLP) for Hep3B and hepatocytes when VLPs are either unmodified (■) or surface-modified with PEG (■). * indicates that the values are NOT significantly different (using ANOVA, $p \sim 0.50$ for $n = 5$). All error bars represent 95% confidence intervals (1.96 σ) for $n = 5$.

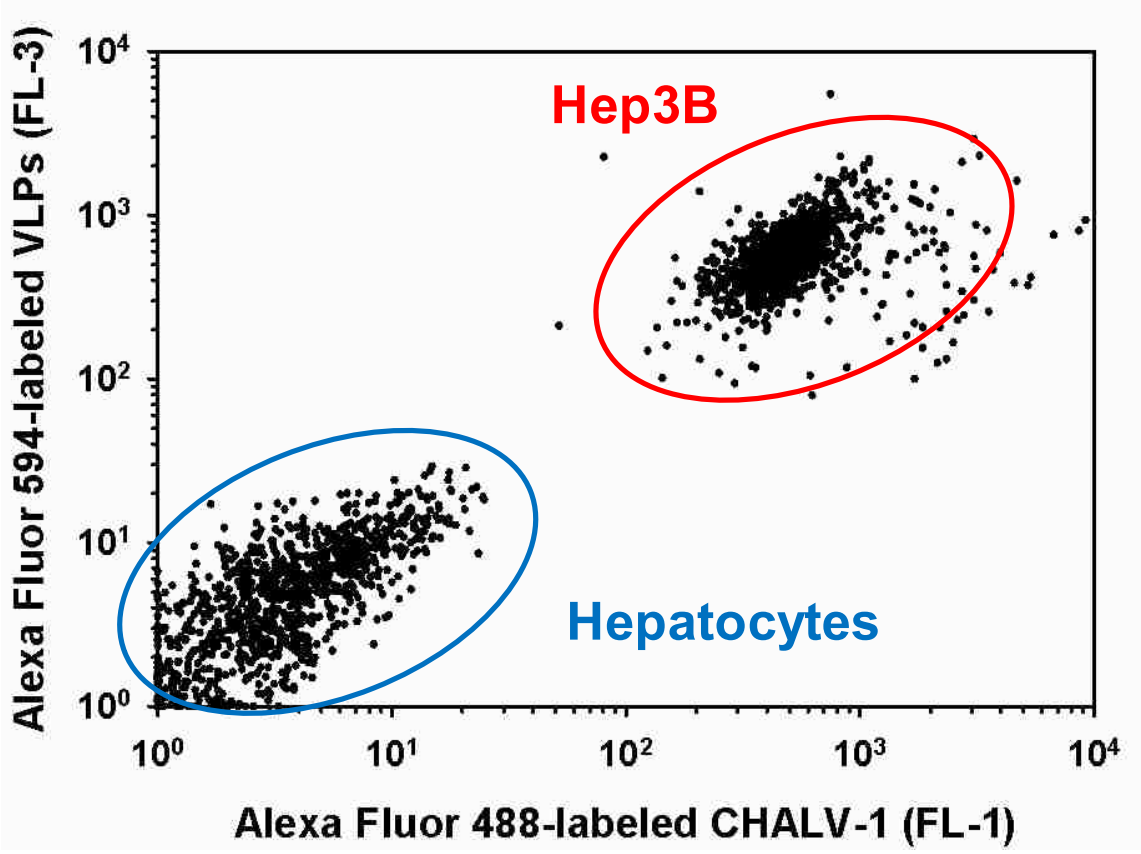

Figure S-2. MS2 VLPs modified with a high density (~240 peptides per VLP) of the SP94 targeting peptide can bind specifically to Hep3B cells even when they are co-cultured with hepatocytes. Alexa Fluor® 488-labeled CHALV-1 specifically recognizes and binds to HCC.

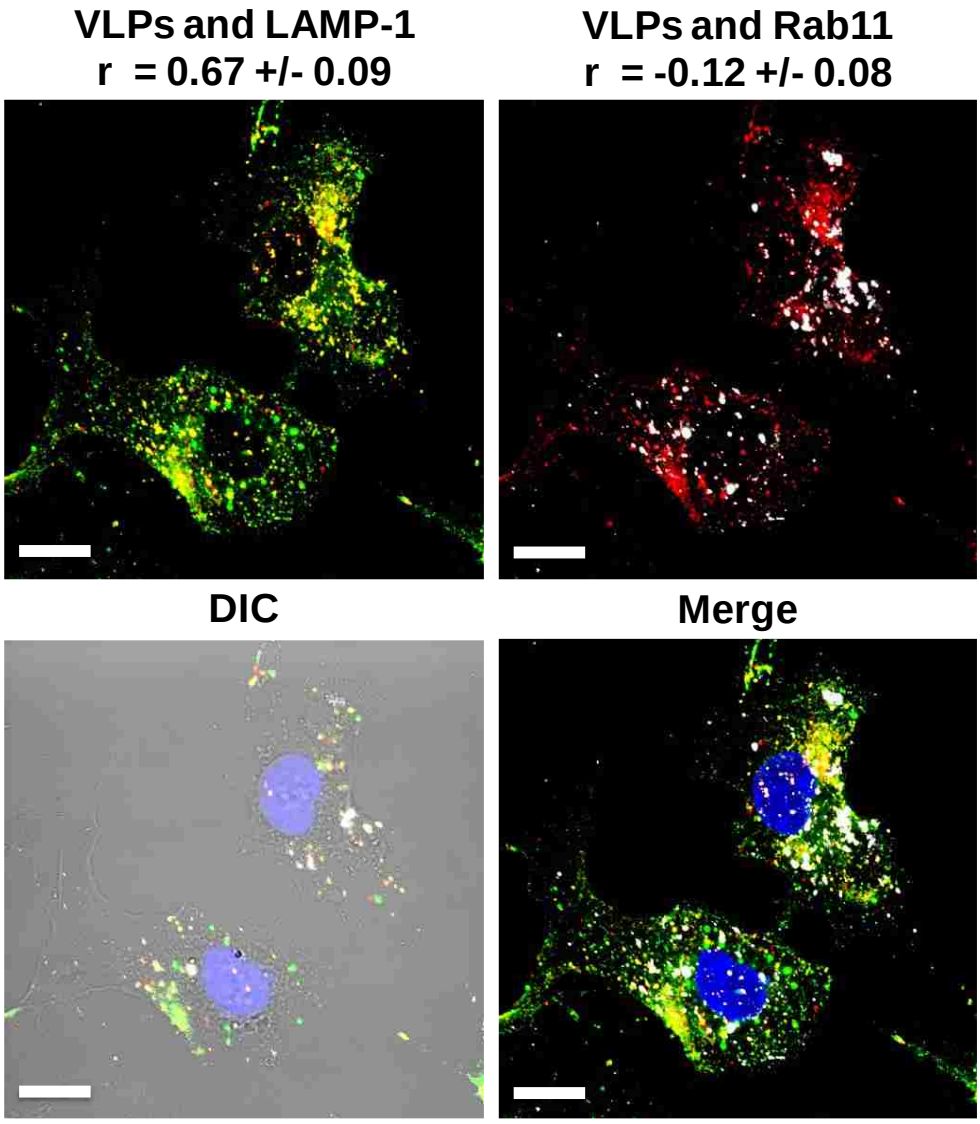

Figure S-3. MS2 VLPs modified with the SP94 targeting peptide are directed to lysosomes upon endocytosis by HCC. A saturating concentration of SP94-targeted VLPs, labeled with Alexa Fluor® 555 (red), was exposed to sub-confluent Hep3B cells for 2 hours at 37°C. The cells were then washed, fixed, permeabilized, and exposed to an Alexa Fluor® 488-labeled antibody against lysosome-associated membrane protein-1 (LAMP-1, green) and an Alexa Fluor® 647-labeled antibody against Rab11a (white). The positive Pearson's correlation (r) that exists between SP94-targeted VLPs and LAMP-1 indicates that VLPs are directed to lysosomes upon endocytosis by Hep3B. Conversely, the near-zero Pearson's correlation that exists between SP94-targeted VLPs and Rab11 indicates that VLPs are not localized within $Rab11^+$ recycling endosomes. Differential Interference Contrast (DIC) images were employed to define the boundaries of Hep3B cells, the nuclei of which are labeled with DAPI, such that pixels outside of the cell boundaries could be disregarded when calculating Pearson's correlation coefficients (expressed as the mean value ± the standard deviation for n = 3 x 50 cells). Scale bars = 10 μm.

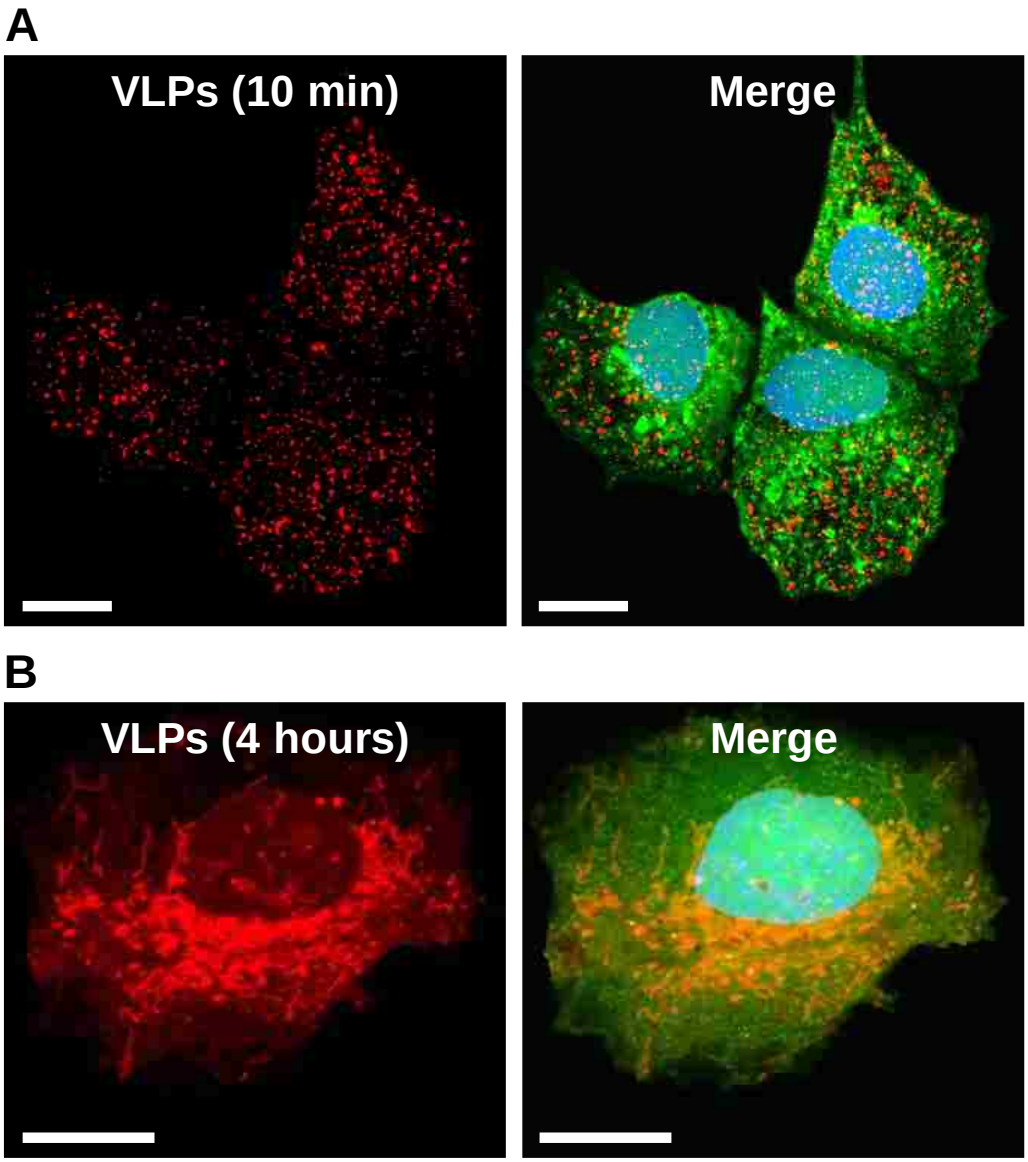

Figure S-4. Upon endocytosis, MS2 VLPs co-modified with the SP94 targeting peptide and the H5WYG fusogenic peptide become distributed in the cytosol of HCC cells. (A) SP94-targeted MS2 VLPs, labeled with Alexa Fluor® 555 (red), are rapidly endocytosed by Hep3B ($t_{½}$ = 6 minutes). (B) VLPs co-modified with the SP94 and H5WYG peptides become distributed in the cytosol of Hep3B cells within 1-4 hours of endocytosis. Hep3B cells are labeled with Hoechst 33342 and CellTracker™ Green CMDFA. Scale bars = 10 μm.

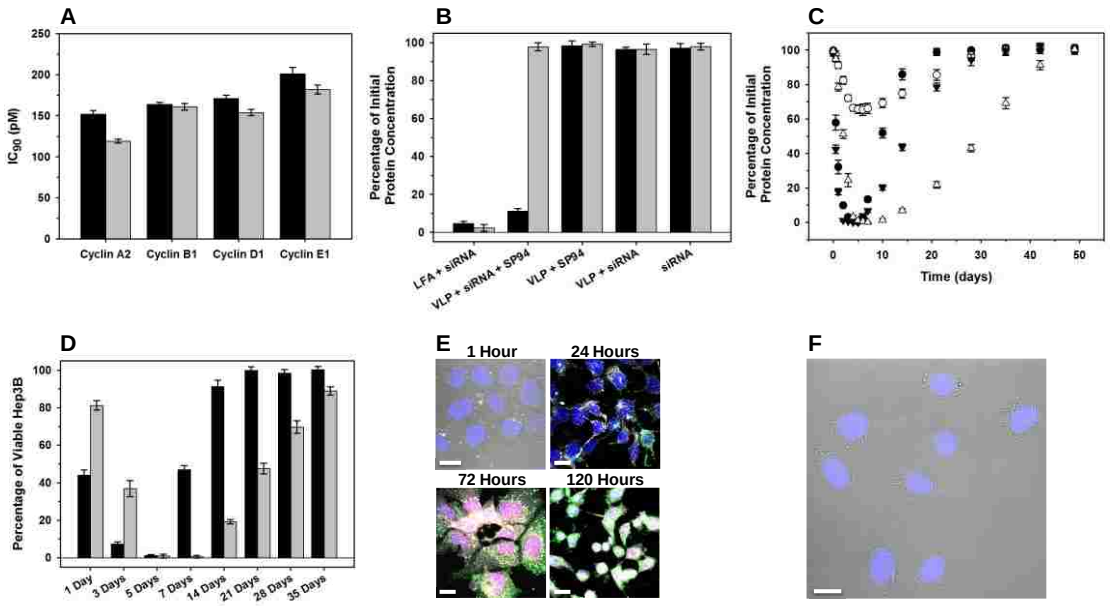

Figure S-5. SP94-targeted MS2 VLPs, when loaded with a siRNA cocktail that silences expression of cyclin A2, cyclin B1, cyclin D1, and/or cyclin E1, can induce selective apoptosis of Hep3B without affecting the viability of hepatocytes. (A) The concentration of siRNA necessary to silence 90% of cyclin A2, cyclin B1, cyclin D1, or cyclin E1 expression (IC_{90}) in Hep3B when delivered via SP94-targeted MS2 VLPs (■) or Lipofectamine™ RNAiMAX (■). (B) The percentage of initial cyclin A2 expression that remains upon exposure of Hep3B (■) and hepatocytes (■) to Lipofectamine™ RNAiMAX (LFA) with encapsulated siRNA or SP94-targeted VLPs with encapsulated siRNA. Cyclin A2 expression is unaffected by SP94-targeted VLPs, unmodified VLPs with encapsulated siRNA, and siRNA alone. (C) The time-dependent change in cyclin A2 expression after exposure of logarithmic (●) or confluent Hep3B (○) to SP94-targeted, siRNA-loaded VLPs for 24 hours. The duration of cyclin A2 silencing can be increased via modification of the siRNA with a nuclear localization sequence (NLS); cyclin A2 concentrations remain at less than 50% of initial values for 14 days in logarithmic Hep3B (▼) and for 28 days in confluent Hep3B (Δ) using this strategy. (D) NLS-modified siRNA (■) can, when delivered to logarithmic Hep3B via SP94-targeted MS2 VLPs, suppress Hep3B division for longer periods of time than unmodified siRNA (■). (E) and (F) SP94-targeted VLPs, when loaded with the siRNA cocktail, can induce apoptosis of Hep3B (E) without affecting the viability of hepatocytes (F). Within several minutes, MS2 VLPs, labeled with Alexa Fluor® 647 (white), are endocytosed by Hep3B. Within several hours, VLPs become distributed in the cytosol of Hep3B cells and release their encapsidated siRNA. Early apoptosis (determined using Alexa Fluor® 488-labeled annexin V) is induced within 24 hours, while late apoptosis (determined using propidium iodide) is induced within 72 hours. The nuclei of Hep3B and hepatocytes are labeled with DAPI. All scale bars = 20 μm. All error bars represent 95% confidence intervals (1.96 σ) for n = 3.

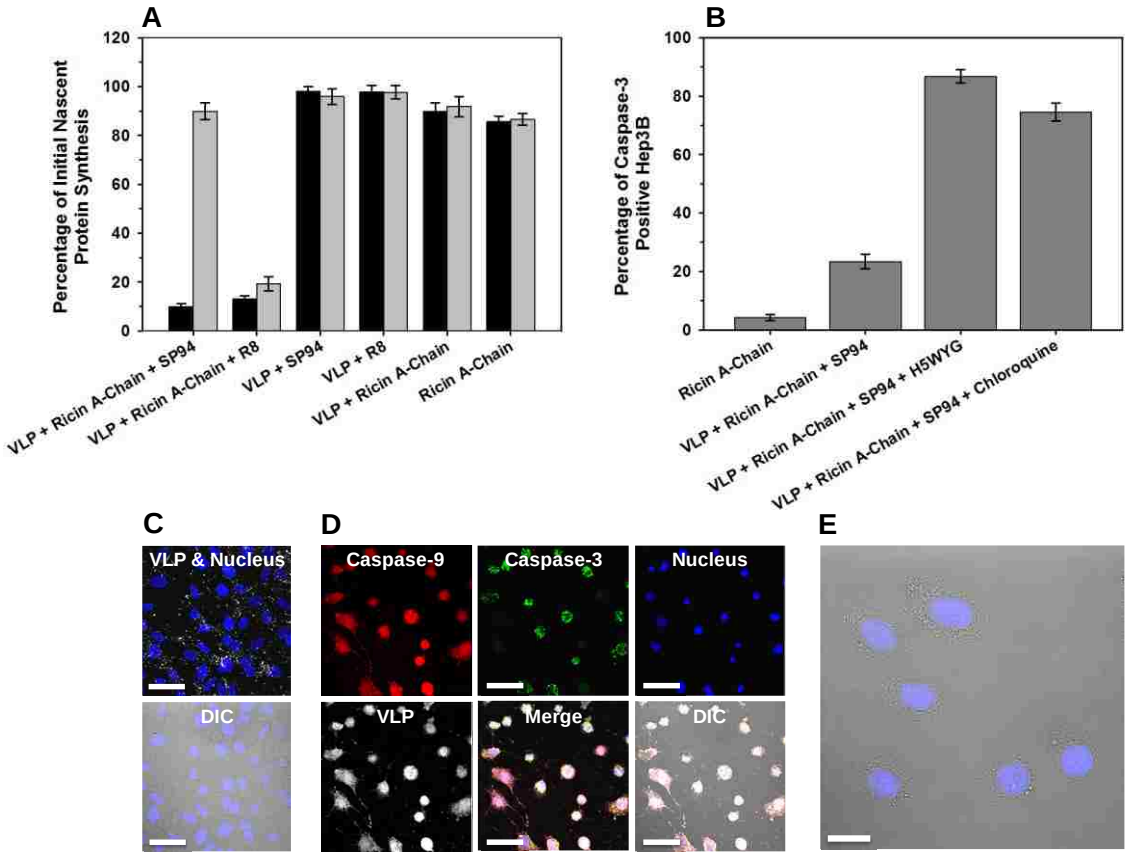

Figure S-6. MS2 VLPs, when modified with the SP94 targeting peptide, possess the specificity to deliver ricin A-chain to Hep3B without affecting the viability of hepatocytes. (A) The percentage of initial nascent protein synthesis that remains upon exposure of Hep3B (■) and hepatocytes (■) to ricin A-chain-loaded VLPs modified with either the SP94 peptide or the R8 peptide. SP94-modified VLPs, R8-modified VLPs, unmodified VLPs loaded with ricin A-chain, and ricin A-chain alone have no affect on protein biosynthesis in either Hep3B or hepatocytes. (B) The percentage of apoptotic Hep3B (i.e. cells that are positive for caspase-3 activation) increases dramatically when VLPs co-modified with the SP94 targeting peptide and the H5WYG fusogenic peptide are utilized to deliver ricin A-chain. Endosomal escape of ricin A-chain loaded VLPs is critical to promote apoptosis of Hep3B, as evidenced by the relative inability of SP94-targeted VLPs loaded with ricin A-chain to induce caspase-3 activation; the activity of these VLPs can, however, be recovered by inhibiting lysosomal acidification via exposure of Hep3B to chloroquine. (C) – (E) SP94-targeted, ricin A-chain-loaded VLPs, labeled with Alexa Fluor® 647 (white), are rapidly endocytosed by Hep3B (C) and induce selective apoptosis, as evidenced by caspase-3 and caspase-9 activation, within 72 hours (D). SP94-targeted VLPs that encapsidate ricin A-chain do not affect the viability of hepatocytes even after continual exposure for 7 days (E). Hep3B and hepatocyte nuclei are labeled with DAPI. All scale bars = 20 μm. All error bars represent 95% confidence intervals (1.96 σ) for n = 3.

CHAPTER 3

In-situ Grazing Incidence Small Angle X-ray Scattering of 2D Virus-Like Particle Lattice Formation via a Convective Assembly Process

The use of viral particles (including icosahedral and filamentous bacterial phages, as well as plant viruses1) as building blocks or scaffolds in the synthesis of nanoscale materials presents several distinct advantages over the use of 'artificial' nanoparticles, including perfect monodispersity, convenience of synthesis from laboratory culture, and, most importantly, the range of strategies available to selectively modify the viral structure with organic or inorganic substances, including the encapsidation of nanoparticles[2] or other foreign materials within the internal volume of the particle and the conjugation of functional peptides (either through chemical reaction or genetic engineering) to selectively bind or nucleate the growth of inorganic materials at the surface of the viral capsid[1, 3, 4]. By combining these particle modification approaches with 'bottom-up' self-assembly, viral particles could, in principle, be used as scaffolds, templates, or 'nanocontainers' to organize virtually any type of functional inorganic material into larger hierarchical structures relevant to energy transduction, sensing, information storage, logic devices, etc.[1-4] Synthesis of these assemblies will require a continuous coating method applicable to large-scale solid substrates; although 3D crystallization[5], liquid crystal organization[6-8], and interfacial assembly[9-11] of viral particles has been investigated as means of viral lattice formation, *convective assembly*[12-17] (CA) has emerged as a promising tool for the rapid, generalized deposition of colloidal assemblies directly onto a solid surface. In CA (Figure 1), a film is deposited from a microliter-sized

droplet of a colloidal suspension trapped between a fixed substrate and a plate moving at constant velocity v across the substrate at a fixed angle θ (typically < 30° with respect to one another). Although originally developed for spherical colloids, CA has since been applied to ordered arrays of tobacco mosaic virus (TMV), a rod-like plant virus with diameter of ca. 18 nm and length of approximately 300 nm[17]; here, we extend this method to viral particles with icosohedral symmetry, specifically virus-like particles (VLPs, capsids assembled from viral coat protein without the presence of genetic material) derived from the bacteriophages MS2 and Qβ (Figure 2), and examine the mechanism of lattice formation during CA using *in-situ* grazing-incidence small-angle x-ray scattering (GISAXS) performed at a synchrotron source. Icosohedral viruses and VLPs present a number of advantages as nanoscale building blocks arrays over TMV or other filamentous phages, including almost spherical symmetry and near perfect monodispersity enabling the assembly of highly ordered crystalline lattices[9-11], ability to produce VLPs from plasmids in *E. coli* in large quantities[18], and availability of improved genetic screens and selections[19] relative to those available for rod-like viruses that could eventually allow the identification of mutants with altered interaction potentials or the ability to direct specific growth of inorganic materials. Furthermore, GISAXS enables

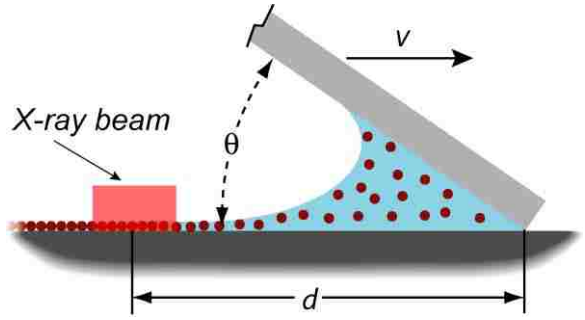

Figure 1. Schematic of the convective assembly process used in GISAXS studies of VLP self-assembly. A plate at angle θ is moved across a substrate at velocity v, trailing a meniscus from which a particle film is deposited. The self-assembly process is observed at a fixed position on the substrate

the *in-situ* characterization of nanostructure during dynamic assembly processes in real-time under an ambient environments[20-22], unlike electron microscopy (a technique generally limited to *ex-situ* studies[20, 23-25]) or optical methods. In GISAXS, an x-ray beam is incident upon a sample at an angle greater than the critical angle of the film but less than that of the substrate, thus maximizing the scattering volume inside the film and, coupled with the high photon flux obtained at a synchrotron source, enabling the investigation of fast (on the time scale of seconds) self-assembly phenomena of films as thin as one monolayer [20]. For the study of CA, the x-ray beam is placed at a fixed position upon the solid substrate (Figure 1); the film assembly process is monitored as the plate of the convective coater passes through this spot.

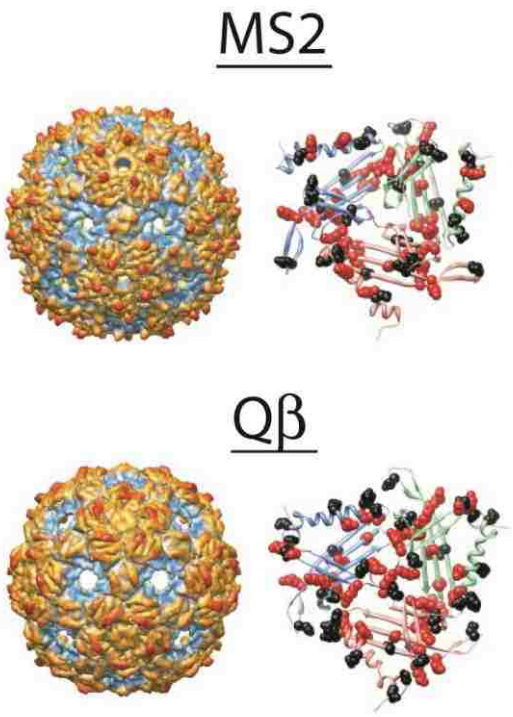

Figure 2. Structures of Qβ (a) and MS2 (b) bacteriophages, and close-ups of phage subunit structure for Qβ (c) and MS2 (d). Acidic and basic amino acid residues are highlighted in red and blue, respectively, with hydrophobic loops in black.

Our initial studies compared the CA of VLPs derived from MS2 and Qβ (Figure 2). MS2 and Qβ are nearly identical in size (27. 5 nm and 28.5 nm, respectively), but differ in overall surface charge charge (3.9 vs. 5.3 for MS2 and Qβ at a pH of 7.2), charge distribution (both across the surface and radially from the center of the particle), and acidity (with isoelectric points of 3.9 and 5.3 for MS2 and Qβ). As seen in the time sequence *in-situ* GISAXS data in Figure 3, these differences result in

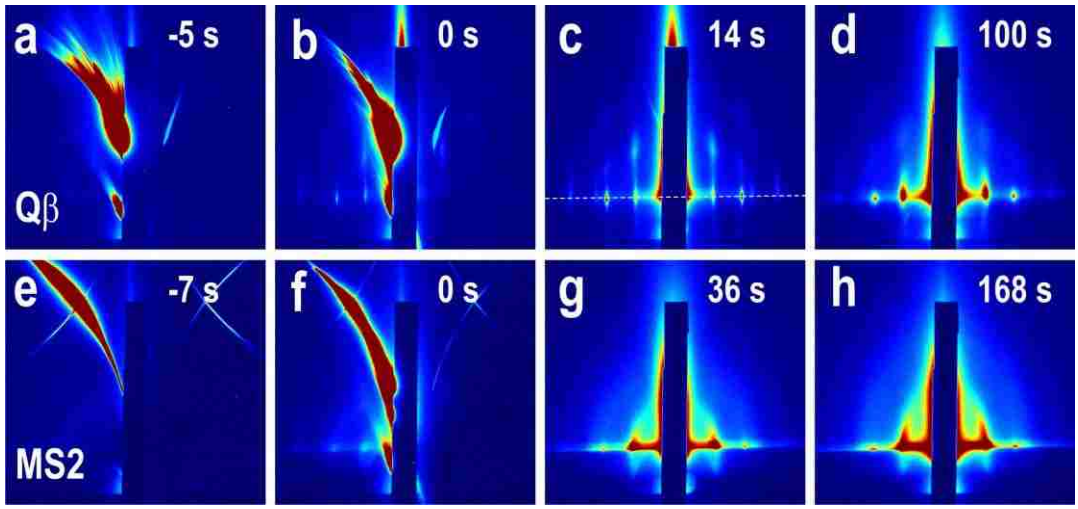

Figure 3. Time sequence of GISAXS data, referenced to the first emergence of the x-ray beam from behind the plate of the convective coater (panels a and e), comparing the self-assembly of Qβ (a-d) and MS2 (e-h) from 100mM NaCl under identical coating conditions. For Qβ, assembly of 2D arrays occurs without intermediate aggregation or structure (b-c); disappearance of (20) and (21) reflections indicates loss of long-range order during film drying (d). MS2 assembly is characterized by formation of multilayer aggregates (g) which are deposited as a glassy film with poor translational order(h). Plate movement is from left to right in both series of images.

dissimilar self-assembly behavior. In this data, time referenced to the first appearance of a particle array (panels b and f), initial scattering for both particle types is dominated by a low-angle reflection from the curved liquid meniscus and glass slide of the convective coater (panels a and b); a set of cross-hatched scattering features also appears (most notably in the data set for MS2), a feature that we do not attribute to any self-assembly process given the symmetry of these features with the background reflection. For Qβ, the self-assembly process can be divided into two stages; direct appearance (panel b) and evolution (panel c), notably without any intermediate structure, followed by a reduction in film ordering from water evaporation (panel d). However, MS2 assembly is characterized by the formation of multilayer aggregates (panels f and g), as evidenced by the inward curvature of the scattering features along the substrate axis; this aggregation is

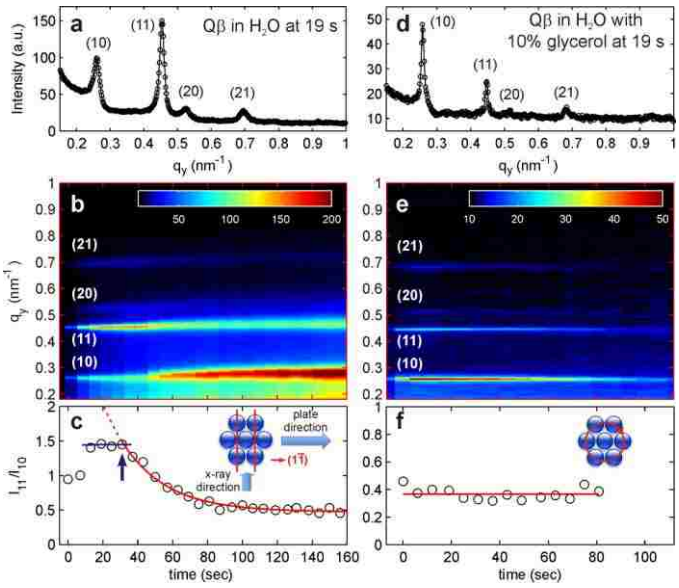

Figure 4. a) A horizontal linecut at q_z= 0.24 ± 0.02 nm^{-1} taken from the GISAXS data for Qb self-assembled in water at t=19 (the dashed line marked in Figure 3c). The first four Bragg diffractions are indexed to 2D hexagonal packing. b) The time evolution of this horizontal linecut. c) The ratio of the integrated intensities underneath the (11) and (10) reflections, after background subtraction. The red line is a fit to an exponential decay function as described in the text, and the inset represents the dominant 2D domain orientation induced by convective transport. (d)-(f) are corresponding panels from GISAXS for Qb in water with 10% glycerol.

intensified after complete film drying (panel h), resulting in a glassy film without long-range order. This propensity toward aggregation for MS2 is a result of the ionic properties of this particle, a conclusion supported by assembly as a function of ionic strength (*vide infra*).Data for Qβ assembly was analyzed in further detail as presented in Figure 4a-c. Line cuts plotted as a function of time (panel b) show a broadening of the (10) diffraction peak as well as a shift to higher *q* during film drying.. The (10) peak shape analysis in the beginning at t=19 sec shows a lattice constant of 24.2 nm (giving an interparticle spacing of 24.2*(2/sqrt(3)) = 28.0 nm, consistent with the size of Qβ) with a domain size of ~280 nm. Similar analysis near the end at t=162 sec shows a contracted packing of lattice constant of 22.3 nm (an interparticle distance of 25.7 nm) and an

average domain size of ~158 nm. We attribute this shrinkage in interparticle spacing during film drying to collapse of the (empty) VLP capsid. The average number of particles per domain also decreases by 60% during film drying, from ca. 130 at t = 19 sec to ca. 50 at t = 162 sec).

Figure 4c plots the intensity ratio of (11) and (10) reflections from the data in panel b. From this data, it is apparent that convective transport favors an orientation of the self-assembled domains with (11) direction parallel to the direction of the plate motion. This initial lattice orientation is consistent with an assembly mechanism whereby convective transport of particles toward a drying front, induced by water evaporation, is combined with immersion capillary forces to guide the packing of colloidal particles into a 2D lattice[26]. The observed reorientation of lattice domains after assembly demonstrates that the film maintains fluidity over a time scale sufficient for structural rearrangement in the film, either by rotation of entire lattice domains or diffusion of individual particles; the presence of either process suggests incomplete surface coverage of the 2D viral array. This thermal diffusion can be fit to an exponential decay of the form of $I_{11}/I_{10} = C_1 + C_2 e^{-t/\tau}$, giving a characteristic time scale τ of 26±3 sec, consistent with the onset time of 31 sec (labeled as blue arrow c) for this diffusion mechanism to dominate the average orientation of the VPL domains. The peak intensity ratio saturates at a value of $C_1 = 0.47$, slightly smaller than 0.58 estimated from the simulations for randomly orientated 2D domains modeled using paracrystal theory,[27] an effect we attribute to the form factor of the VLP particles.

In contrast to Qβ assembly from H_2O, Qβ self-assembled in 10% glycerol has a nearly constant lattice parameter of 24.4 nm (inter-particle distance is 28.2 nm), and

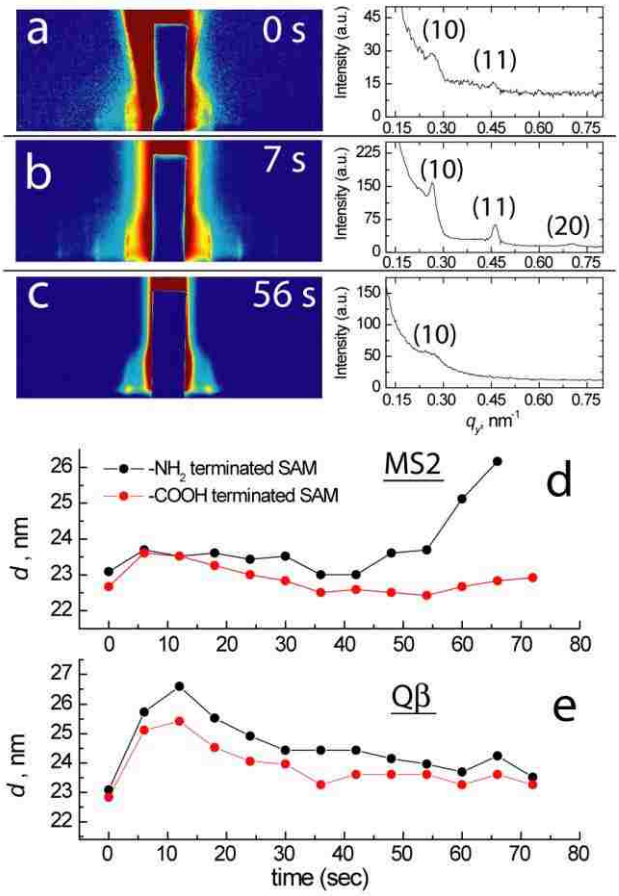

Figure 5. a-c) Time sequence in-situ GISAXS data for the convective assembly of MS2 onto an amine-modified surface, with initial appearance of the MS2 lattice (a) followed by development of lattice order (b) and ultimate collapse after film drying (c). d) Lattice spacing for the (10) reflection as a function of time for MS2 assembled at an amine or carboxylate-terminated SAM, e) as d, but for Qβ.

much better degree of ordering, seen as much sharper diffractions in (d) and (e). However, the observed FWHM of the diffraction are limited by our instrument resolutions of ~0.01 nm^{-1}, which indicates an averaged domain size beyond ~600 nm. Furthermore, the ratio of (10) to (11) intensity is constant over time (Figures 4e and f), with a value that suggests formation of random domain orientation within the film. We posit that lack of favored domain orientation, along with the increased long-range order

relative to films deposited from 100 mM NaCl, is a result of a fundamentally different mechanism for lattice assembly; specifically, we hypothesize a self-assembly mechanism where convective flow at the drying line is negligible due to an increase in viscosity in the coating solution after preferential evaporation of water as well as the inherent low volatility of glycerol. Instead, transport of particles to the growing lattice is controlled by 2D diffusion, with the implication that diffusion-controlled transport results in greater long-range order of the 2D crystal. We note that mobility at the substrate surface due to the presence of a non-volatile medium cannot account for the increased order alone, as the rearrangement of lattice orientation seen in films deposited from 100 mM NaCl indicate significant surface mobility of particles without glycerol over the time frame of film formation. Another factor that may influence the degree of long-range order in assemblies of viral particles between glycerol and aqueous solutions is the Debye length of the virus. However, variation of the Debye length for Qβ during self-assembly by variation of the NaCl concentration (from 0.1 to 1.0 M) did not show any increase in the degree of long-range ordering, suggesting that for Qβ electrostatic screening is not a significant factor in lattice formation, again consistent with convective transport dominating the self-assembly process from aqueous solutions[26]. Reduction in immersion capillary forces during the 2D crystallization process between particles in water versus particles in glycerol may play a role in increased lattice ordering, although the reduction in interparticle force in the latter case is expected to be only ca. 13%[26].

Finally, we utilized our in-situ GISAXS studies of VLP assembly to identify experimental conditions under which the aggregation of MS2 is reduced during the self-

assembly process, enabling the assembly of ordered 2D lattices using convective assembly. According to DLVO (Derjaguin-Landau-Verwey-Overbeek) theory[28-30], aggregation driven by van der Waals forces can be lessened by increasing the electrostatic repulsion between particles through reduction of the ionic strength of the supporting medium, or by increasing the surface potential of the particles[31]. Consistent with these predictions, a study of assembly from NaCl solutions with ionic strengths between 0.10 to 1.0 M found that aggregation of MS2 was eliminated for NaCl concentrations below 100 mM, forming ordered 2D lattices. Assuming a 10-fold concentration of electrolyte at the point of MS2 aggregation, this corresponds to a Debye length of ca. 1 nm, on the same length scale as the peptide loops extending from the surface of MS2. Similarly, increasing the surface potential of MS2 by addition of surface charge through chemical conjugation with decamers of the cationic peptides poly-L-lysine or poly-L-arginine inhibited aggregation of MS2, permitting the assembly of 2D close-packed lattices from 100 mM NaCl onto oxidized silicon.

Assembly onto amine- or carboxylate- modified surfaces was also found to reduce aggregation of MS2 while altering the self-assembly pathway for both MS2 and Qβ VLPs relative to that seen for lattice formation at oxidized silicon. Example *in-situ* data for MS2 assembly at an amine-modified self-assembled monolayer (SAM) is shown in Fig.5 panels a-c; data for assembly at a carboxylic-acid terminated interface as well as for Qβ at either surface is qualitatively similar. We find that lattice development at a modified substrate differs in several important respects over that seen at an unmodified (silica) surface. First, ordering in MS2 arrays is increased relative to that seen at unmodified surfaces under identical solution conditions as evidenced by the appearance of a (20)

reflection (Fig. 5b). Unlike assembly of Qβ at unmodified surfaces, the I_{11}/I_{10} ratio for both MS2 and Qβ is constant throughout the entire film formation process (equal to ca. 0.4, consistent with isotropic ordering of lattice domains in the plane of the substrate) until complete film drying induces collapse of the VLP lattice (Fig. 5c). However, there are significant changes in lattice spacing over time; as seen in Figs. 5d and e for MS2 and Qβ, respectively, the (10) interplanar spacing undergoes expansion from an initial compacted state (with this effect much more pronounced for Qβ than MS2) followed by shrinkage of the lattice during film drying (as was seen for Qβ assembly at silicon) and, in the case of MS2, complete collapse of the film into a glassy state (Fig. 5c). Furthermore, (10) spacing indicates that the initial VLP lattice is compressed by ca. 20% in the plane of the substrate; while the Qβ interparticle distance recovers to

Based upon this data, we posit a mechanism for VLP assembly at an amine- or carboxylate-modified surface whereby the initial VLP lattice is not formed by convective transport (as evidenced by the isotropic lattice orientation), but rather by adsorption of VLP to the SAM surface at a point prior to the emergence of the x-ray beam from behind the coater meniscus, with the formation of an ordered MS2 lattice suggesting that this adsorption occurs before solvent evaporation increases the VLP concentration to a point where MS2 aggregation is induced. During the adsorption step, the VLP capsid is compressed; expansion of the interparticle distance during film drying demonstrates fluidity in the adsorbed VLP monolayer. For MS2, the presence of an ordered is temporary, with complete film drying prompting lattice collapse via aggregation.

In conclusion, we have demonstrated the formation of well-ordered 2D crystals of empty viral capsids though a convective coating technique, following the self-assembly

process in real time using grazing-incidence small-angle x-ray scattering at a synchrotron source. The assembly mechanism is consistent with convective transport of particles to the drying front of the evaporating film; scrambling of lattice orientation after the initial assembly stage shows the presence of fluidity in the VLP monolayer. Addition of non-volatile solvent to the VLP solution increases domain size, with an invariant average lattice orientation suggesting that assembly does not occur through convective transport, but possibly by particle diffusion within the deposited film. Although 2D lattice formation of MS2 was suppressed by solution aggregation under conditions that otherwise led to well-defined crystallization of Qβ, using DLVO theory we identified experimental parameters that can be modified to inhibit VLP aggregation (ionic strength of the solution, MS2 surface potential), and confirmed the formation of ordered MS2 lattices under these conditions.

Methods MS2 and Qβ bacteriophages were produced by infection of *Escherichia coli* A/λ using standard methods[32] and purified by sedimentation to equilibrium in CsCl gradients. Virus-like particles were produced from the parental bacteriophage via incubation in pH 11.8 buffer for 4 hours, which hydrolyzes the RNA genome and results in empty capsids. VLPs were stored in TNME buffer (10 mMTris-HCl, 100 mM NaCl, 0.1 mM $MgSO_4$, and 0.01 mM EDTA at pH 7.4) at 4°C. The following conditions were employed in all GISAXS measurements: particle volume fraction (φ) = 0.02, deposition velocity (v) = 12 μm/s, relative humidity during the coating process = 15%. C-terminal cysteine residues of -L-lysine or poly-L-arginine were chemically conjugated to surface

lysine residues present in the MS2 capsid using a heterobifunctional crosslinker; each MS2 particle was estimated to bear 120 copies of poly(Lys) or poly(Arg).

GISAXS measurements were performed on beam line 8-ID at the Advanced Photon Source at Argonne National Labs using a wavelength of 1.6868 Å, a sample-to-detector distance of either 1580 or 1254 mm, an analysis angle of 0.20°, and a 2048 x 2048 Marr CCD detector. The 100 μm x 50 μm beam was fixed relative to the substrate (Figure 1), with the beam direction perpendicular to the movement of the coater plate. Detector images were obtained with a period of 6 seconds, using an integration time of 1 second.

References:

1. Young, M.; Willits, D.; Uchida, M.; Douglas, T. *Annual Review Of Phytopathology* **2008,** 46, 361-384.
2. Aniagyei, S. E.; DuFort, C.; Kao, C. C.; Dragnea, B. *Journal Of Materials Chemistry* **2008,** 18, (32), 3763-3774.
3. Fischlechner, M.; Donath, E. *Angewandte Chemie-International Edition* **2007,** 46, (18), 3184-3193.
4. Merzlyak, A.; Lee, S. W. *Current Opinion In Chemical Biology* **2006,** 10, (3), 246-252.
5. Kuznetsov, Y. G.; Malkin, A. J.; Lucas, R. W.; Plomp, M.; McPherson, A. *Journal Of General Virology* **2001,** 82, 2025-2034.
6. Lee, S. W.; Lee, S. K.; Belcher, A. M. *Advanced Materials* **2003,** 15, (9), 689-692.
7. Lee, S. W.; Mao, C. B.; Flynn, C. E.; Belcher, A. M. *Science* **2002,** 296, (5569), 892-895.
8. Lee, S. W.; Wood, B. M.; Belcher, A. M. *Langmuir* **2003,** 19, (5), 1592-1598.
9. He, J. B.; Niu, Z. W.; Tangirala, R.; Wan, J. Y.; Wei, X. Y.; Kaur, G.; Wang, Q.; Jutz, G.; Boker, A.; Lee, B.; Pingali, S. V.; Thiyagarajan, P.; Emrick, T.; Russell, T. P. *Langmuir* **2009,** 25, (9), 4979-4987.
10. Kaur, G.; He, J. B.; Xu, J.; Pingali, S. V.; Jutz, G.; Boker, A.; Niu, Z. W.; Li, T.; Rawlinson, D.; Emrick, T.; Lee, B.; Thiyagarajan, P.; Russell, T. P.; Wang, Q. *Langmuir* **2009,** 25, (9), 5168-5176.
11. Russell, J. T.; Lin, Y.; Boker, A.; Su, L.; Carl, P.; Zettl, H.; He, J. B.; Sill, K.; Tangirala, R.; Emrick, T.; Littrell, K.; Thiyagarajan, P.; Cookson, D.; Fery, A.; Wang, Q.; Russell, T. P. *Angewandte Chemie-International Edition* **2005,** 44, (16), 2420-2426.
12. Yuan, Z.; Petsev, D. N.; Prevo, B. G.; Velev, O. D.; Atanassov, P. *Langmuir* **2007,** 23, (10), 5498-5504.
13. Prevo, B. G.; Hwang, Y.; Velev, O. D. *Chemistry Of Materials* **2005,** 17, (14), 3642-3651.
14. Prevo, B. G.; Fuller, J. C.; Velev, O. D. *Chemistry Of Materials* **2005,** 17, (1), 28-35.
15. Prevo, B. G.; Velev, O. D. *Langmuir* **2004,** 20, (6), 2099-2107.
16. Kuncicky, D. M.; Naik, R. R.; Velev, O. D. *Small* **2006,** 2, (12), 1462-1466.
17. Wargacki, S. P.; Pate, B.; Vaia, R. A. *Langmuir* **2008,** 24, (10), 5439-5444.
18. Peabody, D. S. *J. Biol. Chem.* **1990,** 265, 5684-5689.
19. Peabody, D. S.; Manifold-Wheeler, B.; Medford, A.; Jordan, S. K.; do Carmo Calderia, J.; Chackerian, B. *J. Mol. Biol.* **2008,** 380, 252-263.
20. Narayanan, S.; Wang, J.; Lin, X.-M. *Phys. Rev. Lett.* **2004,** 93, (13).
21. Roth, S. V.; Autenrieth, T.; Gruebel, G.; Riekel, C.; Burghammer, M.; Hengstler, R.; Schulz, L.; Mueller-Buschbaum, P. *Appl. Phys. Lett.* **2007,** 91, 091915.
22. Dunphy, D.; Fan, H. Y.; Li, X. F.; Wang, J.; Brinker, C. J. *Langmuir* **2008,** 24, (19), 10575-10578.
23. Bigoni, T. P.; Lin, X.-M.; Nguyen, T. T.; Corwin, E. I.; Witten, T. A.; Jaeger, H. M. *Nature Mater.* **2006,** 5, 265-270.

24. Lin, X.-M.; Jaeger, H. M.; Sorensen, C. M.; Klabunde, K. J. *J. Phys. Chem. B* **2001,** 105, 3353-3357.
25. Schulz, D. G.; Lin, X.-M.; Li, D.; Gebhardt, J.; Meron, M.; Viccaro, P. J.; Lin, B. *J. Phys. Chem. B* **2006,** 110, 24522-24529.
26. Denkov, N. D.; Velev, O. D.; Kralchevsky, P. A.; Ivanov, I. B.; Yoshimura, H.; Nagayama, K. *Langmuir* **1992,** 8, 3183-3190.
27. Hosemann, R.; Bagchi, S. N., *Direct Analysis of Diffraction by Matter*. North-Holland Publishing: Amsterdam, 1962.
28. Derjaguin, B. V., *Theory of Stability of Colloids and Thin Films*. Plenum: New York, 1989.
29. Derjaguin, B. V.; Churaev, N. V.; Muller, V. M., *Surface Forces*. Plenum: New York, 1987.
30. Verwey, E. J. W.; Overbeek, J. T. G., *Theory and Stabilty of Lyophobic Colloids*. Elsevier: Amsterdam, 1948.
31. Israelachvili, J. N., *Intermolecular and Surface Forces*. 2nd ed.; Academic Press: New York, 1991.
32. Hooker, J. M.; Kovacs, E. W.; Francis, M. B. *Journal of the American Chemical Society* **2004,** 126, (12), 3718.

SUMMARY OF CONTRIBUTIONS

I, Carlee Ashley, designed and performed all experiments described in this manuscript but wish to acknowledge contributions made by the following individuals. The original protocell construct was conceived of by Jeffrey Brinker and engineered for use in non-specific transfection applications by Juewen Liu. Bimodal silica particles were developed and synthesized by Nichlaus Carroll, under the direction of Dimiter Petsev, while monomodal silica particles were synthesized by Xingmao Jiang. Genevieve Phillips performed all hyperspectral confocal fluorescence microscopy imaging, while Brandy Comyford collected most flow cytometry data. David Padilla, Page Brown, and Tracey Hanna assisted with FRAP studies, as well as experiments involving delivery of doxorubicin to hepatocellular carcinoma via targeted protocells. Eric Carnes assisted with data analysis and figure preparation, while David Peabody and Walker Wharton provided overall guidance and advice.

Experiments involving the use of targeted VLPs for delivery of siRNA cocktails to hepatocellular carcinoma were directed by Walker Wharton. Bryce Chackerian suggested several schemes for conjugating peptides and other ligands to the surfaces of VLPs. Constantine Khripin and Matthew Rush performed all AFM experiments, while Tamara Howard imaged re-assembled VLPs via TEM. Genevieve Phillips collected hyperspectral and 3D confocal fluorescence images. David Peabody provided critical advice that enabled the development of VLPs for targeted delivery applications.

Orlin Velev, Dimiter Petsev, and Plamen Atanassov designed the meniscus coater that was employed in all convective assembly studies. Zhen (Cherry) Yuan built the

meniscus coater and helped determine the coating conditions that favored formation of *hcp* monolayers. GISAXS data was analyzed by Michael Sprung, Zhang Jiang, and Darren Dunphy, under the direction of Jin Wang. Darren Dunphy, additionally, assisted with all *in situ* GISAXS experiments and provided valuable interpretation of GISAXS data.